CENTER FOR RESEARCH AND ADVANCED STUDIES OF THE
NATIONAL POLYTECHNIC INSTITUTE

PHYSICS DEPARTMENT

"Measurement of the B_S^0 lifetime using the semileptonic decay channel $B_S^0 \to D_S^- \mu^+ \nu X$"

Thesis submitted by

Marco Antonio Carrasco Lizárraga

In order to obtain the

Doctor of Science

degree, speciality in

Physics

Supervisors: Alberto Sánchez Hernández, Ph. D.

Mexico City November, 2009,

Abstract

We report a measurement of the B_s^0 lifetime in the semileptonic decay channel $B_s^0 \to D_s^- \mu^+ \nu X$ (and its charge conjugate), using approximately 0.4 fb^{-1} of data collected with the DØ detector during 2002–2004. Using 5176 reconstructed $D_s^- \mu^+$ signal events, we have measured the B_s^0 lifetime to be $\tau(B_s^0) = 1.398 \pm 0.044$ (stat)$^{+0.028}_{-0.025}$ (syst) ps. This is the most precise measurement of the B_s^0 lifetime to date.

to Ari,
my mom and dad,
and my bro and sis.

Acknowledgements

First and foremost the work presented herein could not have been possible without the guidance and unconditional support from my thesis advisor Alberto Sánchez Henández, I sincerely thank you for your patience, friendship, and for keeping your faith in me all these years. Second, I could not have gotten this far without financial and institutional support, and for that I am very thankful to both the Department of Physics at CINVESTAV, and Mexico's own Consejo Nacional de Ciencia y Tecnología (CONACYT), whose grant permited me to be a full-time student and concentrate on my PhD work.

From the Department of Physics at CINVESTAV, special mention goes to professor Heriberto Castilla and secretary Patricia Villar. I thank you Heriberto for introducing me to experimental high energy physics and for all the help I got from you time and time again. Paty, I know it was no small feat getting me through my degree for all these years, its no overstatement when I say this accomplishment could not have been made without your help, so I bow down to you.

The D0 collaboration also deserves all my gratitude. It was the SMT group who welcomed me and I thank my mentor Mike Kirby in particular, I could not have asked for a better group leader and role model while I stayed at Fermilab. Other D0 role models, very dedicated and hard working people who I also look up to and want to thank are both Bill Lee and George Ginther. Both of you are examples of what I should aim to be.

Invaluable during my years of study was the moral support from my parents Marco and Irma, my brother Mario and sister Miusseth, as well as my newfound family at Cuernavaca. But nobody deserves my gratitude more than Ariadna Patjane, without you by my side for all those years none of this would have made any sense, or getting here even mattered. Carlos Stutz,

I thank you for your help and wisdom, but most of all, for you friendship. Hermelinda Brito, I thank you from the bottom of my heart, this accomplishment also goes to you who kept believing in me even during the most difficult of times. Ariana Ponciano, I won't forget you were there to give me a push forward at the start of my graduate studies, thanks.

I would also like to thank my CINVESTAV colleagues and friends Juan Barranco, Argelia Bernal, Abel Flores, Alain Flores, Lao-Tse López and Aldo Martínez. As well as the ones I left behind at Fermilab: Jesús Hernández, Suharyo Sumowidagdo and Daniel McCarron. You were always there for me when I needed you guys. And so were my online friends who kept me sane on those cold and lonely months away from home, I thank Rey, Karen, Jocelyn, Cindy, ByeShin and Lynn, I consider your friendships as some of the most genuine I've made in my life. Particularly I would like to express my gratitude to Lynn, the end was proving difficult but you pulled me through and out of the darkness and became my pillar and motivation, this degree is for you as well.

Last but not least, I thank the friends who took care of me unconditionally during the last year of my studies, when financial resources were scarce and all of you contributed to my survival and well being. I thank Eduardo, Bernardo, Alfonso and Ivan, my drinking buddies will surely be missed. Hecly and Ruben, you took care of me far more than anyone else during this period, I will never forget that and promise to make it up to you. Cesar, Arturo, Roxana, Erendi, Adriana and Angie, your help was essential in the final moments, but special mention goes to Roxana, you helped me more than I deserve, my gratitude and respect go out to you.

This thesis is the culmination of my PhD work, but it is a lot more than that, it probably represents the most important period in my life and I am thankful to each and everyone who has been a part of it, for better or for worse. Thanks everyone!

Contents

List of Figures

List of Tables

Chapter 1

Introduction

High Energy Physics, also referred to as Elementary Particle Physics, is that branch of Physics that researches elemental particles, their properties and the way they interact with each other. It does so by colliding material particles at very high speeds, so close to the speed of light that, if we remember Einstein's equations, a huge amount of energy is needed; henceforth the term High Energy Physics (HEP) has been adopted to describe this field of science. HEP's main goal is to study and understand what matter is made of, to its most fundamental level.

As in almost every other field of Science, research in HEP splits up in two main directions: theoretical and experimental work. Theory works on new or existing models that describe certain aspects of our universe, while experiments are designed to prove or disprove these models, sometimes even ending up with discoveries of whole new phenomena. In turn, both efforts go hand in hand and complement each other for an ultimate scientific understanding of the world around us and the laws that govern it, in any scale, from the subatomic to the cosmological and everything in between. As mentioned before, HEP deals with the subatomic scale, the elementary particles and fundamental blocks of matter, and the work presented in this thesis in particular, lives in the realm of experimentation of such scale.

The main idea of a HEP experiment, perhaps currently lacking better means, is to take an electrically charged subatomic particle, accelerate it to a speed as close to the speed of light as possible through the use of electromagnetic fields, and then put it on a head on crash course with either a fixed material target or an accelerated particle traveling in the opposite direction. The objective of this being that, if we want to know what that entity is made of or built with, we use this brute force method to break it into pieces. Sensitive and especialized detectors are placed at the collision point, and the data resulting from such events is recorded for experimental high energy physicists to analyze and try to reconstruct and understand.

In the remaining of this introductory chapter I'll summarize what these elementary building blocks have been found to be so far, and how they fit into a sort of subatomic periodic table called the standard model. That will be followed by a brief description of the spectator model and heavy quark expansion theories which led to the ideas that motivated the proposal of this thesis's research, finally ending the chapter with a basic description of what Fermilab is and the particular kind of work I performed while I stayed there as a PhD student. Chapter 2 will describe a few of the theoretical issues that serve as background for this work, while chapter 3 is used to describe the experimental setup in detail: the DØ detector itself. On Chapter 4 the data selection and event reconstruction methods are exposed, which will lead to the lifteime fit and final measurement presented in chapter 5. Consistency checks for the measurement will be described in chapter 6, as well as the calculations for the systematic uncertainties, finally recapping the ideas of this thesis in the conclusions and final thoughts found in chapter 7.

1.1 The Standard Model

The Standard Model of particle physics is a theory of three of the four known fundamental interactions and the elementary particles that take part in these

interactions. These particles make up all visible matter in the universe. Every high energy physics experiment carried out since the mid-20th century has eventually yielded findings consistent with the Standard Model [23]. Still, the Standard Model falls short of being a complete theory of fundamental interactions because it does not include gravitation, dark matter, or dark energy. It is not quite a complete description of leptons either, because it does not describe nonzero neutrino masses, although simple natural extensions do. The Standard Model groups two major extant theories, quantum electroweak and quantum chromodynamics, into an internally consistent theory describing the interactions between all experimentally observed particles. The Standard Model describes each type of particle in terms of a mathematical field, via quantum field theory.

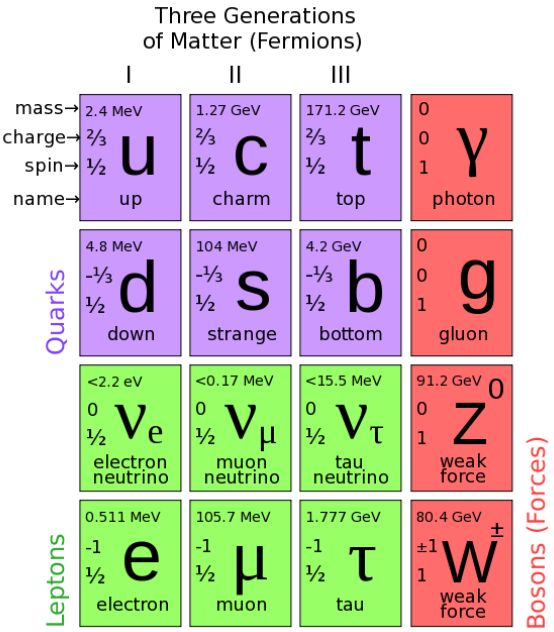

Figure 1.1: The Standard Model of elementary particles, with the gauge bosons in the rightmost column [23].

The Standard Model includes 12 elementary particles of spin $-1/2$ known as fermions. According to the spin-statistics theorem, fermions respect the Pauli Exclusion Principle. Each fermion has a corresponding antiparticle. The fermions of the Standard Model are classified according to how they interact (or equivalently, by what charges they carry). There are six quarks (up, down, charm, strange, top, bottom), and six leptons (electron, electron neutrino, muon, muon neutrino, tauon, tauon neutrino). Pairs from each classification are grouped together to form a generation, with corresponding particles exhibiting similar physical behavior.

The defining property of the quarks is that they carry color charge, and hence, interact via the strong interaction. The confining behavior of the strong force results in quarks being perpetually (or at least since very soon after the start of the big bang) bound to one another, forming color-neutral composite particles (hadrons) containing either a quark and an antiquark (mesons) or three quarks (baryons). The familiar proton and the neutron are the two baryons having the smallest mass. Quarks also carry electric charge and weak isospin. Hence they interact with other fermions both electromagnetically and via the weak nuclear interaction.

The remaining six fermions do not carry color charge and are called leptons. The three neutrinos do not carry electric charge either, so their motion is directly influenced only by the weak nuclear force, which makes them notoriously difficult to detect. However, by virtue of carrying an electric charge, the electron, muon, and tauon all interact electromagnetically.

Each member of a generation has greater mass than the corresponding particles of lower generations. The first generation charged particles do not decay; hence all ordinary (baryonic) matter is made of such particles. Specifically, all atoms consist of electrons orbiting atomic nuclei ultimately constituted of up and down quarks. Second and third generations charged particles, on the other hand, decay with very short half lives, and are observed only in very high-energy environments. Neutrinos of all generations also do not

decay and pervade the universe, but rarely interact with baryonic matter.

1.2 Heavy Hadron Lifetime Theory

Measurements of the lifetimes of different b hadrons (hadrons with a a bottom quark or antiquark) allow tests of the mechanism of heavy hadron decay. The spectator model predicts that all hadrons with the same heavy flavor content have identical lifetimes. However, observed charm and bottom hadron lifetimes suggest that non-spectator effects, such as interference between contributing amplitudes, are not negligible in heavy hadron decays. This implies that a mechanism beyond the simple spectator model is required. An effective theory called the Heavy Quark Expansion (HQE) [3] includes such effects and predicts lifetime differences among the different bottom hadrons. In particular, a difference of the order of 1% is predicted between B^0 and B_s^0 mesons. The measurement of the flavor-specific B_s^0 lifetime using semileptonic decays is also useful in determining the decay width difference between the light and heavy mass eigenstates of the B_s^0 meson, which is an equal mixture of CP eigenstates that correspond to mass eigenstates in the absence of CP violation in the B_s^0 system.

1.3 B_s^0 overview. Motivation for this thesis

A B_s^0 meson is composed of a s quark and a b antiquark, currently its measured mass is of 5366.3 ± 0.6 MeV [12]. The best lifetime measurements for this bottom-strange meson, published before this thesis, can be seen in figure 1.2. It is clear that statistical errors are at around 10% at best, which is due to the limited statistics accumulated by these experiments. Furthermore, B-factories like BaBar at SLAC in California and Belle at KEK in Japan, do not have enough energy to produce enough statistics for B_s^0 studies.

Henceforth, the main objective of the work presented in this thesis is to

B_s^0 MEAN LIFE

VALUE (10^{-12} s)	DOCUMENT ID		TECN	COMMENT
$1.42\ ^{+0.14}_{-0.13} \pm 0.03$	[6] ABREU	00Y	DLPH	$e^+e^- \to Z$
$1.53\ ^{+0.16}_{-0.15} \pm 0.07$	[7] ABREU,P	00G	DLPH	$e^+e^- \to Z$
$1.36 \pm 0.09\ ^{+0.06}_{-0.05}$	[8] ABE	99D	CDF	$p\overline{p}$ at 1.8 TeV
$1.72\ ^{+0.20}_{-0.19}\ ^{+0.18}_{-0.17}$	[9] ACKERSTAFF	98F	OPAL	$e^+e^- \to Z$
$1.50\ ^{+0.16}_{-0.15} \pm 0.04$	[8] ACKERSTAFF	98G	OPAL	$e^+e^- \to Z$
$1.47 \pm 0.14 \pm 0.08$	[7] BARATE	98C	ALEP	$e^+e^- \to Z$
$1.54\ ^{+0.14}_{-0.13} \pm 0.04$	[8] BUSKULIC	96M	ALEP	$e^+e^- \to Z$

Figure 1.2: Previous B_s^0 lifetime measurements [12].

make a very precise measurement of the lifetime of the B_s^0, that is, with the the smallest error ever recorded to make it the best of its kind. Also motivating this work and as hinted in section 1.2, HQE predictions can be tested measuring the lifetime of the bottom-strange meson B_s^0 and comparing it to that of B^0. A final motivating factor for this measurement will be explained with greater detail in section 1.3.2.

1.3.1 Why use $B_s^0 \to D_s^- \mu^+ \nu X$?

Having decided to measure B_s^0's lifetime, the next step is to choose a decay channel for it. The basic idea is that we have to take our detector in mind and know its strengths and weaknesses, in order to obtain higher statistics with a cleaner signal (the most significant over the noise). Figure 1.3 lists the decay channels with higher probabilities. From it, it is clear that with a 93% chance a B_s^0 will decay into some combination containing a charmed-strange meson D_s^- $(\bar{c}, s)$, plus something else.

Now, the particular channel with the highest probability is the semileptonic decay in which B_s^0 decays into a D_s^-, a lepton and its corresponding neutrino, plus something else. The probability is high compared to other

channels, but it has an important drawback: the neutrino. Our detector can't "see" neutrinos, so we will not be able to fully reconstruct the B_s^0 which we want to measure. But on the other hand, there is an extremely important postive factor about this decay: if the lepton is a muon, then we can make use of DØ̃'s muon detectors and single-muon trigger to greatly reduce the combinatorial background in our data selection and event reconstruction process. The single-muon trigger translates to a proper identification of a charged track as a muon, whereas tracks recorded at DØ̃'s central tracking system (section 3.4) will not be properly identified since that system lacks the ability to do so.

B_s^0 DECAY MODES

Mode	Fraction (Γ_i/Γ)
D_s^- anything	(93 $\pm$25) %
$D_s^- \ell^+ \nu_\ell$ anything	(7.9 $\pm$ 2.4) %
$D_{s1}(2536)^- \mu^+ \nu_\mu X \times$ B($D_{s1}^- \rightarrow D^{*-} K_S^0$)	(2.3 $\pm$ 0.7) $\times 10^{-3}$
$D_s^- \pi^+$	(3.3 $\pm$ 0.5) $\times 10^{-3}$
$D_s^- \pi^+ \pi^+ \pi^-$	(8.4 $\pm$ 3.3) $\times 10^{-3}$
$D_s^- K^+$	(2.4 $^{+\ 1.3}_{-\ 1.1}$) $\times 10^{-4}$
$D_s^+ D_s^-$	(1.1 $\pm$ 0.4) %
$D_s^{*+} D_s^-$	$<$ 12.1 %
$D_s^{*+} D_s^{*-}$	$<$ 25.7 %
$D_s^{(*)+} D_s^{(*)-}$	(3.9 $\pm$ 1.5) %
$J/\psi(1S)\phi$	(1.3 $\pm$ 0.4) $\times 10^{-3}$
$J/\psi(1S)\pi^0$	$<$ 1.2 $\times 10^{-3}$
$J/\psi(1S)\eta$	$<$ 3.8 $\times 10^{-3}$

Figure 1.3: Selected B_s^0 decay modes. Highest (Γ_i/Γ) fraction modes are shown [12].

Looking at the rest of decay channels on figure 1.3, and taking into account that the more charged tracks we introduce (like pions), the more our combinatorial background will increase, we choose the decay channel $B_s^0 \to D_s^- \mu^+ \nu X$ as our best option, not a fully reconstructable channel, but one with cleaner signals due to the detector's abilities to properly identify muons. Next, we are faced with another decay channel decision, the D_s^-.

D_s^+ DECAY MODES

Hadronic modes with a $K\overline{K}$ pair

$K^+ K_S^0$	(1.49 ± 0.09) %
$K^+ K^- \pi^+$	(5.50 ± 0.28) %
$\phi\pi^+$	(4.38 ± 0.35) %
$\phi\pi^+$, $\phi \to K^+K^-$	(2.18 ± 0.33) %
$K^+ \overline{K}^*(892)^0$	
$K^+ \overline{K}^*(892)^0$, $\overline{K}^{*0} \to K^-\pi^+$	(2.6 ± 0.4) %
$f_0(980)\pi^+$, $f_0 \to K^+K^-$	(6.0 ± 2.4) × 10^{-3}
$K^+ \overline{K}_0^*(1430)^0$, $\overline{K}_0^* \to K^-\pi^+$	(5.1 ± 2.5) × 10^{-3}
$f_0(1710)\pi^+$, $f_0 \to K^+K^-$	
$K^+K^-\pi^+$ nonresonant	
$K^0 \overline{K}^0 \pi^+$	—
$K^*(892)^+ \overline{K}^0$	(5.3 ± 1.2) %
$K^+K^-\pi^+\pi^0$	(5.6 ± 0.5) %
$\phi\pi^+\pi^0$, $\phi \to K^+K^-$	
$\phi\rho^+$, $\phi \to K^+K^-$	(4.0 $^{+\ 1.1}_{-\ 1.2}$) %

Figure 1.4: D_s^+ hadronic decay modes (with a $K\bar{K}$ pair). Highest (Γ_i/Γ) fraction modes are shown [12].

The D_s^- originating from a B_s^0 decay will, in turn, also decay and there are many ways it could do it, the most probable of which are shown in figure 1.4. These modes all end up with a $K\bar{K}$ pair, two charged tracks we can look for using the central tracking system. Looking at the modes with higher probabilities, we discard those with neutral particles which will decay in photons like the π^0 or the $\bar{K^0}$. We are left with two channels of interest:

$D_s^- \to K^-K^+\pi^-$ and $D_s^- \to \phi\pi^-$. In the first case we have 3 charged tracks (K^-, K^+, π^-), in the latter the ϕ will decay through $\phi \to K^-K^+$, so in the end it will also have the same 3 tracks. The big difference though, is that through the ϕ decay, we can restrict a couple of the kaons to be consistent with the ϕ's mass, while in the first case, were we directly have the $D_s^- \to K^-K^+\pi^-$ decay, we dont have this condition to clean our signal, so we will end up with a lot more statistics, but most of which will be unwanted combinatorial background noise.

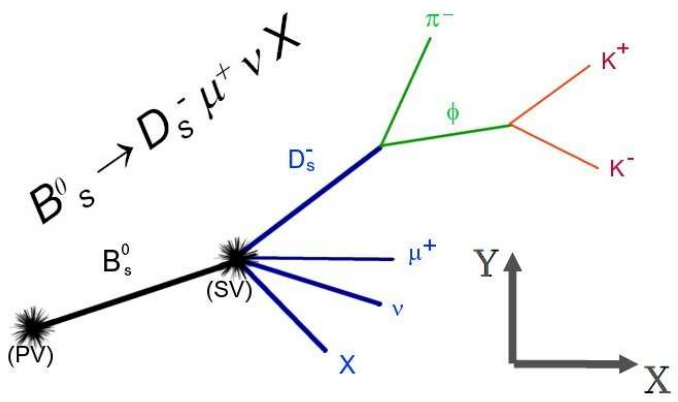

Figure 1.5: Graphic representation of the semileptonic decay channel $B_s^0 \to D_s^-\mu^+\nu X$.

Having chosen our decay channels one after another in order to get the highest probability modes while thinking ahead and keeping in mind our detector's capabilities to properly identify particles and our abilities to filter our data for cleaner signals, we are left with the best choice of decay mode to make the lifetime measurement we are after. This decay mode can be summarized through figure 1.5. The primary vertex (PV) is located at the $p\bar{p}$ collision point spotted on the beampipe, B_s^0 is thought to originate here and travel until it decays at what its called the secondary vertex (SV). The distance it travels from PV to SV is called the Decay Length and it will be

discussed further on section 4.4, since measuring it is critical in reaching our goal.

1.3.2 Determining $\Delta\Gamma_s$ from $B_s \to D_s^- \mu^+ X$

Using the flavor specific decay $B_s \to D_s^- \mu^+ X$ we could test the sensitivity on the determination of lifetime differences between the CP even and CP odd eigenstates of the B_s^0 meson. For this thesis, we will perform the lifetime measurement of the B_s^0 meson using the assumption that the lifetime difference between CP eigenstates is zero. However, recent results from DØ [19] and CDF [20] enforce the hypothesis of different widths for each $B^0_{s,\text{heavy}}$ and $B^0_{s,\text{light}}$ eigenstates of the $B_s^0 \bar{B}_s^0$ system.

It is well known that in the Standard Model (SM), the B_s^0 mesons exist in two eigenstates of CP: $|B_s^{even}\rangle = \frac{1}{\sqrt{2}}(|B_s^0\rangle - |\bar{B}_s^0\rangle)$, and $|B_s^{odd}\rangle = \frac{1}{\sqrt{2}}(|B_s^0\rangle + |\bar{B}_s^0\rangle)$ with $CP\ |B_s^0\rangle = -|\bar{B}_s^0\rangle$. The mass eigenstates at time $t = 0$, B_s^H and B_s^L, (where H means "heavy" and L means "light") are linear combinations of $|B_s^0\rangle$ and $|\bar{B}_s^0\rangle$ too, e.g.:

$$|B_s^H\rangle = p|B_s^0\rangle - q|\bar{B}_s^0\rangle, \qquad |B_s^L\rangle = p|B_s^0\rangle + q|\bar{B}_s^0\rangle, \tag{1.1}$$

with $p^2 + q^2 = 1$. In the SM, these mass eigenstates are approximately the CP eigenstates.

The mass and lifetime differences of the two mass eigenstates are defined by

$$\Delta m = m_H - m_L, \qquad \Delta\Gamma = \Gamma_L - \Gamma_H, \qquad \Gamma = \frac{\Gamma_H + \Gamma_L}{2}, \tag{1.2}$$

where $m_{H,L}$ and $\Gamma_{H,L}$ are the mass and decay width of B_s^H and B_s^L. Width difference in B_s^0 system is expected to be large in comparison with B^0 system, where is almost null. It is also expected that B_s^0 mesons are produced in an equal mixture of B_s^H and B_s^L, and its decay length distribution is described by a function [21] like

$$F(t) = e^{-\Gamma_H t} + e^{-\Gamma_L t} \qquad \text{with} \qquad \Gamma_{L,H} = \Gamma \pm \Delta\Gamma/2, \tag{1.3}$$

instead of just one exponential lifetime $e^{-\Gamma t}$, which is the functional form used in the measurement of the B_s^0 lifetime assuming a single lifetime (or $\Delta\Gamma = 0$).

It can be shown that the B_s^0 lifetime, $\tau(B_s^0)$, obtained from a fit assuming the single lifetime, is related with the total decay width, Γ, and the width difference $\Delta\Gamma$ by the relation

$$\tau(B_s^0) = \frac{1}{\Gamma}\frac{1 + (\Delta\Gamma/2\Gamma)^2}{1 - (\Delta\Gamma/2\Gamma)^2}. \tag{1.4}$$

Determining $\Delta\Gamma_s$ using the expected result from this thesis serves as part of the motivation for this work, although the particular results for this measurement will not be reported here, since this is a subject pending the DØ collaboration's approval, but it is work in progress and can be left as a "further study" note.

1.4 Fermilab

Fermi National Accelerator Laboratory (Fermilab), located in Batavia near Chicago, Illinois, is a U.S. Department of Energy national laboratory specializing in high-energy particle physics. Fermilab's Tevatron is a landmark particle accelerator; at 3.9 miles (6.3 km) in circumference, it is the world's second largest energy particle accelerator (the CERN LHC is 27 kilometres in circumference), you can see a satellite view of the site on Fig. 1.6. In addition to high energy collider physics done at the DØ and Collider Detector at Fermilab (CDF) facilities, Fermilab is also host to a number of smaller fixed target experiments and neutrino experiments, such as MiniBooNE (Mini Booster Neutrino Experiment), SciBooNE (SciBar Booster Neutrino Experiment) and MINOS (Main Injector Neutrino Oscillation Search).

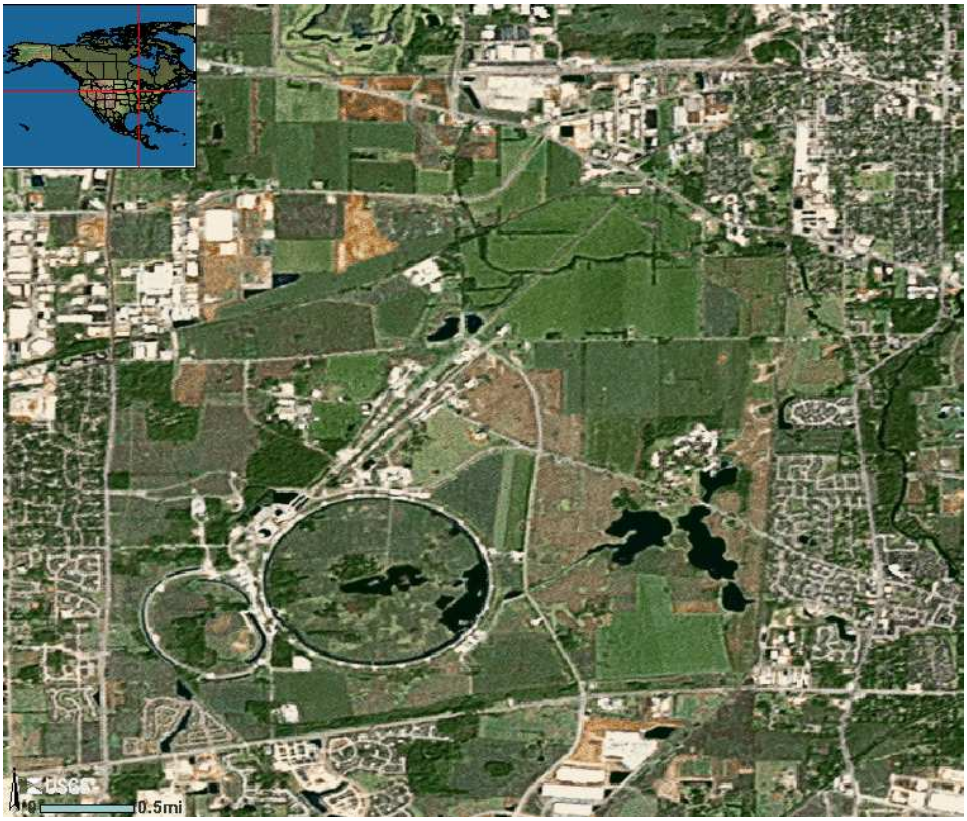

Figure 1.6: A satellite view of Fermilab. The circular structures in the southwest corner (bottom left) are the Main Injector Ring and Tevatron [24].

The four-mile-long Tevatron with its superconducting magnets is the second most powerful particle accelerator in the world (LHC being the most powerful). Traveling at almost the speed of light, protons and antiprotons circle the Tevatron in opposite directions. Physicists coordinate the beams so that they collide at the centers of two 5,000-ton detectors DZero and CDF inside the Tevatron tunnel at energies of 1.96 trillion electron volts (TeV), revealing the conditions of matter in the early universe and its structure at the smallest scale [24].

1.4.1 DØ Collaboration and my service on site

The DØ detector will be described in detail in chapter 3, but as a collaboration, it is an international effort of about 550 physicists from 89 universities and national laboratories from 18 countries. As a PhD student aspiring to become part of such a collaboration, earning the right to use their facilities and data comes with a few obligations. First and foremost, you need to be on site and devote your time and effort to the operation and maintenance of the detector itself.

For that, I was working at DØ for over a year and half. Started off as a Silicon Microstrip Tracker (SMT) shifter, learning the ropes of that particular system while also taking Radiological Worker basic training. The DØ control room works 24/7 and there are always at least 4 people supervising its operations, with on-call experts for each system ready to assist at any time. Once I understood the SMT's operations and dived deeper into the group working on it, I managed to get a spot as a SMT Expert, which added a lot of responsibilities to my work. These included everything from managing the SMT's channel archives, debugging code for the system or subsystems, running tests and studies to improve the SMT's performance, controls and overall operation; testing, repairing and replacing malfunctioning hardware; to developing tools that could be more user friendly to the shifters, the regular operators. Not to mention the one in every five weeks that I was on-call, fully and personally responsible for the SMT's operations and well being for a 7 day period, ready to be on site at anytime needed.

The control room was running short on DAQ shifters, so later on I volunteered to take on that "sidejob", and I believe the control room was happy to get a DAQ shifter with SMT expertise status. The DAQ shifter is a crucial element in the control room, he or she is the one with full control on the data taking, which in turn translates to how efficient the detector is in recording data to disc, and making sure its good data at that.

A DAQ shifter doesn't need to be an expert on any of the other systems

in particular, but a reliable DAQ shifter knows enough of them all to have a better grasp in any situation. DAQ shiters don't call the shots, but undoubtedly they are critical in running the show in the control room. DAQ shifts are for 8 hours, 7 days in a row, once every 3 weeks. You start with the day shift, move onto the evening shift and finish with the night shift, one week at a time. Then you start all over again, and I did this for about 6 months.

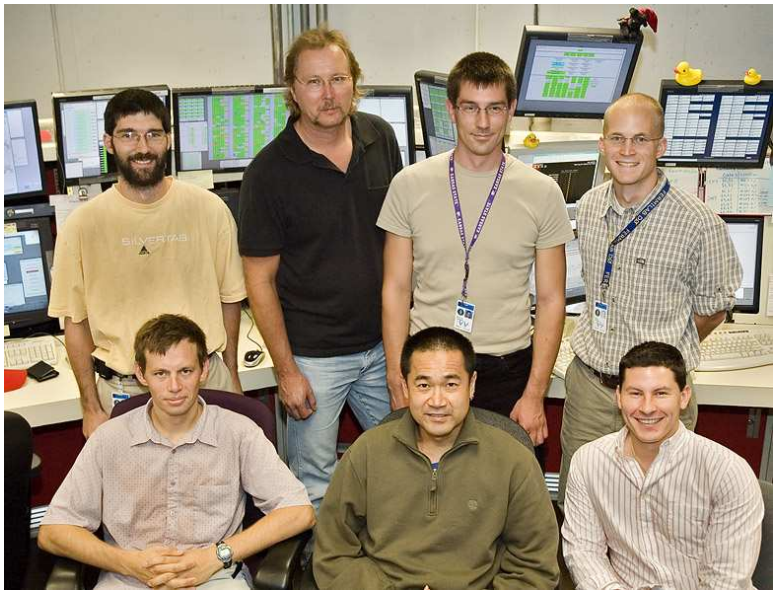

Figure 1.7: DØ Silicon Microstrip Tracker team of experts as of August 2006. Back row, from left: Michele Weber, Mike Utes, Kristian Harder, Derek Strom. Front row, from left: Dmitri Tsybychev, Kazu Hanagaki, Marco Carrasco. Not pictured: Michael Kirby, group leader.

None of the work I performed while I was stationed at DØ had any direct impact on the thesis research presented here. My work there was to help future generations of students get the data they will need, much like I was able to do research on data I didn't take myself, but someone else took before I was even a PhD student. Therefore my contribution to DØ was very satisfying, and even though you get the chance to work with many people from all over the world in order to develop new research and perhaps publish

other articles, my main satisfaction came from the everyday supervising and operation on the SMT system and the DØ detector as a whole, looking to improve its efficiency while knowing that the data being collected would eventually find a young researcher like myself to analyze and make the best use of.

Chapter 2

Theoretical Background

This chapter provides some of the theoretical background needed to interpret the measurement studied in this thesis, most of which was taken from the workshop "B Physics at the Tevatron: Run II and Beyond" [25], held at Fermilab in 2001. The theory of b decays requires some elementary concepts on symmetries and mixing, some knowledge of the standard electroweak theory, and some information on how the b quark is bound into hadrons. The Standard Model, in which quark masses, flavor violation, and CP violation all arise from Yukawa interactions among the quark fields and the Higgs field, still serves as the current foundation for discussing flavor physics.

2.1 CP Violation and the CKM matrix

Let us begin by recalling some of the most elementary aspects of particle physics. Experiments have demonstrated that there are several species, or flavors, of quarks and leptons. They are the down-type quarks (d, s, b), up-type quarks (u, c, t), charged leptons (e, μ, τ), and neutrinos (ν_e, ν_μ, ν_τ). They interact through the exchange of gauge bosons: the weak bosons $W^\pm$ and Z^0, the photon, and the gluons. Experiments of the past decade have verified the $SU(3) \times SU(2) \times U(1)$ gauge structure of elementary particle

interactions, in a comprehensive and very precise way. By comparison, tests of the flavor interactions are not yet nearly as broad or detailed.

The Cabibbo-Kobayashi-Maskawa (CKM) matrix contains a CP violating parameter for three generations. By construction, the CKM matrix is unitary, which implies several relations among its entries and, hence, between CP conserving and CP violating observables. Furthermore, the same construction shows how, in the Standard Model, neutral currents conserve flavor at the tree level, which is known as the Glashow-Iliopoulos-Maiani (GIM) effect.

In the standard, one-doublet, model, we see that flavor and CP violation arise solely through the CKM matrix. Furthermore, in more general settings, the CKM matrix can still arise, but there may be other sources of CP violation as well. If the CKM matrix is the only source of CP violation, there are many relations between CP-conserving and CP violating observables that arise from the fact that V is a unitary matrix.

To emphasize the physical transitions associated with the CKM matrix, it is usually written

$$V = \begin{pmatrix} V_{ud} & V_{us} & V_{ub} \\ V_{cd} & V_{cs} & V_{cb} \\ V_{td} & V_{ts} & V_{tb} \end{pmatrix}, \tag{2.1}$$

so that the entries are labeled by the quark flavors. Because V is unitary, $|V_{ud}|^2 + |V_{us}|^2 + |V_{ub}|^2 = 1$, and similarly for all other rows and columns.

Even more interesting constraints come from the orthogonality of columns (or rows) of a unitary matrix. Taking the first and third columns of V, one has

$$V_{ud}V_{ub}^* + V_{cd}V_{cb}^* + V_{td}V_{tb}^* = 0\,. \tag{2.2}$$

Equation (2.2) says that the three terms in the sum trace out a triangle on the complex plane. Because it is a consequence of the unitarity property of V, this triangle is called the "unitarity triangle,"

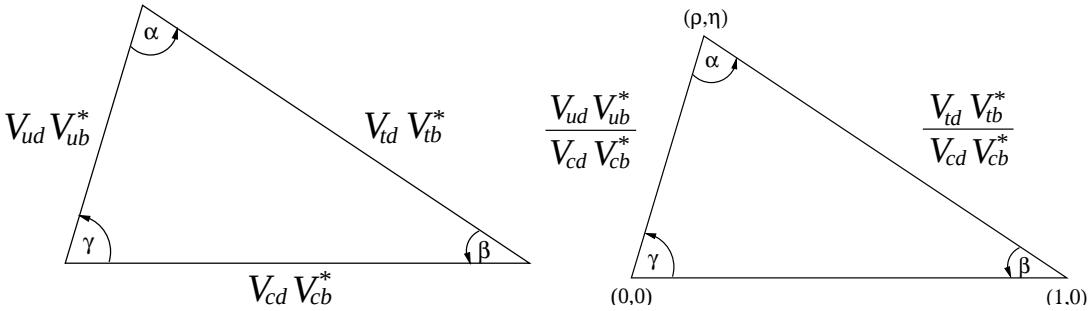

Figure 2.1: The unitarity triangle. The version on the left directly expresses Eq. (2.2). The rescaled version shows the definition of $(\bar{\rho}, \bar{\eta})$.

shown in Fig. 2.1.

The lengths of the sides are simply $|V_{ud}V_{ub}^*|$, etc., and the angles are

$$\alpha = \arg\left[-\frac{V_{td}V_{tb}^*}{V_{ud}V_{ub}^*}\right], \qquad \beta = \arg\left[-\frac{V_{cd}V_{cb}^*}{V_{td}V_{tb}^*}\right], \qquad \gamma = \arg\left[-\frac{V_{ud}V_{ub}^*}{V_{cd}V_{cb}^*}\right]. \tag{2.3}$$

The notation $\beta \equiv \phi_1$, $\alpha \equiv \phi_2$, $\gamma \equiv \phi_3$ is also used. By construction $\alpha + \beta + \gamma = \pi$. The unitarity triangle(s) are useful because they provide a simple, vivid summary of the CKM mechanism. Separate measurements of lengths, through decay and mixing rates, and angles, through CP asymmetries, should fit together. Furthermore, when one combines measurements—from the B, B_s, K, and D systems, as well as from hadronic W decays—all triangles should have the same area and orientation. If there are non-CKM contributions to flavor or CP violation, however, the interpretation of rates and asymmetries as measurements of the sides and angles no longer holds. The triangle built from experimentally defined sides and angles will not fit with the CKM picture.

In the parameterization favored by the Particle Data Book [12]

$$V = \begin{pmatrix} c_{12}c_{13} & s_{12}c_{13} & s_{13}e^{-i\delta_{13}} \\ -s_{12}c_{23} - c_{12}s_{23}s_{13}e^{i\delta_{13}} & c_{12}c_{23} - s_{12}s_{23}s_{13}e^{i\delta_{13}} & s_{23}c_{13} \\ s_{12}s_{23} - c_{12}c_{23}s_{13}e^{i\delta_{13}} & -c_{12}s_{23} - s_{12}c_{23}s_{13}e^{i\delta_{13}} & c_{23}c_{13} \end{pmatrix}, \tag{2.4}$$

where $c_{ij} = \cos\theta_{ij}$ and $s_{ij} = \sin\theta_{ij}$. The real angles θ_{ij} may be chosen so that $0 \leq \theta_{ij} \leq \pi/2$, and the phase δ_{13} so that $0 \leq \delta_{13} < 2\pi$.

A convenient parameterization of the CKM matrix is due to Wolfenstein [1]. It stems from the observation that the measured matrix obeys a hierarchy, with diagonal elements close to 1, and progressively smaller elements away from the diagonal. This hierarchy can be formalized by defining λ, A, ρ, and η via

$$\lambda \equiv s_{12}\,, \qquad A \equiv s_{23}/\lambda^2\,, \qquad \rho + i\eta \equiv s_{13}e^{i\delta_{13}}/A\lambda^3\,. \tag{2.5}$$

From experiment $\lambda \approx 0.22$, $A \approx 0.8$, and $\sqrt{\rho^2+\eta^2} \approx 0.4$, so it is phenomenologically useful to expand V in powers of λ:

$$V = \begin{pmatrix} 1 - \frac{1}{2}\lambda^2 & \lambda & A\lambda^3(\rho - i\eta) \\ -\lambda & 1 - \frac{1}{2}\lambda^2 & A\lambda^2 \\ A\lambda^3(1 - \rho - i\eta) & -A\lambda^2 & 1 \end{pmatrix} + \mathcal{O}(\lambda^4)\,. \tag{2.6}$$

It is customary to rescale Eq. (2.2) by the common factor $A\lambda^3$, to focus on the less well-determined parameters (ρ, η). In the context of the Wolfenstein parameterization, there are many ways to do this. Since we anticipate precision in experimental measurements, and also in theoretical calculations of some important hadronic transition amplitudes, it is useful to choose an exact rescaling. We choose to divide all three terms in Eq. (2.2) by $V_{cd}V_{cb}^*$ and define

$$\bar{\rho} + i\bar{\eta} \equiv -\frac{V_{ud}V_{ub}^*}{V_{cd}V_{cb}^*}. \tag{2.7}$$

Then the rescaled triangle, also shown in Fig. 2.1, has its apex in the complex plane at $(\bar{\rho}, \bar{\eta})$. The angles of the triangle are easily expressed

$$\alpha = \tan^{-1}\left(\frac{\bar{\eta}}{\bar{\eta}^2 + \bar{\rho}(\bar{\rho}-1)}\right), \quad \beta = \tan^{-1}\left(\frac{\bar{\eta}}{1-\bar{\rho}}\right), \quad \gamma = \tan^{-1}\left(\frac{\bar{\eta}}{\bar{\rho}}\right), \tag{2.8}$$

Since $\bar{\eta}$, $\bar{\rho}$, and $1-\bar{\rho}$ could easily be of comparable size, the angles and, thus, the corresponding CP asymmetries could be large.

At the Tevatron there is also copious production of B_s mesons. The corresponding unitarity triangle is

$$V_{us}V_{ub}^* + V_{cs}V_{cb}^* + V_{ts}V_{tb}^* = 0\,, \tag{2.9}$$

replacing the d quark with s. In Eq. (2.9) the first side is much shorter than the other two. Therefore, the opposing angle

$$\beta_s = \arg\left[-\frac{V_{ts}V_{tb}^*}{V_{cs}V_{cb}^*}\right] = \lambda^2\eta + \mathcal{O}(\lambda^4) \tag{2.10}$$

is small, of order one degree. Therefore, the asymmetries in $B_s \to \psi\eta^{(\prime)}$ and $B_s \to \psi\phi$ are much smaller than in the corresponding B decays. On the other hand, this asymmetry is sensitive to new physics in $B_s^0 - \overline{B}_s^0$ mixing. In the standard model mixing is induced by loop processes. When, as here, there is also Cabibbo suppression, it is easy for the non-standard phenomena to compete. Thus, in the short term a measurement of β_s represents a search for new physics, whereas in the long term it would be a verification of the CKM picture.

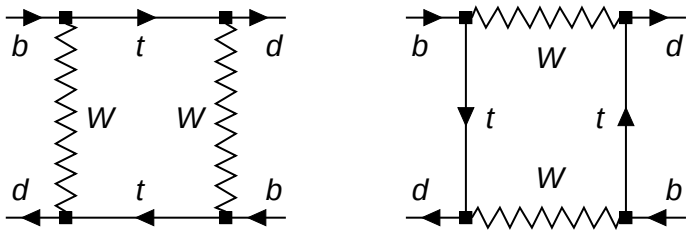

Figure 2.2: Standard Model box diagrams inducing $B^0_d - \overline{B}^0_d$ mixing.

2.2 $B^0_s - \overline{B}^0_s$ mixing

In the following, the notation B^0 represents either of the two neutral B meson species with the standard convention that B^0 ($\overline{B}^0$) contains a $\overline{b}$ antiquark (a b quark). $B^0 - \overline{B}^0$ mixing refers to transitions between the two flavor eigenstates $|B^0\rangle$ and $|\overline{B}^0\rangle$. In the Standard Model $B^0 - \overline{B}^0$ mixing is caused by the fourth order flavor-changing weak interaction described by the box diagrams in Fig. 2.2.

Such transitions are called $|\Delta B| = 2$ transitions, because they change the bottom quantum number by two units. In the Standard Model $|\Delta B| = 2$ amplitudes are small, so measurements of $B^0 - \overline{B}^0$ mixing could easily be sensitive to new physics.

$B^0 - \overline{B}^0$ mixing induces oscillations between B^0 and $\overline{B}^0$. An initially produced B^0 or $\overline{B}^0$ evolves in time into a superposition of B^0 and $\overline{B}^0$. Let $|B^0(t)\rangle$ denote the state vector of a B meson which is tagged as a B^0 at time $t = 0$, i.e., $|B^0(t = 0)\rangle = |B^0\rangle$. Likewise $|\overline{B}^0(t)\rangle$ represents a B meson initially tagged as a $\overline{B}^0$. The time evolution of these states is governed by a Schrödinger equation:

$$\frac{\mathrm{d}}{\mathrm{d}\,t}\begin{pmatrix} |B(t)\rangle \\ |\overline{B}(t)\rangle \end{pmatrix} = \left(M - i\,\frac{\Gamma}{2}\right)\begin{pmatrix} |B(t)\rangle \\ |\overline{B}(t)\rangle \end{pmatrix}. \tag{2.11}$$

The *mass matrix* M and the *decay matrix* Γ are t-independent, Hermitian

2×2 matrices. CPT invariance implies that

$$M_{11} = M_{22}\,, \qquad\qquad \Gamma_{11} = \Gamma_{22}\,. \tag{2.12}$$

$|\Delta B| = 2$ transitions induce non-zero off-diagonal elements in (2.11), so that the mass eigenstates of the neutral B meson are different from the flavor eigenstates $|B^0\rangle$ and $|\overline{B}^0\rangle$. The mass eigenstates are defined as the eigenvectors of $M - i\,\Gamma/2$. We express them in terms of the flavor eigenstates as

$$\begin{aligned} \text{Lighter eigenstate:} \quad |B_L\rangle &= p|B^0\rangle + q|\overline{B}^0\rangle\,, \\ \text{Heavier eigenstate:} \quad |B_H\rangle &= p|B^0\rangle - q|\overline{B}^0\rangle\,, \end{aligned} \tag{2.13}$$

with $|p|^2 + |q|^2 = 1$. Note that, in general, $|B_L\rangle$ and $|B_H\rangle$ are not orthogonal to each other.

The time evolution of the mass eigenstates is governed by the two eigenvalues $M_H - i\,\Gamma_H/2$ and $M_L - i\,\Gamma_L/2$:

$$|B_{H,L}(t)\rangle = e^{-(iM_{H,L} + \Gamma_{H,L}/2)t}\,|B_{H,L}\rangle\,, \tag{2.14}$$

where $|B_{H,L}\rangle$ (without the time argument) denotes the mass eigenstates at time $t = 0$: $|B_{H,L}\rangle = |B_{H,L}(t=0)\rangle$. We adopt the following definitions for the average mass and width and the mass and width differences of the B meson eigenstates:

$$\begin{aligned} m &= \frac{M_H + M_L}{2} = M_{11}\,, & \Gamma &= \frac{\Gamma_L + \Gamma_H}{2} = \Gamma_{11}\,, \\ \Delta m &= M_H - M_L\,, & \Delta\Gamma &= \Gamma_L - \Gamma_H\,. \end{aligned} \tag{2.15}$$

Δm is positive by definition. In our convention the Standard Model prediction for $\Delta\Gamma$ is positive.

We can find the time evolution of $|B(t)\rangle$ and $|\overline{B}(t)\rangle$ as follows. We first

invert (2.13) to express $|B^0\rangle$ and $|\overline{B}^0\rangle$ in terms of the mass eigenstates and using their time evolution in (2.14):

$$\begin{aligned} |B^0(t)\rangle &= \frac{1}{2p}\left[\, e^{-iM_L t-\Gamma_L t/2}\,|B_L\rangle \,+\, e^{-iM_H t-\Gamma_H t/2}\,|B_H\rangle\,\right], \\ |\overline{B}^0(t)\rangle &= \frac{1}{2q}\left[\, e^{-iM_L t-\Gamma_L t/2}\,|B_L\rangle \,-\, e^{-iM_H t-\Gamma_H t/2}\,|B_H\rangle\,\right]. \end{aligned} \tag{2.16}$$

These expressions will be very useful in the discussion of B_s mixing. With (2.13) we next eliminate the mass eigenstates in (2.16) in favor of the flavor eigenstates:

$$\begin{aligned} |B^0(t)\rangle &= \quad g_+(t)\,|B^0\rangle + \frac{q}{p}\,g_-(t)\,|\overline{B}^0\rangle\,, \\ |\overline{B}^0(t)\rangle &= \frac{p}{q}\,g_-(t)\,|B^0\rangle + \quad g_+(t)\,|\overline{B}^0\rangle\,, \end{aligned} \tag{2.17}$$

where

$$\begin{aligned} g_+(t) &= e^{-imt}\,e^{-\Gamma t/2}\left[\quad \cosh\frac{\Delta\Gamma\, t}{4}\,\cos\frac{\Delta m\, t}{2} - i\sinh\frac{\Delta\Gamma\, t}{4}\,\sin\frac{\Delta m\, t}{2}\,\right], \\ g_-(t) &= e^{-imt}\,e^{-\Gamma t/2}\left[-\sinh\frac{\Delta\Gamma\, t}{4}\,\cos\frac{\Delta m\, t}{2} + i\cosh\frac{\Delta\Gamma\, t}{4}\,\sin\frac{\Delta m\, t}{2}\right] \end{aligned} \tag{2.18}$$

Note that—owing to $\Delta\Gamma \neq 0$—the coefficient $g_+(t)$ has no zeros, and $g_-(t)$ vanishes only at $t = 0$. Hence an initially produced B^0 will never turn into a pure $\overline{B}^0$ or back into a pure B^0.

2.3 Heavy Quark Effective Theory

The dominant weak decays of hadrons containing a heavy quark, c or b, are caused by the decay of the heavy quark. In the limit of a very large mass m_Q of a heavy quark Q the parton picture of the hadron decay should set in, where the inclusive decay rates of hadrons, containing Q, mesons $(Q\bar{q})$

and baryons (Qqq), are all the same and equal to the inclusive decay rate $\Gamma_{parton}(Q)$ of the heavy quark. Yet, the known inclusive decay rates are conspicuously different for different hadrons, especially for charmed hadrons, whose lifetimes span a range of more than one order of magnitude from the shortest $\tau(\Omega_c) = 0.064 \pm 0.020$ ps to the longest $\tau(D^+) = 1.057 \pm 0.015$ ps, while the differences of lifetime among b hadrons are substantially smaller. The relation between the relative lifetime differences for charmed and b hadrons reflects the fact that the dependence of the inclusive decay rates on the light quark-gluon 'environment' in a particular hadron is a pre-asymptotic effect in the parameter m_Q, which effect vanishes as an inverse power of m_Q at large mass. A theoretical framework for systematic description of the leading at $m_Q \to \infty$ term in the inclusive decay rate $\Gamma_{parton}(Q) \propto m_Q^5$ as well as of the terms relatively suppressed by inverse powers of m_Q is provided by the Operator Product Expansion (OPE) in m_Q^{-1}. A very successful theory to describe the decay of the meson containing a heavy and a light quark is the Heavy Quark Effective Theory (HQET). In the HQET the Lagrangian is expressed in an OPE expansion. In practice only the b and c quarks have masses large enough that HQET is valid, it does not apply to the top quark since it decays before hadronization. Using this theory, the B_s/B^0 lifetime ratio has been calculated to be $B_s/B^0 = 1 \pm 0.01$. This is a very precise prediction, hence lifetime ratios can be a powerful tool to test the Standard Model.

In section 1.2, it was mentioned that the spectator model predicts that all hadrons with the same heavy flavor content have identical lifetimes. In the spectator model, a heavy quark (b or c) in a hadron is bound to the lighter "spectator" quark(s). For as long as the spectator holds, the decay is governed by the weak decay of the Q, and, for this reason, the lifetime of all hadrons containing Q are the same and equal to that of a free Q. However lifetimes of B hadrons have been experimentally observed to follow a hierarchy scheme:

$$\tau_{B_c} < \tau_{barion} < \tau_{B_s} \leq \tau_{B_d} < \tau_{B_u} \tag{2.19}$$

On the phenomenological level, the main mechanism generating the observed hierarchy of B hadrons are Pauli interference, Weak annihilation, and Weak Exchange.

Chapter 3

The Run IIa DØ Detector

In the present chapter the proton-antiproton production is described followed by a short description of their acceleration on and into the Tevatron. After this we find a description of our experimental setup: the DØ Detector, summarizing each of its subsystem's specifications and purposes. The publication "The Upgraded DØ Detector" [26] was used and can be referred to in order to revise the specs in greater detail.

The DØ detector is one of two multi-purpose physics detectors located on the Tevatron accelerator at Fermilab, Batavia, IL, USA. The DØ experiment was proposed in 1983 to study proton-antiproton collisions at a center-of-mass energy of 1.8 TeV at the Fermilab Tevatron collider. The focus of the experiment was the study of high mass states and large p_T phenomena. The detector performed very well during Run I of the Tevatron, 1992–1996, leading to the discovery of the top quark and measurement of its mass, a precision measurement of the mass of the W boson, detailed analysis of gauge boson couplings, studies of jet production, and greatly improved limits on the production of new phenomena such as leptoquarks and supersymmetric particles, among many other accomplishments.

During Run I, the Tevatron operated using six bunches each of protons and antiprotons, with 3500 ns between bunch crossings and a center-of-mass

energy of 1.8 TeV. The peak luminosity was typically 1–2$\times 10^{31}$ cm^{-2}s^{-1} and approximately 120 pb^{-1} of data were recorded by DØ. Following the completion of the new Main Injector and associated Tevatron upgrades, the collider began running again in 2001. In Run II, which began in March 2001, the Tevatron is operated with 36 bunches of protons and antiprotons with a bunch spacing of 396 ns and at an increased center-of-mass energy of 1.96 TeV. The instantaneous luminosity increased by more than a factor of ten to greater than 10^{32} cm^{-2}s^{-1}.

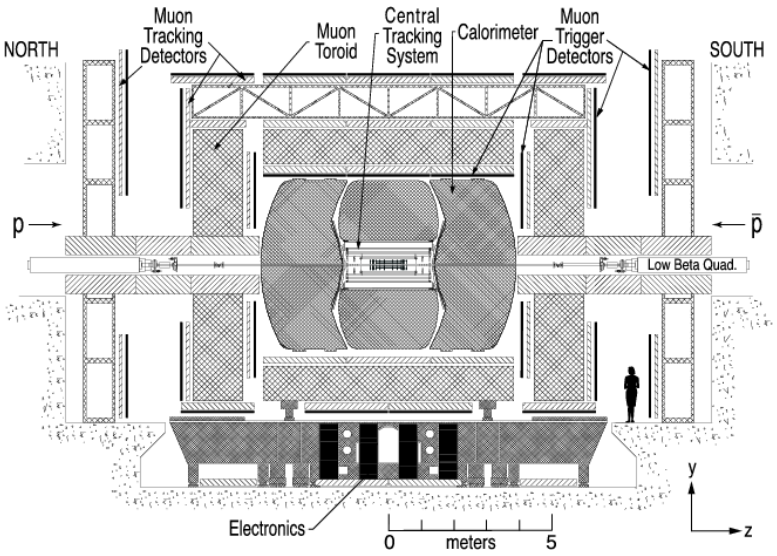

Figure 3.1: Diagram of the upgraded DØ detector, as installed in the collision hall and viewed from inside the Tevatron ring. The forward proton detector is not shown. The detectors in the central region of the detector are shown in Fig. 3.3.

The detector consists of three major subsystems: central tracking detectors, uranium/liquid-argon calorimeters, and a muon spectrometer. The central tracking system was completely replaced from Run I to Run II. The old system lacked a magnetic field and suffered from radiation damage, and improved tracking technologies are now available. The new system includes a silicon microstrip tracker and a scintillating-fiber tracker located within a 2 T

solenoidal magnet. The silicon microstrip tracker is able to identify displaced vertices for b-quark tagging. The magnetic field enables measurement of the energy to momentum ratio (E/p) for electron identification and calorimeter calibration, opens new capabilities for tau lepton identification and hadron spectroscopy, and allows precision muon momentum measurement. Between the solenoidal magnet and the central calorimeter and in front of the forward calorimeters, preshower detectors were added for improved electron identification. In the forward muon system, proportional drift chambers were replaced by mini drift tubes and trigger scintillation counters that can withstand the harsh radiation environment and additional shielding was added. In the central region, scintillation counters were added for improved muon triggering. A forward proton detector for the study of diffractive physics was also added. A side view of the upgraded DØ detector is shown in Figure 3.1.

3.1 p and $\overline{p}$ production

The initial stage in the production of protons and antiprotons is a Cockcroft-Walton pre-accelerator. Here hydrogen atoms are ionised to make H^- ions, which are then accelerated through the iniial stages of the accelerator complex. The Cockcroft-Walton machine accelerates the ions to an energy of about 750 keV, before feeding them into a linear accelerator where they are accelerated to 400 MeV. After this stage the electrons are removed from the ions to leave protons, by passing the beam of ions through a carbon foil. The protons then enter a synchrotron accelerator, known as the Booster, and are accelerated to around 8 GeV before entering the Main Injector, a synchrotron with a 3km circumference. The Main Injector sends protons into the Tevatron, at an energy of 150 GeV, or to the Antiproton Source, at 120 GeV. To produce antiprotons, the protons at 120 GeV are collided witha nickel target. These collisions produce antiprotons as well as other particles, so the antiprotons are separated using bending magnets as a charge-mass

spectrometer. Antiprotons are stored in the accumulator ring until they can be sent to the Main Injector, from which they are injected into the Tevatron.

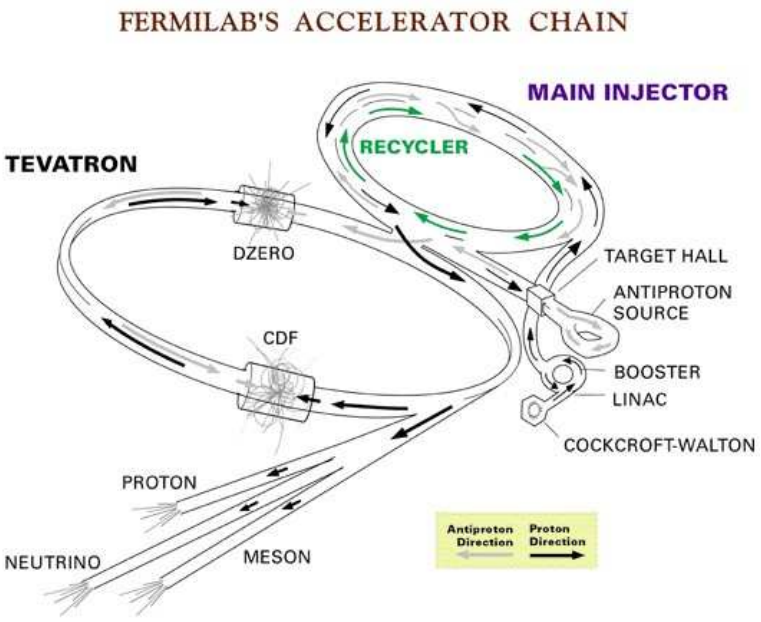

Figure 3.2: Fermilab's Accelerator Rings [24].

3.2 The Tevatron

The Tevatron provides the final acceleration stage before collisions. It is a superconducting synchrotron with a circumference of six kilometers, and while the data for this thesis were taken, it was the highest energy accelerator in the world. The protons and antiprotons are accelerated from 150 GeV to their collision energy of 980 GeV. Once collision energy is reached, the beams are focused for collisions in the two detectors. The protons and antiprotons circle in bunches, with bunch crossings occurring every 396 ns in the center of the detectors. The beams continue to circle and collisions are recorded for several hours, during a period known as a store. Collisions and loss

of particles from the beams reduce the luminosity, and severals hours after collisions are initiated, the beams are dumped and a new store is started.

3.3 The DØ Detector Coordinate System

A right-handed system of coordinates with origin at the center of the detector is used. The z-axis lies along the beam axis, pointing in the direction of the proton beam, and the y-axis points vertically upward. This means that the x-axis points away from the centre of the Tevatron ring. Often spherical polar coordinates are used, with the radial coordinate r lying perpendicular to the beam direction and the azimuthal angle given by $\phi = arctan(y/x)$. The polar angle $\theta = arctan(r/z)$ is usually replaced by the *pseudorapidity*, η, which is defined as

$$\eta = -ln(tan\frac{\theta}{2}) \tag{3.1}$$

The pseudorapidity is an approximation of the rapidity

$$y = \frac{1}{2}ln(\frac{E + p_z}{E - p_z}) \tag{3.2}$$

for E¿¿m, where E, p and m are the energy, momentum and mass of a particle respectively. The two quantities are identical for massless particles.

The term *transverse* refers to the (x, y) plane, and quantitties are often measured in this plane, such as the transverse momentum, $p_T = psin\theta$, and the transverse energy, $E_T = Esin\theta$. The term *forward* refers to points at large $|z|$.

3.4 Central Tracking System

Excellent tracking in the central region is necessary for studies of top quark, electroweak, and b physics and to search for new phenomena, including the

Higgs boson. The central tracking system consists of the silicon microstrip tracker (SMT) and the central fiber tracker (CFT) surrounded by a solenoidal magnet. It surrounds the DØ beryllium beam pipe, which has a wall thickness of 0.508 mm and an outer diameter of 38.1 mm, and is 2.37 m long. The two tracking detectors locate the primary interaction vertex with a resolution of about 35 μm along the beamline. They can tag b-quark jets with an impact parameter resolution of better than 15 μm in $r-\phi$ for particles with transverse momentum $p_T > 10$ GeV/c at $|\eta| = 0$. The high resolution of the vertex position allows good measurement of lepton p_T, jet transverse energy (E_T), and missing transverse energy $\not\!\!E_T$. Calibration of the electromagnetic calorimeter using E/p for electrons is now possible.

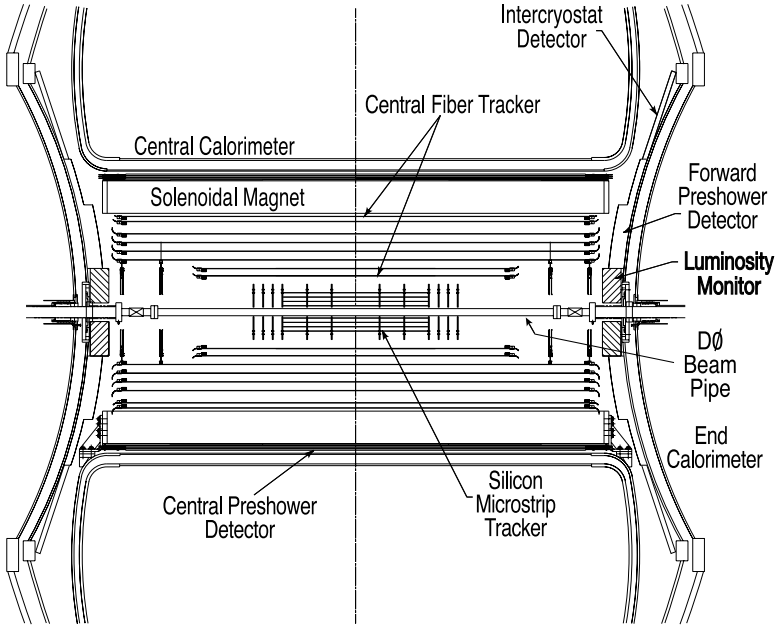

Figure 3.3: Cross-sectional view of the new central tracking system in the $x-z$ plane. Also shown are the locations of the solenoid, the preshower detectors, luminosity monitor, and the calorimeters.

Both the SMT and CFT provide tracking information to the trigger. The SMT provides signals to the Level 2 and 3 trigger systems and is used

to trigger on displaced vertices from b-quark decay. The CFT provides a fast and continuous readout of discriminator signals to the Level 1 trigger system; upon a Level 1 trigger accept, track information based on these signals is sent to Level 2. The Level 3 trigger receives a slower readout of the CFT's digitized analog signals, in addition to the discriminator information available at Level 1 and Level 2. A schematic view of the central tracking system is shown in Figure 3.3.

3.4.1 Silicon Microstrip Tracker (SMT)

The SMT provides both tracking and vertexing over nearly the full η coverage of the calorimeter and muon systems. Design of the detector, electronics, and cooling are, in large part, dictated by the accelerator environment. The length of the interaction region ($\sigma \approx 25$ cm) sets the length scale of the device. With a long interaction region, it is a challenge to deploy detectors such that the tracks are generally perpendicular to detector surfaces for all η. This led to a design of barrel modules interspersed with disks in the center and assemblies of disks in the forward regions. The barrel detectors primarily measure the $r - \phi$ coordinate and the disk detectors measure $r - z$ as well as $r - \phi$. Thus vertices for particles at high η are reconstructed in three dimensions by the disks, and vertices of particles at small values of η are measured in the barrels and central fiber tracker. This design poses difficult mechanical challenges in arranging the detector components and minimizing dead areas while providing sufficient space for cooling and cables.

An isometric view of the SMT is shown in Figure 3.4. The detector has six barrels in the central region. Each barrel has four silicon readout layers. The silicon modules installed in the barrels are called "ladders." Layers 1 and 2 have twelve ladders each; layers 3 and 4 have twenty-four ladders each, for a total of 432 ladders. Each barrel is capped at high $|z|$ with a disk of twelve double-sided wedge detectors, called an "F-disk." Forward of the three disk/barrel assemblies on each side is a unit consisting of three F-disks. In the

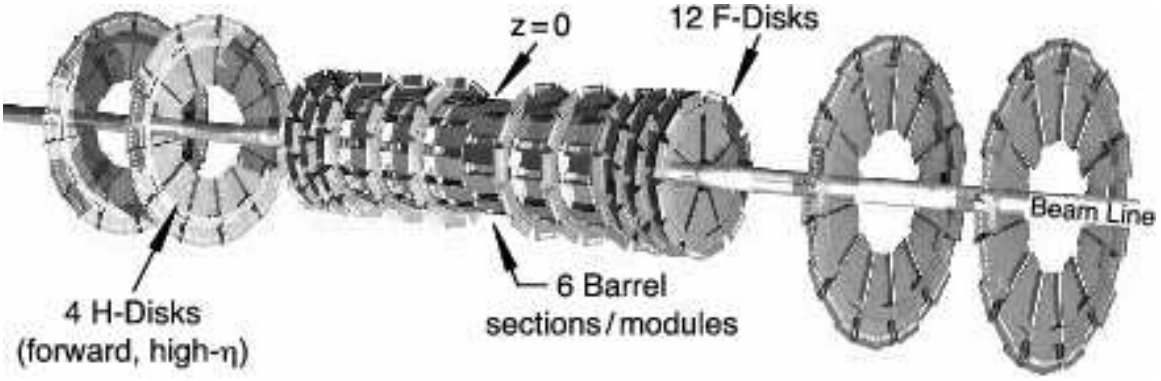

Figure 3.4: The disk/barrel design of the SMT.

far forward regions, two large-diameter disks, "H-disks," provide tracking at high $|\eta|$. Twenty-four full wedges, each consisting of two back-to-back single-sided "half" wedges, are mounted on each H-disk. There are 144 F-wedges and 96 full H-wedges in the tracker; each side of a wedge (upstream and downstream) is read out independently. There is a grand total of 912 readout modules, with 792,576 channels. The centers of the H-disks are located at $|z| = 100.4,\ 121.0$ cm; the F-disks are at $|z| = 12.5,\ 25.3,\ 38.2,\ 43.1,\ 48.1,$ and 53.1 cm. The centers of the barrels are at $|z| = 6.2,\ 19.0,\ 31.8$ cm. The SMT is read out by custom-made 128-channel SVXIIe readout chips.

The SMT uses a combination of single-sided (SS), double-sided (DS), and double-sided double-metal (DSDM) technologies. Silicon sensors were obtained from three manufacturers. Single-sided and double-sided devices were produced from high resistivity 4" silicon wafers, with crystal orientation <111> and <100>. The 90° stereo sensors used in layers 1 and 3 of the four centermost barrels are DSDM sensors, manufactured using <100> 6" wafers. Isolation on the n-side of all double-sided sensors is provided by p-stop implants. All traces are biased using polysilicon resistors. Table 3.1 shows the sensor types used in the SMT and their locations. A sketch of a double-sided 2° ladder with nine SVXIIe readout chips is shown in Figure 3.5.

Table 3.1: Characteristics and deployment of various sensor types in the SMT. i indicates the length of the inner H-disk sensor; o is the length of the outer H-disk sensor.

Module	Type	Layer	Pitch (μm) p/n	Length (cm)	Inner radius (cm)	Outer radius (cm)
F-disks	DS	–	50/62.5	7.93	2.57	9.96
H-disks	SS	–	40 80 readout	7.63^i 6.33^o	9.5	26
Central barrels (4)	DSDM	1, 3	50/153.5	12.0	2.715	7.582
	DS	2, 4	50/62.5	6.0	4.55	10.51
Outer barrels (2)	SS	1, 3	50	6.0	2.715	7.582
	DS	2, 4	50/62.5	6.0	4.55	10.51

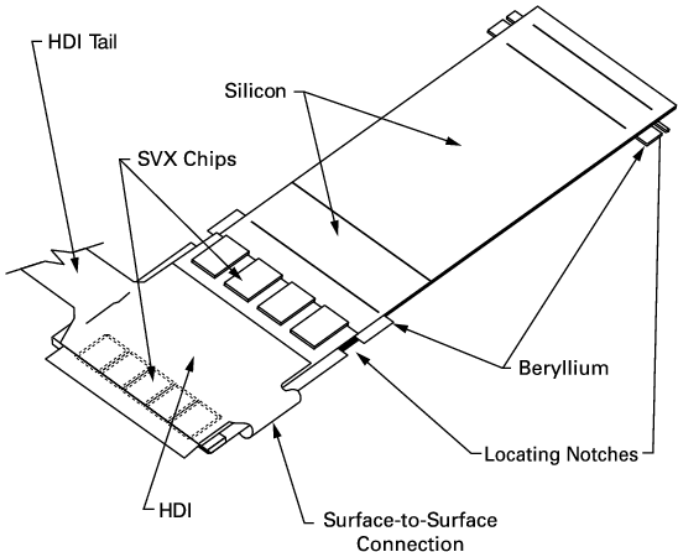

Figure 3.5: Double-sided ladder design, n-side. The SVXIIe readout chips shown as dashed lines are located on the p-side of the ladder.

3.4.2 Central Fiber Tracker (CFT)

The CFT consists of scintillating fibers mounted on eight concentric support cylinders and occupies the radial space from 20 to 52 cm from the center of the beampipe. To accomodate the forward SMT H-disks, the two innermost cylinders are 1.66 m long; the outer six cylinders are 2.52 m long. The outer cylinder provides coverage for $|\eta| \lesssim 1.7$. Each cylinder supports one doublet layer of fibers oriented along the beam direction (z) and a second doublet layer at a stereo angle in ϕ of $+3^\circ$ (u) or -3° (v). Doublet layers with fibers oriented along the beam axis are referred to as axial layers, while the doublet layers oriented at small angles are referred to as stereo layers. From the smallest cylinder outward, the fiber doublet orientation is $zu - zv - zu - zv - zu - zv - zu - zv$. The scintillating fibers are coupled to clear fiber waveguides which carry the scintillation light to visible light photon counters (VLPCs) for read out. The small fiber diameter (835 μm) gives the CFT an inherent doublet layer resolution of about 100 μm as long as the location of the individual fibers is known to better than 50 μm.

Discriminator signals from the axial doublet layers are used to form a fast Level 1 hardware trigger based upon the number of track candidates above specified p_T thresholds (with a minimum threshold of 1.5 GeV/c). Level 1 track candidates are used by the Level 2 trigger, while the Level 3 trigger uses the full CFT readout information.

The scintillating fibers, including the cladding, are 835 μm in diameter and 1.66 or 2.52 m in length. They are optically connected to clear fiber waveguides of identical diameter which are 7.8 to 11.9 m long. The fibers have a multi-clad structure consisting of a core surrounded by two claddings. The scintillating fiber is structurally and chemically similar to the clear fiber, but contains fluorescent dyes. The CFT uses about 200 km of scintillating fiber and 800 km of clear fiber.

Light production in the fibers is a multistep process. The base core material is polystyrene (PS). The PS is doped with the organic fluorescent

dye paraterphenyl (pT) to about 1% by weight. Excitations in the PS are rapidly transferred to the pT via a non-radiative dipole-dipole interaction. pT has a rapid fluorescence decay (a few nanoseconds) and a short emission wavelength ($\approx$ 340 nm). The mean free path of the emitted light is only a few hundred microns in the PS. To get the light out of the detector, a secondary wave-shifter dye, 3-hydroxyflavone (3HF), is added at a low concentration (1500 ppm). The 3HF is spectrally matched to the pT but has minimal optical self-absorption. The 3HF absorbs the 340 nm radiation from the pT and re-emits it at 530 nm which is well-transmitted in PS.

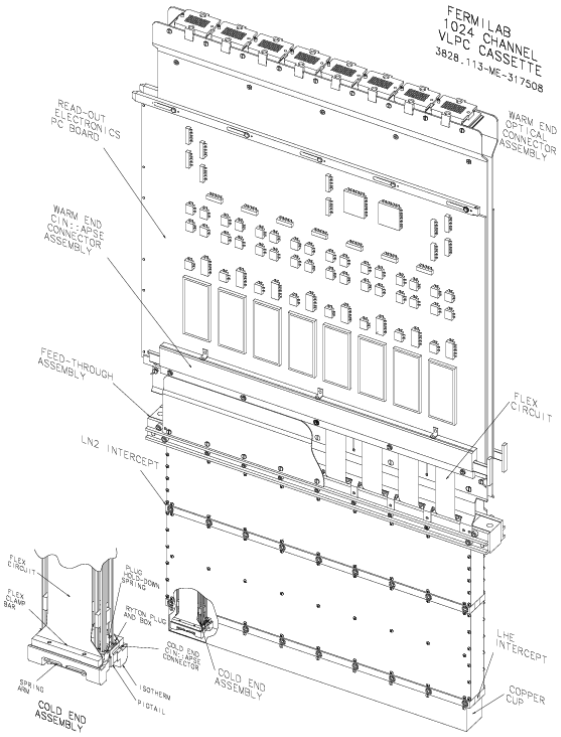

Figure 3.6: A VLPC cassette supporting AFE readout boards as viewed from the left side. The VLPC hybrids are located on the isotherms housed inside the copper cup shown at the bottom of the figure.

The light generated by the passage of charged particles through the scin-

tillating fibers of the CFT is converted into electrical signals by the VLPCs housed in the VLPC cassettes, see figure 3.6. VLPCs are impurity-band silicon avalanche photodetectors that operate nominally at 9 K, and are capable of detecting single photons. They provide fast response, excellent quantum efficiency ($\geq$75%), high gain (22,000 to 65,000), low gain dispersion, and the capability of functioning in a high background environment.

3.5 Solenoidal Magnet

The superconducting solenoidal magnet was designed to optimize the momentum resolution, $\delta p_T/p_T$, and tracking pattern recognition within the constraints imposed by the Run I detector. The overall physical size of the magnet was determined by the available space within the central calorimeter vacuum vessel: 2.73 m in length and 1.42 m in diameter. We selected a central field of 2 T after considering the momentum resolution and tracking pattern recognition, the available space, and the thickness of the cryostat which depends on the thicknesses of the conductor and support cylinder.

In addition, the magnet is required *i*) to operate safely and stably at either polarity, *ii*) to have a uniform field over as large a percentage of the volume as practical, *iii*) to be as thin as possible to make the tracking volume as large as possible, *iv*) to have an overall thickness of approximately $1X_0$ at $\eta = 0$ to optimize the performance of the central preshower detector mounted on the outside of the solenoid cryostat, and *v*) to quench safely without a protection resistor (although one is installed to reduce the recool time after an inadvertent fast dump).

Services such as cryogens, magnet current buses, and vacuum pumpout and relief must reach the magnet from the control dewar through the narrow space (7.6 cm) between the central and end calorimeter vacuum vessels. The magnet system is controlled remotely, including cool down, energization, deenergization for field reversal, quench recovery, and warmup, without access

Table 3.2: Major parameters of the solenoid

Central field	2.0 T
Operating current	4749 A
Cryostat warm bore diameter	1.067 m
Cryostat length	2.729 m
Stored energy	5.3 MJ
Inductance	0.47 H
Cooling	Indirect, 2-phase forced flow helium
Cold mass	1460 kg
Conductor	18-strand Cu:NbTi, cabled
Conductor stabilizer	High purity aluminum
Thickness	0.87 X_0
Cooldown time	$\leq$ 40 hours
Magnet charging time	15 minutes
Fast discharge time constant	11 seconds
Slow discharge time constant	310 seconds
Total operating heat load	15 W plus 0.8 g/s liquefaction
Operating helium mass flow	1.5 g/s

to the magnet cryostat, service chimney, or control dewar.

The major parameters of the solenoid design are listed in Table 3.2. A perspective view of the solenoid inside the central calorimeter with its chimney and control dewar is shown in Figure 3.7. The solenoid, along with its cryostat, control dewar, and connecting service chimney, was manufactured by Toshiba Corp. in Yokohama, Japan. The system was specified to operate safely and reliably over a twenty-year lifetime with up to 150 cool-down cycles, 2500 energization cycles, and 400 fast dumps.

3.6 Preshower Detectors

The preshower detectors aid in electron identification and background rejection during both triggering and offline reconstruction. They function as

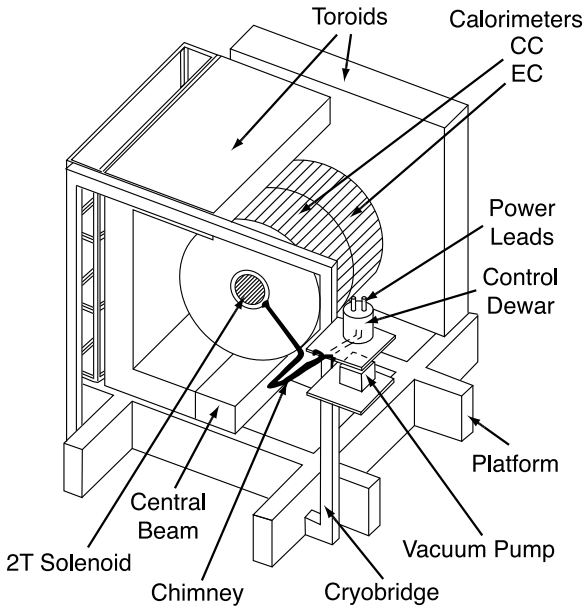

Figure 3.7: Perspective view of the solenoid inside the central calorimeter. One end calorimeter, several muon chambers, and parts of the toroids have been omitted for clarity. Also shown are the service chimney and control dewar.

calorimeters as well as tracking detectors, enhancing the spatial matching between tracks and calorimeter showers. The detectors can be used offline to correct the electromagnetic energy measurement of the central and end calorimeters for losses in the solenoid and upstream material, such as cables and supports. Their fast energy and position measurements allow preshower information to be included in the Level 1 trigger. The central preshower detector (CPS) covers the region $|\eta| < 1.3$ and is located between the solenoid and the central calorimeter with an inner radius of 28.25" and an outer radius of 29.21". The two forward preshower detectors (FPS) cover $1.5 < |\eta| < 2.5$ and are attached to the faces of the end calorimeters. The preshower detectors can be seen in Figure 3.3.

3.7 Calorimetry

The DØ calorimeter system consists of three sampling calorimeters (primarily uranium/liquid-argon) and an intercryostat detector.

3.7.1 Calorimeters

The calorimeters were designed to provide energy measurements for electrons, photons, and jets in the absence of a central magnetic field (as was the case during Run I of the Tevatron), as well as assist in identification of electrons, photons, jets, and muons and measure the transverse energy balance in events. The calorimeters themselves are unchanged from Run I. They are illustrated in Figure 3.8.

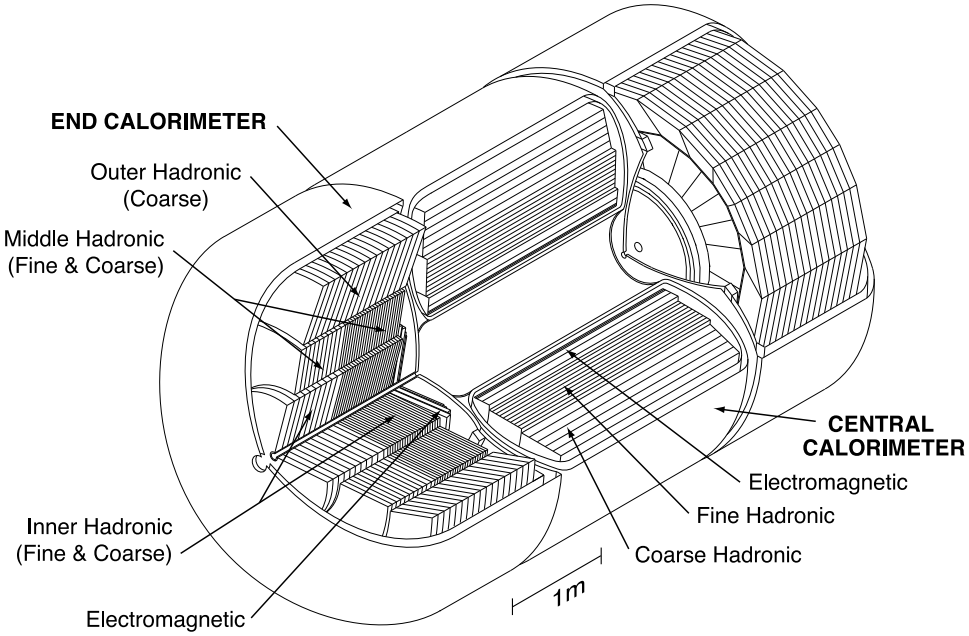

Figure 3.8: Isometric view of the central and two end calorimeters.

As shown in Figure 3.9, the central calorimeter (CC) covers $|\eta| \lesssim 1$ and the two end calorimeters, ECN (north) and ECS (south), extend coverage to

$|\eta| \approx 4$. Each calorimeter contains an electromagnetic section closest to the interaction region followed by fine and coarse hadronic sections. The active medium for the calorimeters is liquid argon and each of the three calorimeters (CC, ECN, and ECS) is located within its own cryostat that maintains the detector temperature at approximately 90 K. Different absorber plates are used in different locations. The electromagnetic sections (EM) use thin plates (3 or 4 mm in the CC and EC, respectively), made from nearly pure depleted uranium. The fine hadronic sections are made from 6-mm-thick uranium-niobium (2%) alloy. The coarse hadronic modules contain relatively thick (46.5 mm) plates of copper (in the CC) or stainless steel (EC).

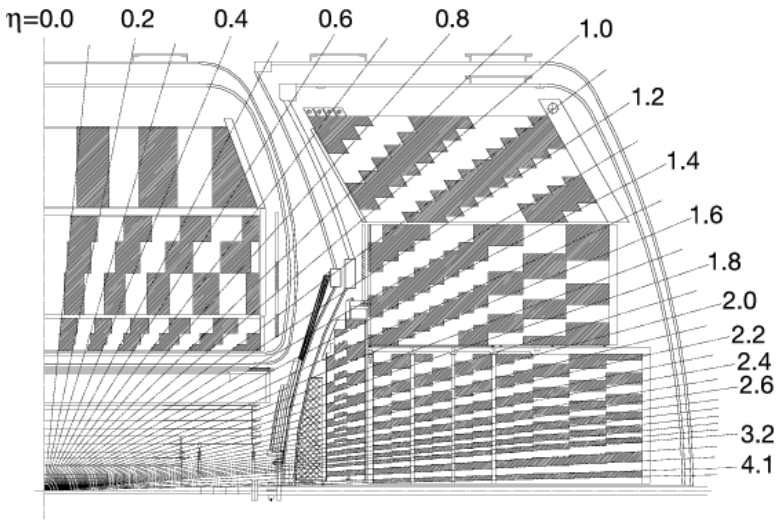

Figure 3.9: Schematic view of a portion of the DØ calorimeters showing the transverse and longitudinal segmentation pattern. The shading pattern indicates groups of cells ganged together for signal readout. The rays indicate pseudorapidity intervals from the center of the detector.

Since the calorimeter system is contained in three separate cryostats, it provides incomplete coverage in the pseudorapidity region $0.8 <| \eta |< 1.4$, as can be seen in Figure 3.9. In addition, there is substantial unsampled material in this region, degrading the energy resolution. To address this

problem, additional layers of sampling have been added. Within the central and end cryostats are single-cell structures called massless gaps — calorimeter readout cells in front of the first layer of uranium. The Intercryostat Detector (ICD) provides scintillator sampling that is attached to the exterior surfaces of the end cryostats. It covers the region $1.1 <| \eta |< 1.4$. The massless gaps are those used in Run I, while the ICD is a replacement for a similar detector in the same location (the Run I detector had approximately twice the coverage in η; the space was needed for SMT and CFT cabling in Run II).

The ICD is a series of 0.5"-thick scintillating tiles (Bicron BC-400) enclosed in light-tight aluminum boxes. Each tile covers an area of $\Delta\eta \times \Delta\phi \approx 0.3 \times 0.4$ and is divided into twelve subtiles, as shown in Figure 3.10, each covering $\Delta\eta \times \Delta\phi \approx 0.1 \times 0.1$. Because of the cryogenic services for the solenoid, one half of a tile is missing at the south end of the detector, giving a total of 378 channels.

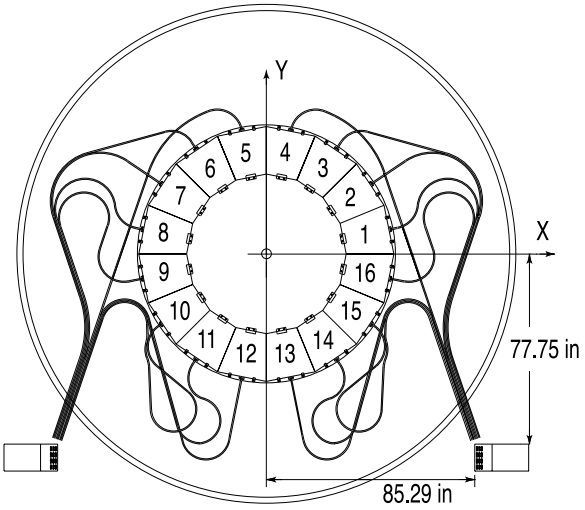

Figure 3.10: The arrangement of the ICD tiles on the endcap cryostats. The rectangles represent the iron block and fiber backplane assemblies in which the ICD electronics and PMTs are installed. The beamline is perpendicular to the page.

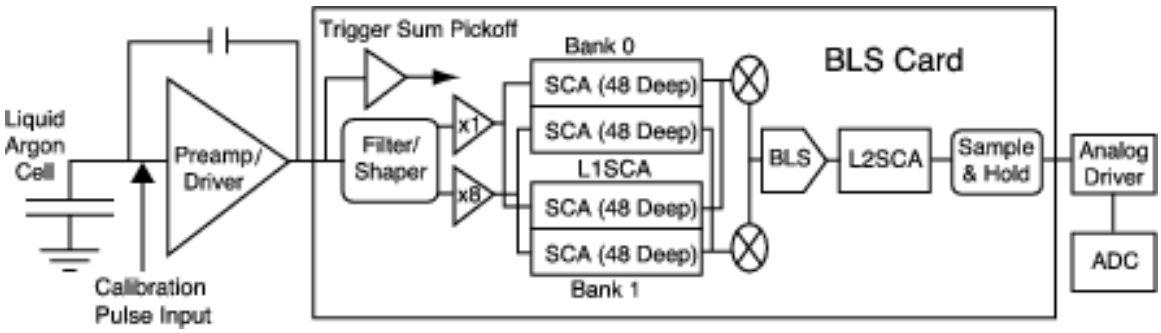

Figure 3.11: Readout chain of the calorimeter in Run II indicating the three major components: preamplifiers, baseline subtractor and storage circuitry (BLS), and the ADCs.

3.7.2 Calorimeter Electronics

Figure 3.11 illustrates the main components in the calorimeter readout chain. There are 55,296 calorimeter electronics channels to be read out; 47,032 correspond to channels connected to physical readout modules in the cryostats. The remaining electronics channels are not connected to the detector (The ADC cards are identical and contain enough channels to read out the most populated regions of the detector). The readout is accomplished in three principal stages. In the first stage, signals from the detector are transported to charge preamplifiers located on the cryostats via low impedance coaxial cable. In the second stage, signals from the preamplifiers are transported on twisted-pair cables to the analog signal shaping and storage circuits on baseline subtractor (BLS) boards. The precision signals from the BLSs are transmitted on an analog bus and driven by analog drivers over 130 m of twisted-pair cable to ADCs. These signals then enter the data acquisition system for the Level 3 trigger decision and storage to tape. The preamplifiers and BLSs are completely new for Run II, and were necessary to accomodate the significant reduction in the Tevatron's bunch spacing.

3.8 Muon System

The central muon system consists of a toroidal magnet, drift chambers, the cosmic cap and bottom scintillation counters, and the $A\phi$ scintillation counters. Exploded views of the muon system are shown in Figures 3.12 and 3.13.

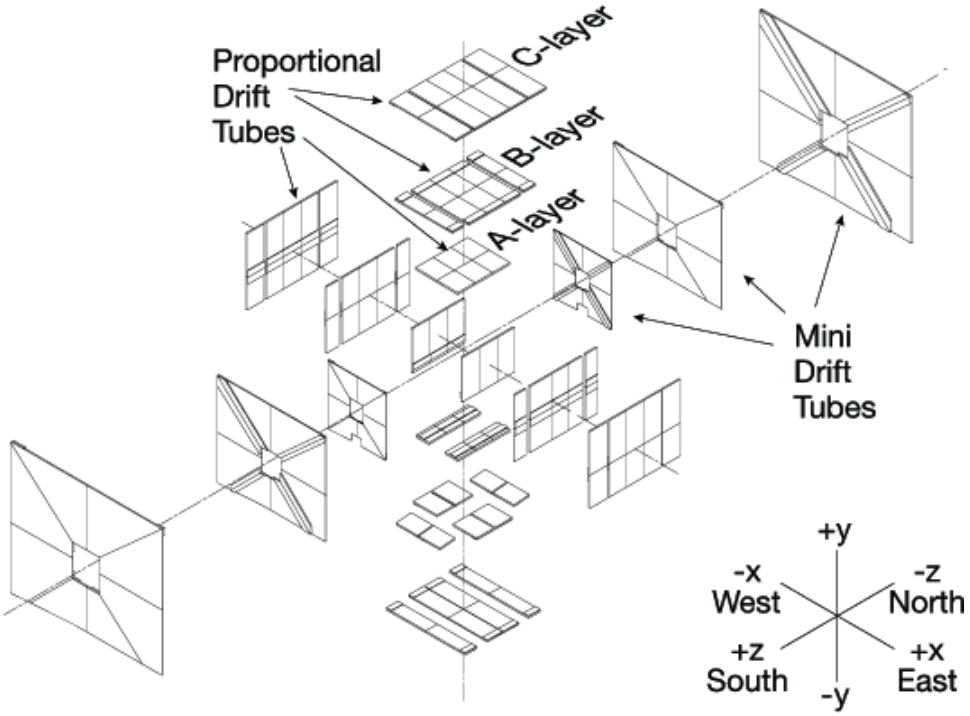

Figure 3.12: Exploded view of the muon wire chambers.

For muon triggering and measurement, the upgraded detector uses the original central muon system proportional drift tubes (PDTs) and toroidal magnets, central scintillation counters (some new and some installed during Run I), and a completely new forward muon system. The central muon system provides coverage for $|\eta| \lesssim 1.0$. The new forward muon system extends muon detection to $|\eta| \approx 2.0$, uses mini drift tubes (MDTs) rather than PDTs, and includes trigger scintillation counters and beam pipe shielding.

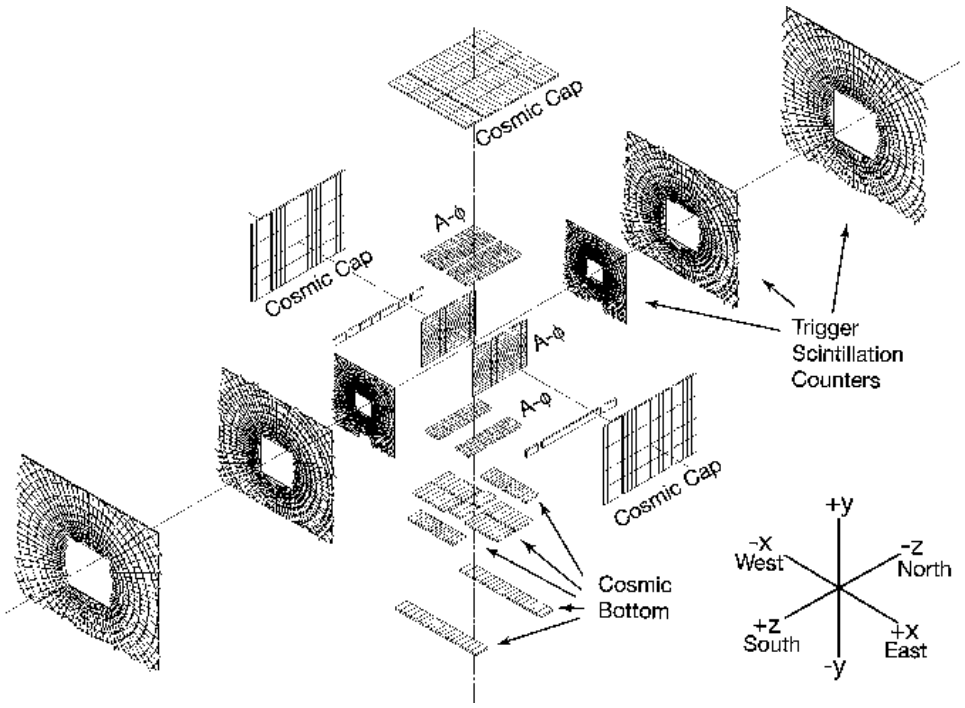

Figure 3.13: Exploded view of the muon scintillation detectors.

During Run I, a set of scintillation counters, the cosmic cap, was installed on the top and upper sides of the outer layer of central muon PDTs. This coverage has been extended to the lower sides and bottom of the detector, to form the cosmic bottom. These trigger scintillation counters are fast enough to allow us to associate a muon in a PDT with the appropriate bunch crossing and to reduce the cosmic ray background. Additional scintillation counters, the $A\phi$ counters, have been installed on the PDTs mounted between the calorimeter and the toroidal magnet. The $A\phi$ counters provide a fast detector for triggering and identifying muons and for rejecting out-of-time background events.

The scintillation counters are used for triggering; the wire chambers are used for precise coordinate measurements as well as for triggering. Both types of detectors contribute to background rejection: the scintillator with

timing information and the wire chambers with track segments.

3.8.1 Toroidal Magnets

The central toroid is a square annulus 109 cm thick whose inner surface is about 318 cm from the Tevatron beamline; it covers the region $|\eta| \lesssim 1$. To allow access to the inner parts of the detector, it was constructed in three sections. The center-bottom section is a 150-cm-wide beam, fixed to the detector platform, which provides a base for the calorimeters and central tracking detectors. Two C-shaped sections, which can be moved perpendicularly to the center beam, complete the central toroid. The magnet is wound using twenty coils of ten turns each. The two end toroids are located at $454 \leq |z| \leq 610$ cm. In the center of each end toroid is a 183 cm square hole centered on the beamline; in x and y the magnets extend 426 cm from the beamline. The end toroid windings are eight coils of eight turns each.

Having a stand-alone muon-system momentum measurement *i*) enables a low-p_T cutoff in the Level 1 muon trigger, *ii*) allows for cleaner matching with central detector tracks, *iii*) rejects π/K decays, and *iv*) improves the momentum resolution for high momentum muons.

3.8.2 Central Muon Drift Chambers

The three layers of drift chambers are located inside (A layer) and outside (B and C layers) of the central toroidal magnet and cover $|\eta| \lesssim 1$. Approximately 55% of the central region is covered by three layers of PDTs; close to 90% is covered by at least two layers. The drift chambers are large, typically 2.8×5.6 m^2, and made of rectangular extruded aluminum tubes. The PDTs outside of the magnet have three decks of drift cells; the A layer has four decks with the exception of the bottom A-layer PDTs which have three decks. The cells are 10.1 cm across; typical chambers are 24 cells wide and contain 72 or 96 cells. Along with an anode wire at the center of each cell, vernier

cathode pads are located above and below the wires to provide information on the hit position along the wire. The wires are ganged together in pairs within a deck and then read out by electronics located at one end of each chamber.

For each PDT hit, the following information is recorded: the electron drift time, the difference ΔT in the arrival time of the signal pulse at the end of the hit cell's wire and at the end of its readout partner's wire, and the charge deposition on the inner and outer vernier pads. Both ΔT and the charge deposition are used to determine the hit position along the wire. The drift distance resolution is $\sigma \approx 1$ mm. The resolution of the ΔT measurement varies depending on whether the muon passes through the cell close to or far from the electronics. If the hit occurs far from the electronics, the resolution is approximately 10 cm. If it is close, the signal propagates two wire lengths and the dispersion in the signal causes the resolution to degrade to about 50 cm. Using charge division, the pad signal resolution is about 5 mm. However, only the A-layer pads are fully instrumented with electronics; about 10% of the B- and C-layer pads are instrumented. There are several reasons for this: *i*) for tracks traversing all three layers, the pad coordinate does not improve the pattern recognition or resolution significantly, *ii*) for tracks that only reach the A-layer, the additional information could help with track matching and background rejection, *iii*) the pad signals are used to monitor the gain to track aging in the PDTs — the instrumented B- and C-layer pads serve this purpose, and *iv*) fully instrumenting the B- and C-layer pads was too expensive.

The cosmic cap and bottom counters are installed on the top, sides and bottom of the outer layer of the central muon PDTs. They provide a fast timing signal to associate a muon in a PDT with the appropriate bunch crossing and discriminate against the cosmic ray background.

The $A\phi$ scintillation counters cover the A-layer PDTs, those between the calorimeter and the toroid. They provide a fast detector for triggering on

and identifying muons and for rejecting out-of-time backscatter from the forward direction. In-time scintillation counter hits are matched with tracks in the CFT in the Level 1 trigger for high-p_T single muon and low-p_T dimuon triggers. The counters also provide the time stamp for low-p_T muons which do not penetrate the toroid and thus do not reach the cosmic cap or bottom counters.

3.8.3 Forward Muon System

The layout of the forward muon system is shown in Figure 3.1. It covers $1.0 \lesssim |\eta| \lesssim 2.0$ and consists of four major parts: the end toroidal magnets, three layers of MDTs for muon track reconstruction, three layers of scintillation counters for triggering on events with muons, and shielding around the beam pipe.

Mini drift tubes were chosen for their short electron drift time (below 132 ns), good coordinate resolution (less than 1 mm), radiation hardness, high segmentation, and low occupancy. The MDTs are arranged in three layers (A, B, and C, with A closest to the interaction region inside the toroidal magnet and C furthest away), each of which is divided into eight octants, as illustrated in Figure 3.12. A layer consists of three (layers B and C) or four (layer A) planes of tubes mounted along magnetic field lines (the field shape in the forward toroids is more "square" than "circular"). The entire MDT system contains 48,640 wires; the maximum tube length is 5830 mm in layer C. Since the flux of particles drops with increasing distance from the beam line, the occupancy of individual tubes is the same within a factor of two over an entire layer.

The momentum resolution of the forward muon spectrometer is limited by multiple scattering in the toroid and the coordinate resolution of the tracking detector. Although the MDT coordinate resolution measured in a test beam is about 350 μm, the 18.8 ns time bin of the digitizing electronics leads to a resolution of about 0.7 mm per hit. The standalone momentum resolu-

tion of the forward muon system is approximately 20% for muon momentum below 40 GeV/c. The overall muon momentum resolution is defined by the central tracking system for muons with momentum up to approximately 100 GeV/c; the forward muon system improves the resolution for higher momentum muons and is particularly important for tracks with $1.6 \lesssim \eta \lesssim 2.0$, i.e. those which do not go through all layers of the CFT.

The muon trigger scintillation counters are mounted inside (layer A) and outside (layers B and C) of the toroidal magnet (Figure 3.1). The C layer of scintillation counters is shown in Figure 3.14. Each layer is divided into octants containing about ninety-six counters. The ϕ segmentation is 4.5° and matches the CFT trigger sectors. The η segmentation is 0.12 (0.07) for the first nine inner (last three) rows of counters. The largest counters, outer counters in the C layer, are 60×110 cm^2. The B and C layers have geometries similar to that of the A layer, but limited in places by the collision hall ceiling and floor. The counter design was optimized to provide good time resolution and amplitude uniformity for background rejection, high muon detection efficiency, and reasonable cost for the production of nearly five thousand counters.

Three sources contribute to non-muon background in the central and forward muon systems: *i*) scattered proton and antiproton fragments that interact with the end of the calorimeter or with the beampipe produce background in the central and forward A layer; *ii*) proton and antiproton fragments interacting with the Tevatron low-beta quadrupole magnets produce hits in the B and C layers of the forward muon system; and *iii*) beam halo interactions from the tunnel. Shielding installed in the accelerator tunnel during Run I significantly reduced the background from beam halo. New shielding has been installed for Run II to reduce the background due to proton and antiproton remnants. Reduction in backgrounds along with the use of radiation-hard detectors helps ensure the long-term, reliable operation of the muon system.

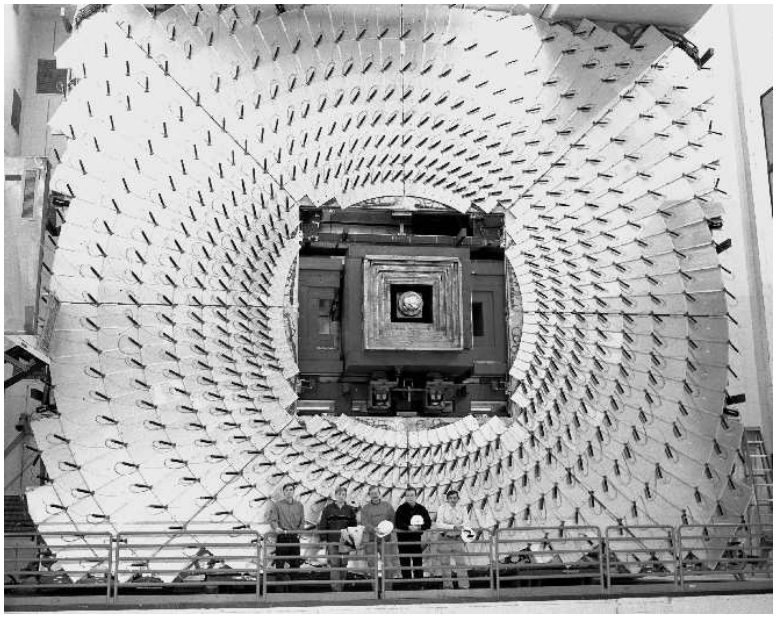

Figure 3.14: Photograph of the C layer of muon trigger scintillation counters of the forward muon system.

The shielding consists of layers of iron, polyethylene, and lead in a steel structure surrounding the beam pipe and low-beta quadrupole magnets. Iron is used as the hadronic and electromagnetic absorber due to its relatively short interaction (16.8 cm) and radiation (1.76 cm) lengths and low cost. Polyethylene is a good absorber of neutrons due to its high hydrogen content. Lead is used to absorb gamma rays. The position of the shielding is shown in Figure 3.1.

3.9 Forward Proton Detector (FPD)

The forward proton detector (FPD) measures protons and antiprotons scattered at small angles (on the order of 1 mrad) that do not impinge upon the main DØ detector. During Run I, such diffractive events were tagged using a rapidity gap (the absence of particles in a region of the detector), however

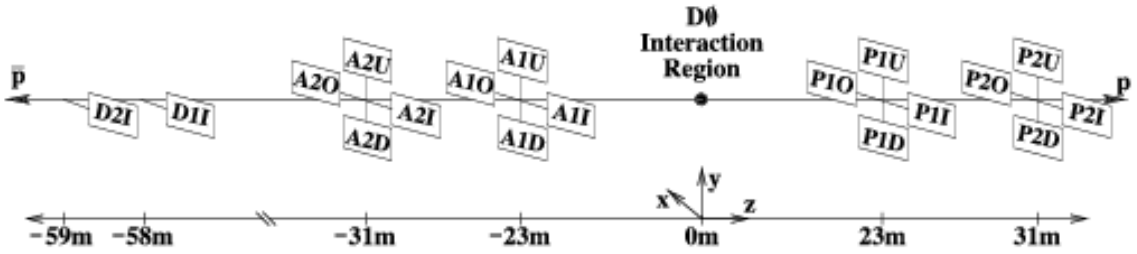

Figure 3.15: FPD layout. Quadrupole castles are designated with a leading P or A when placed on the p side or the $\bar{p}$ side, respectively; the number designates the station location; while the final letter indicates pot potition (U for up, D down, I in, O out). D1I and D2I are dipole castles.

a forward particle detector is necessary for access to the full kinematics of the scattered particle.

The FPD consists of a series of momentum spectrometers that make use of accelerator magnets in conjunction with position detectors along the beam line. The position detectors operate a few millimeters away from the beam and have to be moved out of the beamline during injection of protons or antiprotons into the accelerator. Special stainless steel containers, called Roman pots, house the position detectors, allowing them to function outside of the ultra-high vacuum of the accelerator, but close to the beam. The scattered p or $\bar{p}$ traverses a thin steel window at the entrance and exit of each pot. The pots are remotely controlled and can be moved close to the beam during stable conditions.

The Roman pots are housed in stainless steel chambers called castles. The FPD consists of eighteen Roman pots arranged in six castles. The castles are located at various distances from the DØ interaction point and in locations that do not interfere with the accelerator. The arrangement of the FPD is shown in Figure 3.15.

The FPD acceptance is maximized by minimizing the distance between the detectors and the beam axis. This distance is limited primarily by interaction with the beam halo which increases as the pots are inserted closer to the

beam. FPD acceptance is determined as a function of t, the four-momentum transfer squared of the scattered proton or antiproton, and $\xi = 1 - x_p$ where x_p is the fractional longitudinal momentum of the scattered particle. For the dipole spectrometer, the acceptance is highest for $|t| \lesssim 2$ GeV$^2/c^4$, $0.04 \lesssim \xi \lesssim 0.08$ and extends to $|t| \lesssim 4.3$ GeV$^2/c^4$, $0.018 \lesssim \xi \lesssim 0.085$ (coverage is incomplete). The acceptance in the quadrupole spectrometers covers most of the region $0.6 \lesssim |t| \lesssim 4.5$ GeV$^2/c^4$, $\xi \lesssim 0.1$.

For elastic events, both particles must be detected by diagonally opposite spectrometers with no activity detected in any other DØ subdetector. A sample of elastic events collected during special runs was used to measure the position resolution of the FPD by comparing the x coordinate determined by combining information from the u and v planes to the x coordinate from the x plane. This process gives a resolution of 130 μm.

3.10 Luminosity Monitor

The primary purpose of the luminosity monitor (LM) is to determine the Tevatron luminosity at the DØ interaction region. This is accomplished by detecting inelastic $p\overline{p}$ collisions with a dedicated detector. The LM also serves to measure beam halo rates and to make a fast measurement of the z coordinate of the interaction vertex.

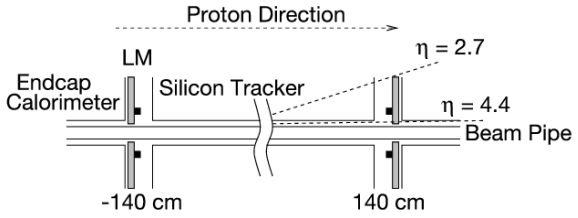

Figure 3.16: Schematic drawing showing the location of the LM detectors.

The LM detector consists of two arrays of twenty-four plastic scintillation counters with PMT readout located at $z = \pm 140$ cm (Figure 3.16). A

schematic drawing of an array is shown in Figure 3.17. The arrays are located in front of the end calorimeters and occupy the radial region between the beam pipe and the forward preshower detector. The counters are 15 cm long and cover the pseudorapidity range $2.7 < |\eta| < 4.4$.

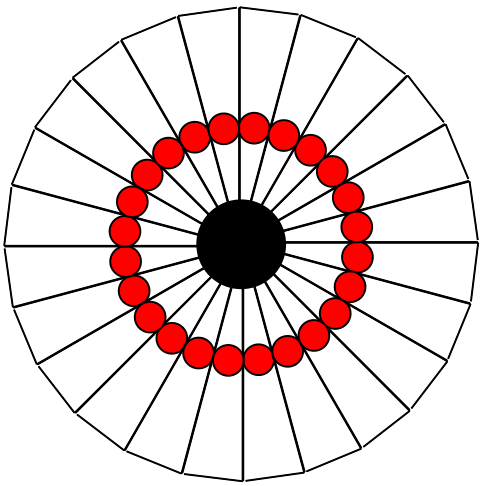

Figure 3.17: Schematic drawing showing the geometry of the LM counters and the locations of the PMTs (solid dots).

Radiation damage is a concern for detectors located this close to the beams. Much of the radiation dose seen by these detectors comes from the $p\overline{p}$ collision products and is thus unavoidable. The PMTs are exposed to a radiation flux of about 25 krad/fb^{-1}, which is sufficient to cause darkening of the borosilicate glass window typically used for PMTs. The R5505Q PMTs have fused silica (quartz) windows which are largely immune to radiation damage. The radiation flux increases rapidly with decreasing radius, reaching a level of approximately 300 krad/fb^{-1} at the innermost scintillator edge. A modest ($\approx 10\%$) light loss was expected for the innermost scintillator edge after 3 fb^{-1}.

The luminosity $\mathcal{L}$ is determined from the average number of inelastic collisions per beam crossing $\bar{N}_{LM}$ measured by the LM: $\mathcal{L} = \frac{f\bar{N}_{LM}}{\sigma_{LM}}$ where f is the beam crossing frequency and σ_{LM} is the effective cross section for

the LM that takes into account the acceptance and efficiency of the LM detector. Since $\bar{N}_{LM}$ is typically greater than one, it is important to account for multiple $p\overline{p}$ collisions in a single beam crossing. This is done by counting the fraction of beam crossings with no collisions and using Poisson statistics to determine $\bar{N}_{LM}$.

To accurately measure the luminosity, it is necessary to distinguish $p\overline{p}$ interactions from the beam halo backgrounds. We separate these processes by making precise time-of-flight measurements of particles traveling at small angles with respect to the beams. We first assume that particles hitting the LM detector originate from a $p\overline{p}$ interaction and estimate the z coordinate of the interaction vertex z_v from the difference in time-of-flight: $z_v = \frac{c}{2}(t_- - t_+)$ where t_+ and t_- are the times-of-flight measured for particles hitting the LM detectors placed at ± 140 cm. Beam-beam collisions are selected by requiring $|z_v| < 100$ cm, which encompasses nearly all $p\overline{p}$ collisions produced by the Tevatron ($\sigma_z \approx 30$ cm). Beam halo particles traveling in the $\pm\hat{z}$ direction will have $z_v \approx \mp 140$ cm, and are eliminated by the $|z_v| < 100$ cm requirement.

3.11 Trigger System

With the increased luminosity and higher interaction rate delivered by the upgraded Tevatron, a significantly enhanced trigger is necessary to select the interesting physics events to be recorded. Three distinct levels form this new trigger system with each succeeding level examining fewer events but in greater detail and with more complexity. The first stage (Level 1 or L1) comprises a collection of hardware trigger elements that provide a trigger accept rate of about 2 kHz. In the second stage (Level 2 or L2), hardware engines and embedded microprocessors associated with specific subdetectors provide information to a global processor to construct a trigger decision based on individual objects as well as object correlations. The L2 system reduces the trigger rate by a factor of about two and has an accept rate of approximately

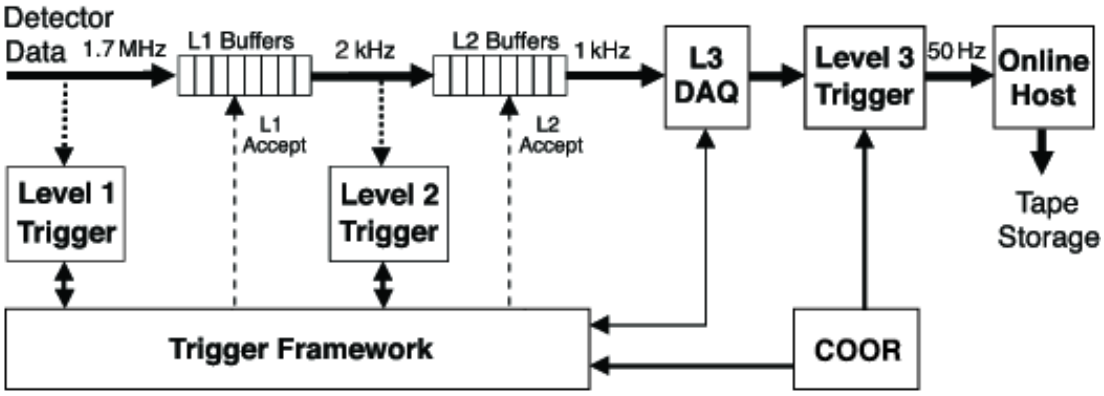

Figure 3.18: Overview of the DØ trigger and data acquisition systems.

1 kHz. Candidates passed by L1 and L2 are sent to a farm of Level 3 (L3) microprocessors; sophisticated algorithms reduce the rate to about 50 Hz and these events are recorded for offline reconstruction. An overview of the DØ trigger and data acquisition system is shown in Figure 3.18. A block diagram of the L1 and L2 trigger systems is shown in Figure 3.19.

The trigger system is closely integrated with the read out of data, as illustrated in Figure 3.18. Each event that satisfies the successive L1 and L2 triggers is fully digitized, and all of the data blocks for the event are transferred to a single commodity processor in the L3 farm. The L1 and L2 buffers play an important role in minimizing the experiment's deadtime by providing FIFO storage to hold event data awaiting a Level 2 decision or awaiting transfer to Level 3.

The overall coordination and control of DØ triggering is handled by the COOR package running on the online host. COOR interacts directly with the trigger framework (for L1 and L2 triggers) and with the DAQ supervising systems (for the L3 triggers).

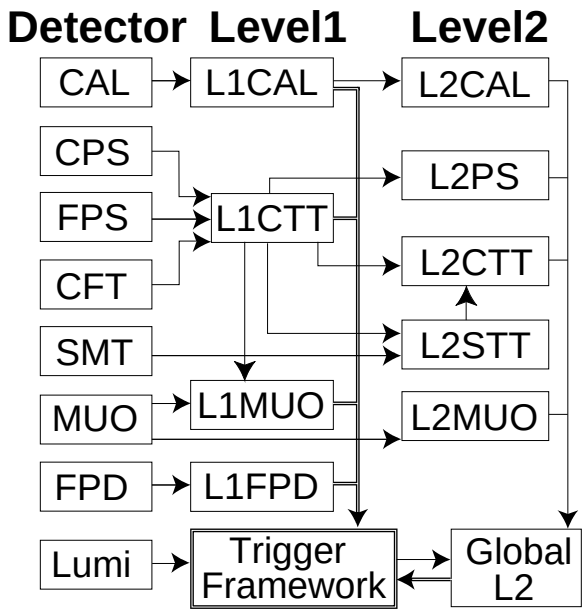

Figure 3.19: Block diagram of the DØ L1 and L2 trigger systems. The arrows show the flow of trigger-related data.

3.12 Data Adquisition System (DAQ)

The data acquisition system (L3DAQ) transports detector component data from the VME readout crates to the processing nodes of the L3 trigger filtering farm. The online host receives event data from the L3 farm nodes for distribution to logging and monitoring tasks. Overall coordination and control of triggering and data acquisition is handled by the COOR program running on the online host system.

The L3DAQ system's designed bandwidth is 250 MB/s, corresponding to an average event size of about 200 kB at an L2 trigger accept rate of 1 kHz. As shown in Figure 3.20, the system is built around a single Cisco 6509 ethernet switch. A schematic diagram of the communication and data flow in the system is shown in Figure 3.21. All nodes in the system are based on commodity computers (SBCs) and run the Linux operating system. TCP/IP sockets implemented via the ACE C++ network and utility library are used

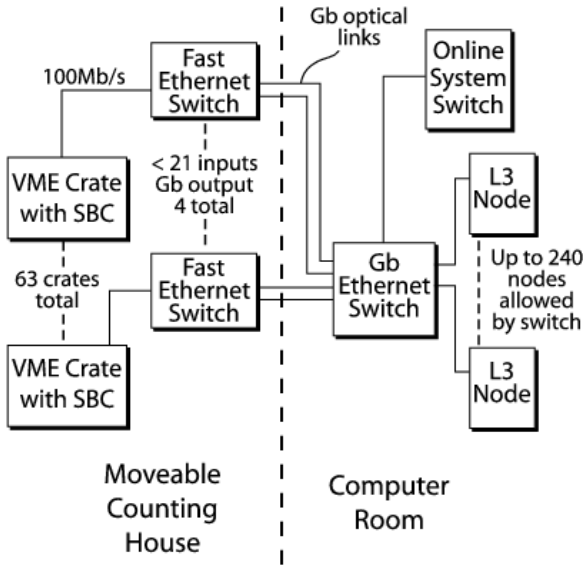

Figure 3.20: The physical network configuration of the L3DAQ system. The moveable counting house holds electronics for the detector and moves with the detector between the assembly hall and the collision hall.

for all communication and data transfers.

Up to sixty-three VME crates are read out for each event, each containing 1–20 kB of data distributed among VME modules. An SBC (single board computer) in each VME crate reads out the VME modules and sends the data to one or more farm nodes specified by routing instructions received from the routing master (RM) process. An event builder (EVB) process on each farm node builds a complete event from the event fragments and makes it available to L3 trigger filter processes.

The supervisor process provides the interface between the main DØ run control program (COOR) and the L3DAQ system. When a new run is configured, the supervisor passes run and general trigger information to the RM and passes the COOR-provided L3 filter configuration to the EVB process on relevant farm nodes, where it is cached and passed on to the L3 filter processes.

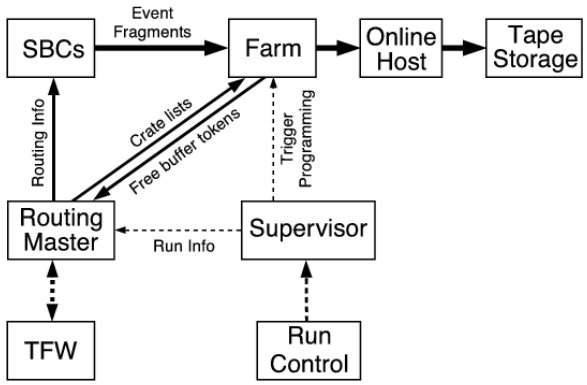

Figure 3.21: Schematic illustration of the information and data flow through the L3DAQ system.

All of the online computing systems are connected to a single high-capacity network switch. The architecture provides for parallel operation of multiple instances of the bandwidth-critical components.

The high-level online software applications are predominately constructed using the Python scripting language. Network communication between the components is implemented with the InterTask Communication (ITC) package, a multi-platform, multi-threaded client/server messaging system developed at Fermilab and based on the ACE network and utility library.

3.13 Monitoring and Control

The DØ experiment has extended EPICS (Experimental Physics and Industrial Control System) to meet the control and monitoring requirements of a large high energy physics detector. EPICS, an integrated set of software building blocks for implementing a distributed control system, has been adapted to satisfy the slow controls needs of the detector by *i*) extending the support for new device types and an additional field bus, *ii*) the addition of a global event reporting system that augments the existing EPICS alarm support, and *iii*) the addition of a centralized database with supporting tools

for defining the configuration of the control system.

EPICS uses a distributed client-server architecture consisting of host-level nodes that run application programs (clients) and input/output controller (IOC) nodes (servers) that interface directly with the detector hardware. The two classes of nodes are connected by a local area network. Clients access process variable (PV) objects on the servers using the EPICS channel access protocol.

To process significant events from all experiment sources, a separate facility, the significant event system (SES), collects and distributes all changes of state. The SES has a central server that collects event messages from sender clients and filters them, via a Boolean expression, for routing to receiving clients. Sender clients, including the IOCs, connect to the server and all state changes on those clients, including alarm transitions, are sent to the server.

One of the most complex tasks performed by the control system is the configuration of the detector for specific run conditions. The set of distinct configurations, both for physics data collection and for calibration runs, is very large; the usual technique of uploading a specific detector configuration and saving it as a file for subsequent downloading is impractical. For ease of configuration management, the detector is represented as a tree with nodes at successively deeper levels corresponding to smaller, more specialized units of the detector. The terminal nodes of the tree, called action nodes, each manage the configuration of a specific, high-level device.

A single server program, COMICS, manages the configuration of the EPICS-accessible part of the detector. The tree nodes, both intermediate and action, are all specialized instances of a base node class that defines the majority of the methods that characterize node behavior. The detector tree structure is defined by a set of configuration files that are Python program segments that instantiate instances of these nodes.

An application framework, in the Python scripting language, assists in

developing operator interfaces and provides a consistent "look and feel" for all visual displays. This framework includes a collection of specialized, graphical objects that construct updating displays of PV values using a Python interface to the EPICS channel access application program interface (APS). The experiment uses more than forty instances of these monitoring displays in the control room to manage the detector components.

While using EPICS records for control and monitoring tasks, almost every detector group needs to maintain structured access to archived PV values. There are two major archiving tools employed by DØ: *i*) the channel archiver, for needs that require sampling rates of 1 Hz or faster, but do not require frequent access to historical data; and *ii*) the EPICS/Oracle Archiver, for long-term studies that require slower sampling rates (once per minute or less frequently), easy access to data at any moment, and minimal maintenance.

Many channel archivers are running concurrently, monitoring several thousand PVs. About once a week, collected archives are sent to the central Fermilab robotic tape storage via the SAM data management system. The channel archiver toolset has interfaces, including web-based tools, that enable retrieval from an archive of data in different formats and generation of time plots with various options.

Chapter 4

Data Selection and Event Reconstruction

Having described the motivation, theoretical background and experimental settings behind this thesis, we arrive at the backbone of our analysis: the data. By data we understand all the $p\bar{p}$ collisions information recorded to disc, which needs to be processed and reduced (skimmed) for further analysis. We will then reconstruct the events that we are interested in, the $B_s^0 \rightarrow D_s^- \mu^+ \nu X$ decay, starting from the right side of figure 1.5 towards the left until have enough confidence we have found our B_s^0. Monte Carlo simulation methods are used in order to compute the efficiency of our findings, as well as to introduce the needed correction factors. In order to get a clean signal the background noise must be understood and described, and it is done so in this chapter as well.

4.1 Data

The data sample used in this report consists of approximately 400 pb^{-1} of $p\bar{p}$ collisions at $\sqrt{s} = 1.96$ TeV collected by the DØ detector at Fermilab during 2002-2004. The data sample was skimmed from the common sample

CSG [4]. Based on the bMU skim, which was produced for B analyzes in semileptonic decays, a loose selection of $D\mu$ candidates was made, trying to avoid any bias on the lifetime. Although no specific requirements at the trigger level were used, it was checked that all final selected events satisfied at least one unbiased (with respect to impact parameter and lifetime) muon trigger, see section .2 for details.

The requirements in this skim were:

- Common Sample filter "SKIM_bMU";
- at least one medium certified muon in the event [5];
  1. nseg > 2,
  2. $p_T > 1.5$ GeV/c,
  3. $p > 3.0$ GeV/c,
  4. N(CFT) > 1,
  5. N(SMT) > 1,
  6. a converged local χ^2 fit (chiqloc > 0),
  7. Number of matched central tracks > 0,
  8. $\chi^2 < 25$ of global muon fit.
- two opposite–charged tracks consistent with a $\phi \rightarrow K^+K^-$ candidate;
  1. $0.99 <$ M $(K^+, K^-) < 1.05$ GeV/c^2,
  2. $p_T > 0.7$ GeV/c for each track,
  3. N(CFT) > 1,
  4. N(SMT) > 1,
- a pion candidate consistent with a $D_s^- \rightarrow \phi\pi^-$ candidate;
  1. $p_T > 0.7$ GeV/c,

2. N(CFT) > 1,

3. N(SMT) > 1,

4. $1.6 <$ M $(\phi\pi^+) < 2.3$ GeV/c^2,

5. $P_{\chi^2}(D_s) > 0.1\%$,

- $2.5 <$ M$(D_s^-, \mu^+) < 5.5$ GeV/c^2;
- $P_{\chi^2}(B_s^0) > 0.01\%$;
- all tracks were clustered into jets using the DURHAM [6, 7] clustering algorithm with p_T cut–off 15 GeV/c, we required all particles to be in the same jet as the muon.
- all tracks are associated with the same primary vertex.

We processed the data using the p14.06 release. Skimmed data was saved in aadst format and stored in SAM [8]. The dataset correspond to approximately 400 pb^{-1}.

4.2 Monte Carlo

Some quantities in this analysis are determined using Monte Carlo (MC) methods. We have generated MC samples using PYTHIA [7] for the production and hadronization phase, and EvtGen [9] for decaying the "b" and "c" hadrons. MCP14 phase has been used in all cases. We generated B_s^0 meson samples with c$\tau = 439$ microns, and no–mixing. The signal sample included contributions from $D_s^-\mu^+\nu$, $D_s^{*-}\mu^+\nu$, $D_{s0}^{*-}\mu+\nu$, $D_{s1}^{'-}\mu^+\nu$, and $D_s^{(*)-}\tau^+\nu$ [1]. To save processing time, D_s^- was forced to decay to $\phi\pi^-$ followed by $\phi \to K^-K^+$.

To be able to evaluate non-combinatorial backgrounds, we generated processes such as $\bar{B}^0 \to D_s^{(*)-}D^{(*)+}$, and $B^- \to D_s^{(*)-}D^{(*)0}X$, where the

[1] $D^{(*)}\bar{D}^{(*)}$ will stands for the sum of $D^*\bar{D}^*$, $D^*\bar{D}$, $\bar{D}D^*$, and $D\bar{D}$. When $D^{(*)}$ appears alone, it will denote either D, D^* or D^{**}.

"right-sign" $D_s^- \mu^+$ combination can be obtained by allowing $D^{(*)+/0}$ to decay semileptonically. The $B_s^0 \to D_s^{(*)-} D_s^{(*)+} X$ and $B_s^0 \to D_s^{(*)-} D^{(*)+/0} X$ processes were also generated. Explicit details of these Monte Carlo samples are given in the appendix Sec. .1.

To be able to fully–simulate these samples, we applied some kinematic cuts prior to DØgstar, (using d0_mess filter): muons had to have $p_T > 1.9$ GeV/c and $|\eta| < 2.1$, the kaons (and pions) from ϕ (D_s) had to have $p_T > 0.6$ GeV/c and $|\eta| < 3.0$, and the p_T of the D_s has to be greater than 1.0 GeV/c. The samples were then processed using the standard full chain procedure DØgstar–DØsim–DØreco. All samples were generated as private production but following the official production criteria. The produced thumbnails were then filtered using the same procedure as in data, described in previous section, above.

4.3 Reconstruction

Events containing semi–muonic B_s^0 decays are identified using a tight selection criteria for the muon present. Reconstruction of B_s^0 candidates is based on the B Analysis package, AATrack [10].

Muon candidates were required to satisfy the criteria described above, plus they had to have a higher reconstructed transverse momentum of $p_T >$ 2 GeV/c. This cut, as well as other higher p_T cuts in the selection, is used to reduce combinatorial background. In other analyses it can be lower but to improve signal significance one has to use impact–parameter cuts or lifetime cuts. Such cuts are avoided in this analysis to reduce any possible bias of the measurement.

Since is difficult to reconstruct the primary vertex on an event–by–event basis, without biasing its determination toward the B_s^0, (due to the tracks coming from the B_s^0 vertex are displaced from the primary vertex) its reconstruction is based on the tracks and the mean beam–spot position. The latter

is calculated for every run, where a typical run lasts several hours. The initial primary vertex is defined by all available tracks, tracks are removed when a track causes a change of more than 9 units in the χ^2 for a fit to a common vertex. The process is repeated until no more tracks can be removed. Tracks from the B_s^0 are not included in the primary vertex determination, for a more detailed description see Ref. [11]. A detailed study of the performace of this vertexing algorithm can be found in Sec. B of DØNote 4690.

To reconstruct $D_s^- \to \phi\pi^-$, any pair of oppositely charged tracks with $p_T > 1.0$ GeV/c are assigned the kaon mass and combined to form a ϕ candidate. Each ϕ candidate is required to have a mass in the range 1.008-1.032 GeV/c^2 compatible with the reconstructed ϕ mass at DØ. The ϕ candidate is then combined with another track of $p_T > 0.7$ GeV/c; for "right-sign" combination we require that the charge of this track be opposite to the charge of the muon. This third track is assigned the pion mass. To have a good vertex determination, all selected tracks must have at least one SMT hit and one CFT hit. The three selected tracks are combined to form a common vertex, the D_s^- vertex. The confidence level of the combined vertex fit is required to be greater that 0.1%, and the p_T of the D_s^- candidate is required to be greater than 3.5 GeV/c.

The secondary vertex, where the B_s^0 decays to a muon and a D_s^- is obtained by simultaneously intersecting the trajectory of the muon track with the flight path of the D_s^- candidate. The confidence level of that vertex should be greater that 0.01%. To further reduce combinatorial background the reconstructed D_s^- decay vertex is required to be positively displacement from the primary vertex as projected along the direction of the D_s^- momentum.

Given the fact that ϕ has spin 1 and D_s^- and ϕ^- are spin 0 particles, the helicity angle (Φ), defined by as the angle between the directions of the K^- and D_s^- in the ϕ rest frame, has a distribution proportional to $\cos^2(\Phi)$. A cut of $|\cos\Phi| > 0.4$ is applied to further remove combinatorial background,

which was found to have a flat distribution in $\cos\Phi$. To suppress physics background, due to $D^{(*)}D^{(*)}$ processes, we required that the transverse momentum of the muon with respect to the D, p_{Trel}, to be greater than 2 GeV/c. The candidate $B_s(D_s\mu)$ invariant mass was also restricted to $3.4-5.0$ GeV/c^2 to further reduce this kind of background and be consistent with a B meson candidate. To increase the significance of the B_s^0 signal we further require that the isolation of the B be greater than 0.65 units, since the number of tracks near the B_s^0 candidate tends to be small. Isolation, $\mathcal{I}(B)$ was defined as $\mathcal{I} = p^{tot}(\mu D_s)/(p^{tot}(\mu D_s) + \sum p_i^{tot})$, where the sum $\sum p_i^{tot}$ was taken over all charged particles in the cone $\sqrt{(\Delta\phi)^2 + (\Delta\eta)^2} < 0.5$, with $\Delta\phi$ and $\Delta\eta$ defined as the pseudo–rapidity and the azimuthal angle with respect to the (μD_s) direction. The muon, kaons, and pion candidates are not included in the sum.

In the cases where we had more than one candidate per event; we choose the one with the best vertex probability $P_{\chi^2}(B_s)$. We also have required the pseudo–proper decay length error to be less than 500 microns.

The invariant mass distribution of the D_s^- candidates is shown in Fig. 4.1(a). Figure 4.1(b) shows the reconstructed invariant mass distribution of the D_s^- candidates after a cut of in the significance of the pseudo-proper decay length to be [2] greater than 5, e.g. $\lambda/\sigma(\lambda) > 5$ for illustration purposes. "Right–sign" and "wrong–sign" combinations are shown in same figure. This cut is not applied for the rest of the analysis. The D_s^- invariant mass distribution for "right-sign" $D_s^-\mu^+$ candidates is fitted using a Gaussian to describe the signal and a second order polynomial to describe the combinatorial background. A second Gaussian is included for the Cabibbo-suppressed $D^- \to \phi\pi^-$ decay. The fit result is overlaid in the same figure. The fit yields a signal of 5176 ± 242 (stat) $\pm$ 314 (sys) events in the D_s^- peak and a mass of 1958.8 ± 0.9 MeV/c^2, slightly shifted from the PDG value of 1968.3 ± 0.5 MeV/c^2 [12],

[2] For definition of the pseudo-proper decay length (PPDL) see Sec. 4.4. The uncertainty in this quantity is obtained on an event-by-event basis from the full covariance matrices of the tracks and the uncertainty in the position of the primary vertex.

the width of the Gaussian is 22.6 ± 1.0 MeV/c^2.

The systematic uncertainty comes from the verification of the D_s^- signal yield, where we have fix the mean and width parameters to the one obtained from the tight cut sample, $\lambda/\sigma(\lambda) > 5$, and from the use of an exponential shape for the background. For the D^- the fit returns 1551 ± 233 events. Fit parameters are shown in Table 4.1. The shifts observed in the D mass peak are due to the current material and magnetic modeling of the experiment. We have found that this does not have any sizeable effect on the lifetime determination.

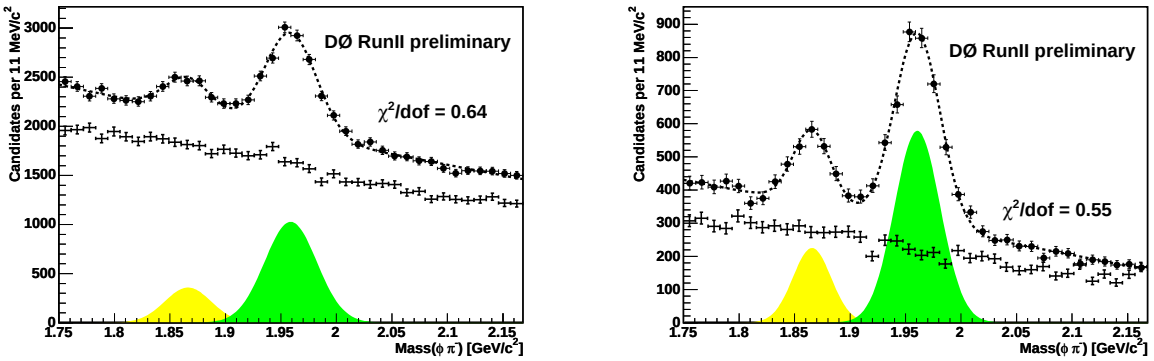

Figure 4.1: (a) Mass distribution for D_s^- candidate events. Points with errors bars show the "right-sign" $D_s^-\mu^+$ combinations, and the crosses show the corresponding "wrong-sign" distributions. The dashed curve represents the result of the fit to the "right-sign" combinations. The mass distribution for the D_s^- signal is shown in green, and the D^- signal in yellow; (b) same distributions after requiring a significance of the pseudo-proper decay length greater than 5.

Parameter	Value	Error	Units
Fraction D_s^- signal	0.0734	0.0034	
Fraction D^- signal	0.0220	0.0033	
$\sigma_{M(D_s^-)}$	22.6	1.0	MeV/c^2
$\sigma_{M(D^-)}$	20.1	2.8	MeV/c^2
Mass D_s^-	1958.8	0.9	MeV/c^2
Mass D^-	1865.7	2.4	MeV/c^2
a_2	-1.75	0.63	(GeV/c^2)$^{-2}$
a_1	3.51	2.48	(GeV/c^2)$^{-1}$

Table 4.1: Result of the invariant D_s^- mass fit to the "right-sign" $D_s^-\mu^+$ combinations. a_1 and a_2 are the coefficients of the polynomial PDF, used for describing the combinatorial background shape. Fractions of D_s^- and D^- are determined from the fit.

4.4 Pseudo-Proper Decay Length and K Factor

The lifetime of the B_s^0, τ, is related with the decay length, L, by the relation

$$L = c\tau\beta\gamma = c\tau\frac{p}{m}, \tag{4.1}$$

where $c\tau$ is the proper decay length, p is the total momentum and m its mass. In the transverse plane this relation is transformed to

$$L_{xy} = c\tau\frac{p_T}{m}, \tag{4.2}$$

where p_T is the transverse momentum of the B_s^0, and L_{xy} is the so-called transverse decay length. The decay length of the B_s^0 in the transverse plane is defined as the displacement of the B_s^0 vertex from the primary vertex [3], projected onto the transverse momentum of the $D_s^-\mu^+$ system. If $\vec{X}$ is a

[3]As described above, the primary vertex is determined using a beam-spot constraint while the secondary vertex, B_s^0, as well as the tertiary vertex, D_s^- is determined by a fit to the candidate tracks.

Common Sample filter SKIM_bMU
all tracks must have at least one SMT and CFT hit
all particles to be in the same jet as the muon
all tracks are associated with the same primary vertex

at least a muon satisfaying:

- nseg = 3
- $p_T > 2.0$ GeV/c
- $p > 3.0$ GeV/c
- A converged local χ^2 fit (chiqloc > 0)
- Number of matched central tracks > 0
- $\chi^2 < 25$ of global muon fit

two opposite charged tracks consistent with a $\phi \rightarrow K^+K^-$ candidate:

- $p_T > 1.0$ GeV/c for each track
- $1.008 <$ M $(K^+, K^-) < 1.032$ GeV/c^2

a pion candidate consistent with a $D_s^- \rightarrow \phi\pi^-$ candidate:

- $p_T(\pi^-) > 0.7$ GeV/c
- $1.6 <$ M $(\phi\pi^+) < 2.3$ GeV/c^2
- $p_T(D_s^-) > 3.5$ GeV/c
- $P_{\chi^2}(D_s^-) > 0.1\%$
- Helicity$(D_s^-) > 0.4$
- $\vec{L}_{xy}(D_s^-) \cdot \vec{p}_T(D_s^-) > 0.0$

$3.4 <$ M$(D_s^-, \mu^+) < 5.0$ GeV/c^2
$P_{\chi^2}(B_s^0) > 0.01\%$
$p_T(\mu^+$ w.r.t. $D) > 2.0$ GeV/c
$\mathcal{I}(B_s^-) > 0.65$
$\sigma(\lambda_B) < 500$ μm
one candidate per event based on best B_s^0 vertex fit

Table 4.2: Summary of all cuts used in this analysis.

vector which points from the primary vertex to the secondary vertex in the transverse plane, we then have

$$L_{xy} = \frac{\vec{X} \cdot \vec{p_T}(D_s^- \mu^+)}{|\vec{p_T}(D_s^- \mu^+)|}. \tag{4.3}$$

Now, when the B_s^0 decays semileptonically, it is not fully reconstructed and thus $p_T(B_s^0)$ is not determined. The p_T of the $D_s^- \mu^+$ system is used as the best approximation, and a correction factor, K, has to be introduced. This K factor is defined by

$$K = \frac{p_T(D_s^- \mu^+)}{p_T(B_s^0)}. \tag{4.4}$$

The quantity used to extract the B_s^0 lifetime is called the pseudo-proper decay length, denoted by λ, and is defined by

$$\lambda = L_{xy} \frac{m(B_s^0)}{p_T(D_s^- \mu^+)} = c\tau \frac{1}{K}. \tag{4.5}$$

The correction factor K is determined using Monte Carlo methods. This correction is applied statistically by smearing the exponential decay distribution when extracting the $c\tau(B_s^0)$ from the pseudo-proper decay length in the lifetime fit.

We used the MC samples described in Sec. 4.2, where B_s^0 has been decayed semileptonically through D_s^-, D_s^{*-}, D_{s0}^{*-}, and $D_{s1}^{'-}$. The D_s^{*-} decays almost entirely to D_s^- and a photon, while D_{s0}^{*-} and $D_{s1}^{'-}$ decay to D_s^- and a π^0. Since the information for B_s^0 branching ratios as well as the information of the D_s^{*-} and D_s^{**-} particles is not well-known, we used the information provided by the EvtGen program and we later varied such information to evaluate any possible systematic uncertainty due to this assumption. Since the D_s^- originating from D_s^{*-} or D_s^{**-} could have softer p_T distribution in comparison with the direct $B_s^0 \to D_s^-$, the K correction factors are determined separately, to allow further studies. The branching fractions used in MC are:

$$Br(B_s^0 \to D_s^- \mu^+ \nu) = (2.10 \pm 0.64)\%$$

$$Br(B_s^0 \to D_s^{*-} \mu^+ \nu) = (5.60 \pm 1.70)\%$$

$$Br(B_s^0 \to D_{s0}^{*-} \mu^+ \nu) = (0.20 \pm 0.06)\%$$

$$Br(B_s^0 \to D_{s1}^{'-} \mu^+ \nu) = (0.37 \pm 0.11)\%$$

$$Br(B_s^0 \to D_s^{(*)-} \tau^+ \nu) \times Br(\tau^+ \to \mu^+ \nu) = 2.86\% \times 17.7\% = (0.51 \pm 0.15)\%$$

The Monte Carlo samples were processed with the same reconstruction and selection criteria applied to data. Figure 4.2 (a) shows the obtained K factor distribution for the main four contributions separately. The combined K distribution is shown in Fig. 4.2(b). Table 4.3 shows the K factor mean and RMS values for the different $D_s^{(*)}$ contributions.

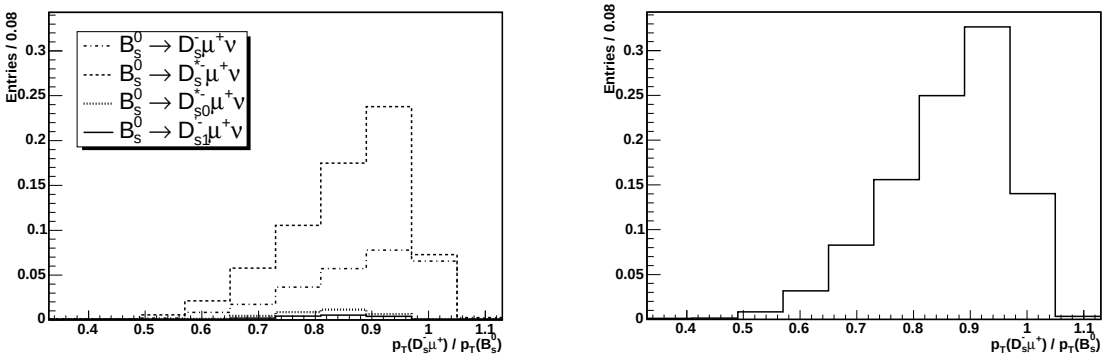

Figure 4.2: Monte Carlo K factor distribution for $B_s^0 \to D_s^- \mu^+ \nu X$. (a) Normalized K factor distributions for each contribution, (b) K factor for all contributions combined.

Contribution	Mean	R.M.S.
$D_s^- \mu^+ X$	0.8823	0.1109
$D_s^{*-} \mu^+ X$	0.8590	0.1021
$D_{s0}^{*-} \mu^+ X$	0.8254	0.0986
$D_{s1}^{'-} \mu^+ X$	0.8147	0.0900
$D_s^{(*)-} \tau^+ X$	0.7703	0.0948
All	0.8628	0.1053

Table 4.3: K factor mean and RMS for different $D_s^{(*)}$ contributions.

4.5 Physics Background

Apart from the background due to combinatorial processes such as a real muon and a fake D_s^-, there could be real physics processes which will produce a real muon and a real D_s^-, where neither comes from the semileptonic decay of B_s^0. These "right-sign" $D_s^- \mu^+$ combinations will be in the signal sample. We define such events as physics backgrounds. There are two possible sources for the physics backgrounds:

1. charm background: prompt c, $c\bar{c}$; and
2. bottom background: b, $b\bar{b}$, not $B_s^0 \to D_s^- \mu^+ X$ decay

To estimate the contribution of such processes we used Monte Carlo methods.

4.5.1 $c\bar{c}$ Background

One of the possible sources of physics backgrounds come from the prompt charm events (c or $c\bar{c}$) In this case real D_s^- are created at the collision point and decay with short lifetime. Tracks that have $p_T > 2$ GeV, muons, are also generated at the primary vertex or from c quark decay. These backgrounds are expected to have almost zero lifetime, and could give relatively large effects to the B_s lifetime measurement. However, it is difficult to know how

much the prompt charm backgrounds exists in data using kinematic quantities, then we will use MC samples. This contamination has been evaluated in the DØ published analysis, "Measurement of the ratio of B^+ and B^0 meson lifetimes" [13]: 10 ± 7 %. The PPDL distribution of events passing the requirement criteria of that analysis is shown in the Fig. 4.3. In same figure the PPDL distribution for events passing the cuts of the current analysis is also shown. As can been see the effect of IP cuts (used in the lifetime ratio analysis) is pretty small. We will use the distribution obtained with our cuts as the shape of charm background. We parametrize it as a Gaussian with parameters shown in the figure. Variations to this estimates are taken to evaluate systematic uncertainties. As an extra cross–check in the fit will let this fraction of $c\bar{c}$ to float, which gives us a fraction of 7 ± 4 %, consistent with the number above. We decide to keep the larger value with its corresponded uncertainty to be conservative.

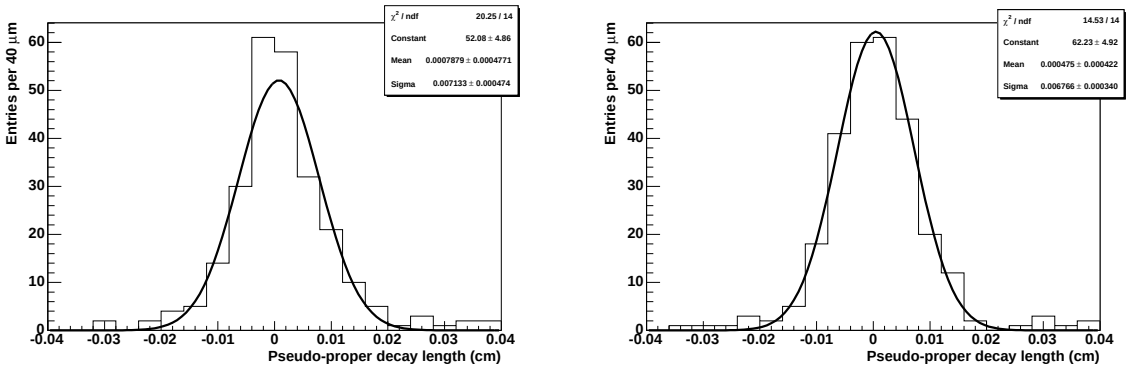

Figure 4.3: PPDL distribution for prompt charm events (ccbar). Left: PPDL distribution for events passing the lifetime ratio analysis cuts. Right: PPDL distribution for events passing cuts of the current analysis.

4.5.2 Non–B_s^0 Background

There are some events which originates from the $\bar{B}$ mesons ($\bar{B}^0$, $B-$, $\bar{B}_s^0$) and provide the $D_s^- \mu^+$ final state, but not through the semileptonic decay ($B_s^0 \to D_s^- \mu^+ \nu X$). We call these events as non–B_s^0 backgrounds. These kind of backgrounds are expected to have relatively long lifetime, thus their effect on the lifetime fit will be relatively smaller than the charm background.

Three sources of such events are identified as: $\bar{B}^0 \to D_s^{(*)-} D^{(*)+} X$, $B^- \to D_s^{(*)-} \bar{D}^{(*)0} X$, and $\bar{B}_s^0 \to D_s^{(*)-} D^{(*)} X$. In the first two processes, the $D^{(*)+}$ or the $\bar{D}^{(*)0}$ decay semileptonically, while in the last contributions the two $D^{(*)}$, which can be a $D^{(*)+}$ or $\bar{D}^{(*)0}$ or even a $D_s^{(*)+}$ can decay semileptonically. These events can be reconstructed as signal events, but the momentum of the lepton (muon) coming from the decay of the $D^{(*)}$ will be softer, since it comes from a secondary decay of a charm hadron, then is expected that such contributions will be also small due to kinematic cuts.

	$\bar{B}^0 \to D_s^- D^{(*)} X$	$B^- \to D_s^- D^{(*)} X$	$B_s^0 \to D_s^+ D_s^{(*)-} X$	$B_s^0 \to D_s^+ D^{(*)} X$
Br.	$(10.5 \pm 2.6)\%$	$(10.5 \pm 2.6)\%$	$(10^{+9}_{-7})\%$	$(15.4 \pm 3.9)\%$
$\langle K \rangle$	0.7607	0.7599	0.8155	0.7623
RMS(K)	0.0918	0.0843	0.1093	0.0885
$f_{D_s D}$	3.7%	3.7%	3.5%	0.4%

Table 4.4: $f_{D_s D}$ contributions and MC information.

The $f_{D_s D}$ contributions are obtained as the ratio of the efficiencies and acceptances for the specific decays:

$$f_{D_s D} = \frac{\epsilon(b\bar{b} \to BX \to D_s^{(*)-} D^{(*)+} X')}{\epsilon(b\bar{b} \to B_s^0 X \to D_s^{(*)-} \mu^+ \nu X')}. \tag{4.6}$$

Since the information about branching ratios of the involved decays is not well known, neither in the PDG or the Monte Carlo used we will use the information coded in the PYTHIA-EvtGen packages, see Sec. .1. At

the end we vary such information according to the PDG branching ratio errors to evaluate any source of systematic uncertainty. Table 4.4 provide the contributions found as well as information most relevant of each MC sample.

Chapter 5

Measurement

The seeked lifetime measurement is performed in this chapter. This is done so by fitting signal and background probability functions for the pseudo-proper decay length distribution.

5.1 Lifetime Fit

To perform the lifetime fit, we define a signal sample using the D_s^- mass distribution in the region from 1913.6 MeV/c^2 to 2004.0 MeV/c^2, corresponding to $\pm 2\sigma$ from fitted mean mass, 1958.8 MeV/c^2. The number of candidates in this region is 21028.

The pseudo-proper decay length distribution of the combinatorial background events contained in the signal sample was defined using "right-sign" events from the D_s^- sidebands (1755.3 – 1800.5 MeV/c^2 and 2117.1 – 2162.3 MeV/c^2) and "wrong-sign" events from the interval 1755.3 – 2162.3 MeV/c^2.

We assume that the combinatorial background is due to random track combinations and then the sideband sample events can be used to model the background in the signal sample. This assumption is supported by the mass distribution of the "wrong-sign" combinations where no enhancement is visible in the D_s^- mass region, see Fig. 4.1. By adding the "wrong-sign"

combinations to the "right-sign" sideband events, we better define the parameters of the combinatorial background events in the D_s^- signal sample.

The pseudo-proper decay length distribution obtained from the signal sample is fit using an unbinned maximum log-likelihood method. Both B_s^0 lifetime and background shape are determined in a simultaneous fit using the signal and background samples. The likelihood function $\mathcal{L}$ is given by

$$\mathcal{L} = \mathcal{C}_{sig} \prod_{i}^{N_S} [f_{sig}\mathcal{F}_{sg}^{i} + (1 - f_{sig})\mathcal{F}_{bg}^{i}] \prod_{j}^{N_B} \mathcal{F}_{bg}^{j}, \tag{5.1}$$

where N_S is the number of events in the signal sample and N_B the number of events in the background sample. f_{sig} is the ratio of D_s^- signal events obtained from the D_s^- mass distributions to the total number of events in the signal sample. To constraint f_{sig} we factor in an additional likehood term using the number of D_s^- signal events, observed from the invariant mass distributions, and its uncertainty, $\mathcal{C}_{sig}$. In practice the fit minimizes the quantity $-2\ln(\mathcal{L})$.

5.1.1 Background Probability Function

The background probability distribution function $\mathcal{F}_{bg}^{j}$ was defined for each measured pseudo-proper decay length λ_j as

$$\begin{aligned}
\mathcal{F}_{bg}^{j}(\lambda_j, \sigma(\lambda_j)) \;=\; & (1 - f_+ - f_{++} - f_- - f_{--}) R(\lambda_j, \sigma(\lambda_j), s) \\
& + \; f_+ \frac{e^{-\lambda_j/\lambda^+}}{\lambda^+} \;+\; f_{++} \frac{e^{-\lambda_j/\lambda^{++}}}{\lambda^{++}} \qquad (\lambda_j \geq 0) \\
& + \; f_- \frac{e^{\lambda_j/\lambda^-}}{\lambda^-} \;+\; f_{--} \frac{e^{\lambda_j/\lambda^{--}}}{\lambda^{--}} \qquad (\lambda_j < 0)
\end{aligned} \tag{5.2}$$

where:

λ_j = the PPDL measurement for each data-point
$\sigma(\lambda_j)$ = the error for the PPDL measurement
f_+ = fraction of events in the positive exponential with short PPDL
f_{++} = fraction of events in the positive exponential with long PPDL
f_- = fraction of events in the negative exponential with short PPDL
f_{--} = fraction of events in the negative exponential with long PPDL
λ^+ = slope of the right exponential short PPDL
λ^{++} = slope of the right exponential long PPDL
λ^- = slope of the left exponential short PPDL
λ^{--} = slope of the left exponential long PPDL
R = PDF for zero lifetime component

The PDF for the zero lifetime component is comprised of a Gaussian resolution function where:

$$R(\lambda_j, \sigma(\lambda_j), s) = \left(\frac{1}{\sqrt{2\pi}\sigma(\lambda_j)s}\right) e^{\frac{-(\lambda_j-\lambda_0)^2}{2(\sigma(\lambda_j)s)^2}} \tag{5.3}$$

is the so called resolution function, and s is the correction factor to the error $\sigma(\lambda_j)$ to account for possible underestimate of the errors in data.

We verified that the background PDF agrees with the "right-sign" sideband events and the "wrong-sign" combinations separately, as can be seen in Fig. 5.1. This allow us to combine both samples resulting in the background sample describe above.

5.1.2 Signal Probability Function

The signal probability distribution function $\mathcal{F}^i_{sig}$ is comprised of a normalized decay exponential function convoluted with a Gaussian resolution function $\mathcal{R}$ and smeared with a normalized K factor distribution function $\mathcal{H}(K)$. This function was defined as:

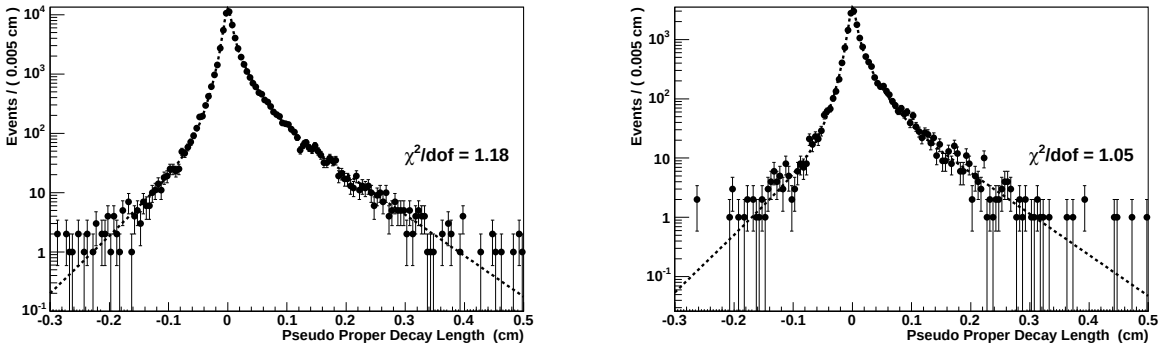

Figure 5.1: Background combinations: Left, "wrong-sign"–only combinations. Right, side-band "right-sign" combinations. The dashed curve corresponds to the fit to both samples combined, projected in each sample separately.

$$\mathcal{F}^j_{sig}(\lambda_j, \sigma(\lambda_j), s) = \int dK\ \mathcal{H}(K)\ \left[\frac{K}{c\tau(B^0_s)} e^{-K\lambda_j/c\tau(B^0_s)} \otimes R(\lambda_j, \sigma(\lambda_j), s)\right], \tag{5.4}$$

where:

$c\tau(B^0_s)$ = is the lifetime for B^0_s signal candidates,

R = is the resolution function, see equation 5.3.

Since a priori, we do not know the the overall scale of the decay length uncertainty, which we estimate on event-by-event basis, the scale factor, s, was introduced as a free parameter in the B^0_s lifetime fit.

In the fit the integration over the K factor PDF is approximated by a finite sum as follows

$$\int dK\ \mathcal{H}(K) \rightarrow \sum_k \Delta K\ \mathcal{H}(K_k), \tag{5.5}$$

where the sum is taken over the bin k of a histogram-med distribution $\mathcal{H}(K_k)$ with bin width ΔK as shown in Fig. 4.2(a).

The events from non-combinatorial background (bottom background) such as the process $B \to D_s^{(*)-} D^{(*)}$ are also taken into account in the likelihood fit terms such as:

$$\int dK\ \mathcal{H}(K)\ \left[f_{D_s D} \frac{K}{c\tau(B)} e^{-K\lambda_j / c\tau(B)} \otimes R(\lambda_j, \sigma(\lambda_j), s) \right], \qquad (5.6)$$

where $f_{D_s D}$ is the fraction of the $D_s^{(*)} D^{(*)}$ process found in the B_s^0 signal sample as described in Sec. 4.5, and $c\tau(B)$ is the lifetime of the corresponding B meson, taken from the world average [12], and scaled by the ratio of masses, Mass(B_s^0)/Mass(B), to account the fact that the mass of the B_s^0 is used in the determination of the pseudo-proper decay length. The K-factor PDF $\mathcal{H}(K)$ for each contribution is evaluated in the same way as in the $D_s^- \mu^+$ signal.

The $c\bar{c}$ background enter in the fit as a Gaussian with fixed parameters, as listed in Fig. 4.3. Then the PDF for the signal events is given by:

$$\mathcal{F}_{sg}^j(\lambda_j, \sigma(\lambda_j), s) = (1 - f_c)[(1 - \sum_i f_{bi}) \mathcal{F}_{sig}^j + \sum_i f_{bi} \mathcal{F}_{bi}^j] + f_c \mathcal{F}_c^j \qquad (5.7)$$

$\mathcal{F}_c^j,\ f_c$ = is the fraction and PDF for ccbar background (a Gaussian distribution)
$\mathcal{F}_{bi}^j,\ f_{bi}$ = is the fraction and PDF for the i–th non–B_s^0 background.

5.2 Fit Results

We performed a simultaneous fit to the signal and background samples, where the parameters for the B_s^0 lifetime ($c\tau(B_s^0)$), background description (λ_-, λ_{--}, λ_+, λ_{++}, f_-, f_{--}, f_+, and f_{++}), and the scale factor parameter, s, where allowed to float. After performing MIGRAD-HESSE-MINOS [14], the fitted values and their statistical uncertainties are shown in Table 5.1. The fitted B_s^0 lifetime is

$$c\tau(B_s^0) = 419.2 \pm 13.1 \ \mu\text{m} \qquad \text{or} \qquad \tau(B_s^0) = 1.398 \pm 0.044 \text{ ps}.$$

Figure 5.2 shows the pseudo-proper decay length distribution of the $D_s^- \mu^+$ signal sample with the fit result superimposed (dashed curve). The dotted curve represents the sum of the background probability function over the events in the signal sample. The B_s^0 signal is represented by the filled green area.

The pseudo-proper decay length distribution for the background sample is displayed in Fig. 5.3 with the result of the fit projected.

Parameter	Value	Stat Uncert.	Units
f_{sig}	0.238	0.007	
f_-	0.109	0.003	
f_{--}	0.022	0.003	
f_+	0.239	0.007	
f_{++}	0.106	0.007	
λ^-	122	5	μm
λ^{--}	461	29	μm
λ^+	209	6	μm
λ^{++}	630	18	μm
s	1.554	0.010	
$c\tau(B_s^0)$	419.2	13.1	μm

Table 5.1: Result of the fit to the $D_s^- \mu^+$ data sample.

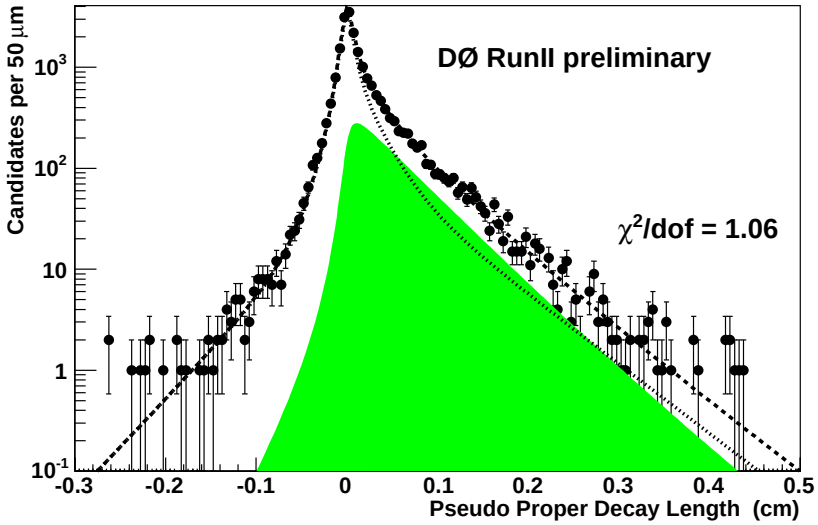

Figure 5.2: Pseudo-proper decay length distribution for $D_s^- \mu^+$ data with the result of the fit superimposed. The dotted curve represents the combinatorial background and the filled green area represents the B_s^0 signal.

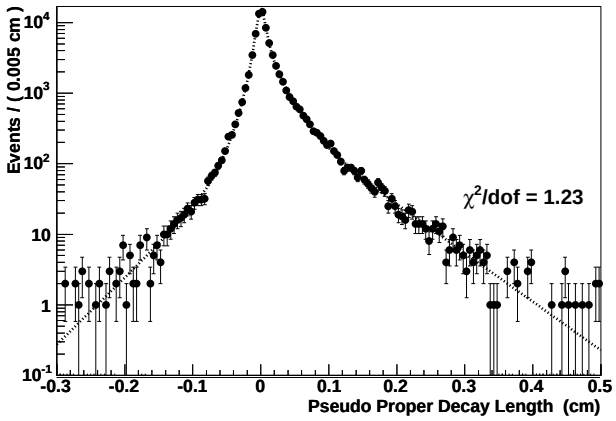

Figure 5.3: Pseudo-proper decay length distribution for background sample, the projection of the fit result is shown by the dashed curve.

Chapter 6

Consistency Checks and Systematic Uncertainties

Once we have our measurement, we need to make sure that measurement is consistent and independent of several factors related to the way in which it was determined. Consistency checks, also known as cross checks, are mainly data sample splitting, in which the whole dataset is divided in two parts using certain parameters and then the measurement is carried away for each subset. Systematic uncertainties on the other hand, change the way the data is selected and fitted, like changing the cut values and fitting techniques. All of these are described in this chapter.

6.1 Consistency checks

6.1.1 Test of Fitting Procedure

To estimate the error due to the fitting procedure we generate 500 Toy MC Samples with the same distributions used on the fit of the pseudo-proper decay length distribution and parameters equal to those obtained from the fit to data. Each sample has been generated with the same number of events

as in data samples. Each Toy MC sample is fitted and the measured lifetime is recorded. The distribution of the fitted lifetimes is fitted with a Gaussian, and a mean of 419.2 ± 0.5 μm is obtained, is consistent with the input value of 419.2 μm. The width of the Gaussian was found to be 12.9 ± 0.4 μm consistent with the statistical uncertainty found in data. Figure 6.1(a) shows the distribution of the fitted lifetimes with the result of the Gaussian fit performed. Figure 6.1(b) shows the pull distribution of the fitted lifetime, which is consistent with unity.

This test demonstrate that the fitting procedure works well and does not introduce any systematic bias in the measurement of the lifetime.

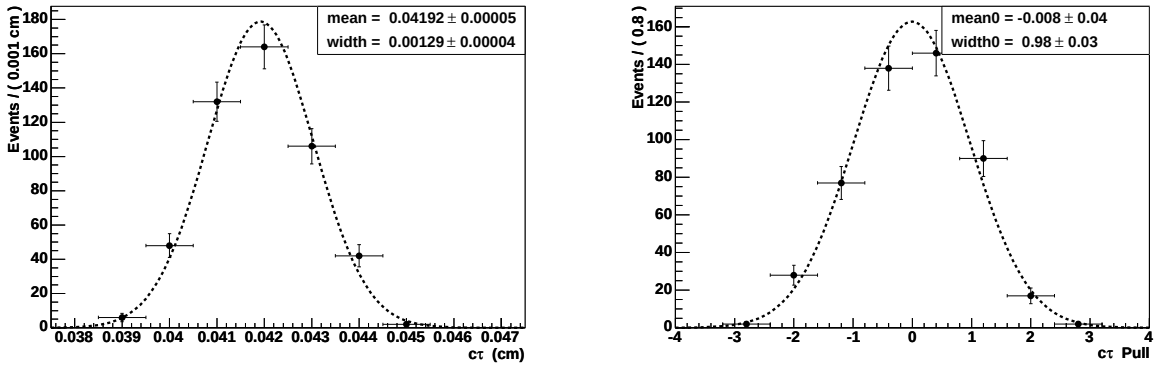

Figure 6.1: (a) Distributions of the fitted $c\tau$ values from the toy MC samples with input lifetime of 419.2 μm. (b) Pull distribution of fitted lifetimes.

We have performed several other test using Toy MC, as shown in [15]. So far, no systematic effect due to the fitting technique is found, and also has been shown that no matter the shape of the background the fit is able to extract the B_s^0 lifetime, as parametrized here.

6.1.2 Test of the Mass Dependence

Given the fact that all mass peaks at DØ are slightly shifted due to remaining magnetic field and material uncertainties, these could produce a small impact on our measurement, the pseudo-proper decay length depends directly on the mass but typical corrections are smaller than 1%. We have checked if this will change our measurement. For the "standard" pseudo–proper decay length calculation we use the PDG mass value of B_s^0. We have re–calculated the pseudo–proper decay length for all events with the mass scaled by the same difference observed in D_s^- mass fit, i.e. by $(M_{fit}(D_s^-) - M_{pdg}(D_s^-))/M_{pdg}(B_s^0) + 1 = (1.9598 - 1.9683)/5.3696 + 1$, and repeat the lifetime fit. We found a shift of -0.8 microns, and will consider this difference negligible.

We also tried to check any possible variation of the background inside the signal D_s^- mass window. Due to our mass resolution we are using a slightly wide mass bin, then we divide our mass signal region in two equal parts and performed the B_s^0 lifetime fit in each sample. We found a consistent result as shown in the last two rows of Table 6.1.

6.1.3 Split Sample Tests

To test the stability of the measurement, we have performed some consistency checks based on sample splitting procedure. In most cases we tried to divide the data in two roughly equal parts. No systematic uncertainty will be quoted from these tests since observed differences were statistically consistent with zero. Table 6.1 shows the fitted lifetimes for different test performed, all of them are consistent.

6.1.4 Lifetime of B^0

To provide support to the method used to extract the B_s^0 lifetime, we have performed the lifetime measurement of the $B^0 \to D^- \mu^+ \nu X$ decay. In Fig. 4.1

Test	$c\tau$ (μm)
run $<$ 181000	417 $\pm$ 18
run $>$ 181000	423 $\pm$ 19
B_s^0	422 $\pm$ 19
$\bar{B}_s^0$	419 $\pm$ 19
$\|\eta(\mu)\| < 0.8$	422 $\pm$ 18
$\|\eta(\mu)\| > 0.8$	417 $\pm$ 19
low mass half of signal region	419 $\pm$ 19
high mass half of signal region	421 $\pm$ 17

Table 6.1: Result of the fit for different split sample tests.

one can easily identified the Cabibbo suppressed decay $D^- \to \phi\pi^-$. The sample composition was estimated in the same way as describe above for D_s, using Monte Carlo events (we generated the needed MC sample in the same way as was made for B_s^0 analysis). It was found that 89.1% of the D^- are from $B^0 \to D^-\mu^+X$, 9.3% from $B^+ \to D^-\mu^+X$, 0.9% from $B^0 \to D^-DX$ and 0.5% from $B_s^0 \to D^-\mu^+X$. Other contributions were found to be really small. Apart from that 10% was assigned as ccbar background in the same way as in the B_s^0 lifetime analysis.

The signal region was defined by the interval 1825.5 – 1905.9 MeV/c^2. All K factor were calculated and the fit performed with the proper correction of definitions in the background samples as well. It was found that the B^0 lifetime obtained is 462 ± 28 μm (stat). Consistent with the world average [12] value for B^0 lifetime (460 μm). Figure 6.2 shows the pseudo-proper decay length distribution of the B candidate sample with the fit result superimposed (dashed curve). The dotted curve represents the the background candidates. The $D^- \to \phi\pi^-$ signal is represented by the filled yellow area.

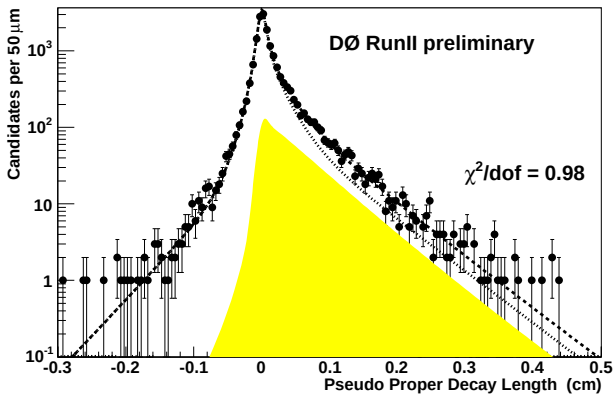

Figure 6.2: Pseudo-proper decay length distribution for $D^-\mu^+$ data with the result of the fit superimposed. The dotted curve represents the combinatorial background and the filled yellow area represents the D^-X candidates.

6.2 Systematic Uncertainties

The systematic uncertainty on the measurement of the B_s^0 lifetime is determined by evaluating the influence of several effects on the fitted lifetime. Contributions are evaluated individually and then added in quadrature to obtain the final systematic uncertainty.

6.2.1 Alignment of the Detector

To estimate the uncertainty due to the alignment of the detector one has to test the lifetime measurement under the assumption of a different SMT geometry. This method has been used in the full-reconstructed decay $B_s^0 \rightarrow J/\psi\phi$ [16] where shifts of ± 2 μm have been observed. We have repeat the study using Monte Carlo signal and found the same shift. We will quote this value as systematic uncertainty.

6.2.2 Combinatorial Background Evaluation

To test the possible inconsistency of the combinatorial background due to the PPDL shape differences between the background combination used for modeling the background and the actual shape of the background under the D_s^- peak, we have tested other assumptions on the background samples: we have used just the events in the sidebands, just the events in the wrong sign combinations, and removing either the right sideband or the left sideband samples. We also have used the same background sample definition in [2]. After performing the fit with these background sample definitions we observed at the most a difference of $\pm 4.3 \mu$m. This will be assigned as the systematic uncertainty.

6.2.3 Cut Selection Bias

When trying to get the most significant signal, one could possibly bias the measurement of $c\tau(B_s^0)$. There are two requirements in our selection method that could potentially change the final result by altering the shape of the pseudo-proper decay length distribution, they are $L_{xy}(D_s^{PV}) > 0.0$ and $p_T(\mu)$ w.r.t. $D_s^- >$ 2.0 GeV/c.

To study their effect, we used Monte Carlo samples. The lifetimes are fitted after all selection criteria is applied. Each cut is then removed individually, the fit is repeated, and the shift is recorded. To take into account all effects introduced by K convolution or measuring method, the differences are taken respect to the input value given to the MC.

Removing only the $L_{xy}(D_s^{PV}) > 0.0$ requirement causes a shift of -0.3 μm. Removing only the $p_T(\mu)$ w.r.t. $D_s^- >$ 2.0 GeV/c requirement results in a shift of +3.0 μm. But, removing both biasing cuts, just results in a shift of +0.7 μm. Using the largest of the individual variations, a systematic uncertainty of $^{+3.0}_{-0.3}$ μm is assigned for the possible selection bias.

Figure 6.3, shows the efficiency plot as function of time, when the biasing

cuts are removed, no significant dependence is observed.

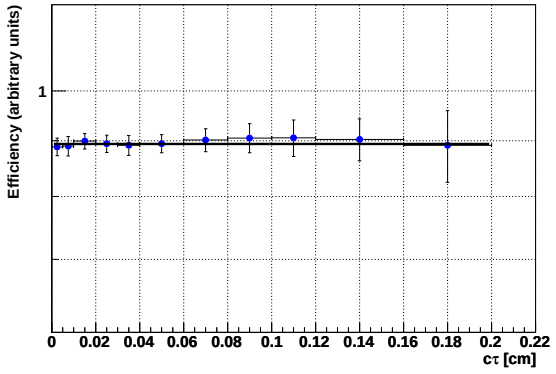

Figure 6.3: Efficiency distribution as function of time with biasing cuts removed, no significant effects are observed.

6.2.4 Decay Length Resolution

To study the effect of uncertainties on the determination of pseudo-proper decay length, the global scale factor parameter, s, has been varied. This parameter was introduced in the fit to account for an overall under– or over–estimation of the event–by–event uncertainty on the pseudo-proper decay length.

In Ref. [16] it was found that the overall scale factor was approximately 1.14, while in the MC studies we have found 1.05. We have forced s to be equal to those value and repeat the fit. We also have used twice these values (e.g. 2.28 and 2.10). We observed a shift of ± 3.7 μm, at the most. We quote these differences as systematic uncertainty due to the resolution model.

Note that the actual value of "s" is not neccesary as large as it looks, since one has to take into account the K factor (about 0.8). If one do that the fit returns 1.240 ± 0.008 consistent with other determinations of this

quatity in fully reconstructed decays. Therefore the variation taken here is very conservative.

6.2.5 K Factor Determination

When extracting the lifetime from a partial reconstructed decay, such as the semileptonic of B_s^0 used in the current analysis, one has to use a correction factor, K, to take into account those missing objects in the reconstruction. That distribution is obtained from Monte Carlo samples.

The shape of the K distribution can be modified due to changes in the kinematics of the event. Such changes could be due to the decay model, the p_T spectrum of the μ, the p_T spectrum of b quark, and the signal sample composition i.e. the ratio $Br(B_s^0 \to D_s^- X)/Br(B_s^0 \to D_s^{*-} X)$. To access all these uncertainties we have generated different MC samples. To account for differences in the $p_T(\mu)$ spectrum, we have changed the p_T cut from 2 GeV/c to 6 GeV/c in the selection applied to MC, a new K factor was obtained and the B_s^0 lifetime repeated, we observe a difference of 2.2 μm. Differences due to modifications of the $p_T(b)$ spectrum are obtained using a new MC sample where the $\hat{p_T}$ of the partons have been changed, e.g. the CKIN(3) PYTHIA parameter was changed from 0.0 to 5.0 GeV/c, this will produce b quarks with harder p_T spectrum (by about the mass of the b quark), a new K distribution was obtained and the fit repeated. We observe -1.4 μm shift. In the standard fit a K factor was obtained from B_s^0 products generated using ISGW decay model, we generated a MC sample using a plain phase-space decay model and repeat the measurement, 2.4 μm shift was obtained due to a difference in the decay model. Finally to take in to account the signal sample composition, we modified the fit to accommodate a sum of two exponential decay distributions instead of one, each with the same decay parameter (lifetime of the B_s^0) but a different K distribution, one obtained for $B_s^0 \to D_s^- X$ and another for $B_s^0 \to D_s^{*-} X$. The two exponential decays are weighted by the corresponding fraction $f_w = Br(B_s^0 \to D_s^- X)/[Br(B_s^0 \to D_s^- X) + Br(B_s^0 \to D_s^{*-} X)]$ or

$Br(B_s^0 \to D_s^{*-}X)/[Br(B_s^0 \to D_s^-X) + Br(B_s^0 \to D_s^{*-}X)] = 1 - f_w$. Then this weight, $f_w = 0.268$, is varied for up-to $\pm 50\%$ of its value and the lifetime fit repeated, a ± 1.6 μm shift was observed.

B_s^0 lifetime fit has also been repeated using different binning in the K factor distribution. So, far no sizable effect on the measurement has been observed.

Adding all these contributions together in quadrature a systematic uncertainty of $^{+3.6}_{-2.1}$ μm is assigned due to the K factor determination.

6.2.6 Physics Background

Background terms not coming from combinatorial enter in the fit as fixed fractions. Since the pseudo-proper decay length of these events is different from B_s^0 semileptonic decays, a mis-measurement of these background fractions will change the final lifetime result. Two kind of these backgrounds were taken into account in the lifetime fit, non-B_s background and $c\bar{c}$ background.

Non–B_s background

To test the effect of the background fractions on the measured B_s^0 lifetime, the values of these fractions are modified following the Br uncertainties, according to the PDG [12], i.e. the fractions for $D_s^{(*-)}D^{(*)0}$, $D_s^{(*-)}D^{(*)+}$, $D_s^{(*-)}D^{(*)}$ and components are changed by $\pm 25\%$, while the fractions for $D_s^{(*-)}D_s^{(*)+}$ are changed by $^{+100}_{-50}\%$. These variations are applied separately and the lifetime fit is repeated for each case and recorded. Furthermore, since the lifetime of B mesons enter in the fit as fixed values, we also have varied them by $\pm 1\sigma$ following the uncertainties quoted in the PDG [12]. Table 6.2 shows all the shifts in the lifetime observed. We also tested the possibility of having different scale factors for the different components, since all D have different lifetime. Using Monte Carlo samples, we have all scale factors consistent with the unity but the one for B_d, which was found to be twice

as big. We changed the fit to include this effect and found a difference of -2.0 μm. We will add this to the total systematic uncertainty due to non–B_s background. Then, a systematic uncertainty of $^{+2.9}_{-4.2}$ μm is assigned due to this source.

Variation			$\Delta c\tau$ (μm)
$f_{D_sD^0}$	$\pm$	25%	± 2.0
$f_{D_sD^+}$	$\pm$	25%	± 1.4
f_{D_sD}	$\pm$	25%	± 0.3
$f_{D_sD_s}$	$^{-}_{+}$	$^{50}_{100}$%	$^{+1.1}_{-2.4}$
$c\tau(D_sD^0)$	$\pm$	1σ	± 0.4
$c\tau(D_sD^+)$	$\pm$	1σ	± 0.3
$c\tau(D_sD)$	$\pm$	1σ	± 0.1
$c\tau(D_sD_s)$	$\pm$	1σ	± 0.8
Total			$^{+2.9}_{-3.7}$

Table 6.2: Result of the fit for variations on the non–combinatorial background parametrization.

$c\bar{c}$ Background

To measure the effect of mis–estimation of this background we have modified the shape and amount of the $c\bar{c}$ background estimate. Taking variations on the width of the Gaussian by $\pm 1\sigma$ as well as the amount of background we found shifts on the B_s lifetime of at the most $^{+2.3}_{-0.8}$ μm. Smaller deviations are observed when the fraction of $c\bar{c}$ is allowed to float.

6.2.7 Summary

In Table 6.3, we summarize and then add in quadrature all the studied systematic uncertainties.

Source	$\Delta c\tau$ (μm)
Detector alignment	± 2.0
Combinatorial background	± 4.3
Selection criteria	$^{+3.0}_{-0.3}$
K factor determination	$^{+3.6}_{-2.1}$
Decay length resolution	± 3.7
non–B_s^0 background	$^{+2.9}_{-4.2}$
ccbar background	$^{+2.3}_{-0.8}$
Total	$\mathbf{^{+8.4}_{-7.6}}$

Table 6.3: Summary of systematic uncertainties for the pseudo-proper decay length.

Chapter 7

Conclusions and Final Thoughts

7.1 B_s^0 Lifetime

Using an integrated luminosity of ≈ 400 pb^{-1}, we have measured the B_s^0 lifetime in the decay channel $D_s^- \mu^+ \nu X$ under the assumption of a single–exponential decay.

$$c\tau(B_s^0) = 419.2 \pm 13.1 \text{ (stat)}^{+8.4}_{-7.6} \text{ (sys) } \mu\text{m}, \tag{7.1}$$

$$\tau(B_s^0) = 1.398 \pm 0.044\text{(stat)}^{+0.028}_{-0.025} \text{ (sys) ps}. \tag{7.2}$$

These results are in good agreement with the current world average values: $\tau(B_s)_{HFAG} = 1.442 \pm 0.066$ ps [17]. Table 7.1 shows the most recent semi–leptonic measurements.

7.2 Conclusions

In conclusion, the B_s^0 lifetime measurement presented here is not only consistent with the previous measurements, but it is currently the world's best

Experiment	dataset	$\tau(B_s^0)$ (ps)
World Average(PDG) [12]		1.461 ± 0.057
ALEPH	91-95	$1.54^{+0.14}_{-0.13} \pm 0.04$
CDF	92-96	$1.36 \pm 0.09^{+0.06}_{-0.05}$
DELPHI	91-95	$1.42^{+0.14}_{-0.13} \pm 0.03$
OPAL	90-95	$1.50^{+0.16}_{-0.15} \pm 0.04$
Average of $D_s l$ measurements [17]		1.442 ± 0.066
CDF [18]	02-04	$1.381 \pm 0.055^{+0.052}_{-0.046}$
This Measurement	**02-04**	$\mathbf{1.398 \pm 0.044^{+0.028}_{-0.025}}$

Table 7.1: Previous semi–leptonic (i.e., flavor-specific) lifetime measurements.

of its kind, even most precise than the global world's average measurement $\tau(B_s)_{PDG} = 1.461 \pm 0.057$ ps [12], where semi–leptonic and hadronic decays were combined. Note that this measurement takes $\Delta\Gamma_s$ equal to zero. The extraction of the average lifetime $\bar{\tau}_s$ for $\Delta\Gamma_s \neq 0$ could be available following the procedures described by the Heavy Flavor Averaging Group (HFAG) [17].

Taking into account the PDG's reported world average liftime measurement of the B^0 as $\tau(B_s)_{PDG} = 1.532 \pm 0.009$ ps [12], our measurement is approximately 2.5σ away from it, more than the 1% predicted by HQE as indicated in section 2.3. However, this result is not conclusive to discard HQE's predictions since we estimate this difference could be further reduced within that 1% margin with a new measurement that uses more statistics. Currently this is work in progress which will include data collected up and until 2009.

7.3 Final Thoughts

The precise measurement obtained in this thesis has been used,at least, in another DØ collaboration article entitled "Combined DØ measurements constraining the CP-violatinig phase and width difference in the B_s^0 system" [22].

In it, the collaboration combines the DØ measurement of the width difference between the light and heavy B_s^0 mass eigenstates and of the CP-violating mixing phase determined from the time-dependent angular distributions in the $B_s^0 \rightarrow J/\psi\phi$ decays along with the charge asymmetry in semileptonic decays also meatured with the DØ detector. Our particular B_s^0 lifetime measurement is used when the article applies the new and improved world-average value as an effective mean lifetime, in the process constraining the values for both $\Delta\Gamma_s$ and $|\phi_s|$. Figure 7.1 shows the resulting constraints, serving as graphical proof of the usefulness of the measurement performed in this thesis.

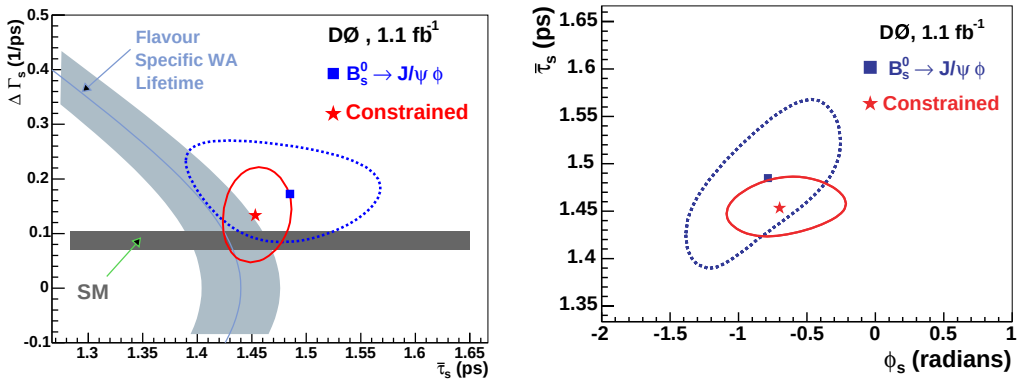

Figure 7.1: (a) Error ellipse in the plane $\Delta\Gamma_s$ versus $\bar{\tau}_s$ for the fit to the $B_s^0 \rightarrow J/\psi\phi$ data (dashed blue line) and for the fit with the constraint from the two D0 measurements of the charge asymmetry in semileptonic B_s^0 decay, and from the world-average flavor-specific liftime (solid red line); (b) Error ellipse in the plane $(\bar{\tau}_s, \phi_s)$ for the solution with $\phi_s < 0$, $\cos\delta_1 > 0$, and $\cos\delta_2 < 0$ of the fit to the $B_s^0 \rightarrow J/\psi\phi$ data (dashed blue line) and of the fit with both the constraint from the two d0 measurements of the charge asymmetry in semileptonic B_s^0 decay, and from the world-average favor-specific lifetime (solid red line). [22]

As a final comment, a further study could be simultaneously fitting both D^- and D_s^- as shown in figure 7.2 in yellow and green respectively. Such work would be interesting and result in lifetime measurements for both particles,

but it was beyond the scope of this thesis since our objective was to get the most precise measurement possible, and a simultaneous fit technique would certainly introduce larger errors.

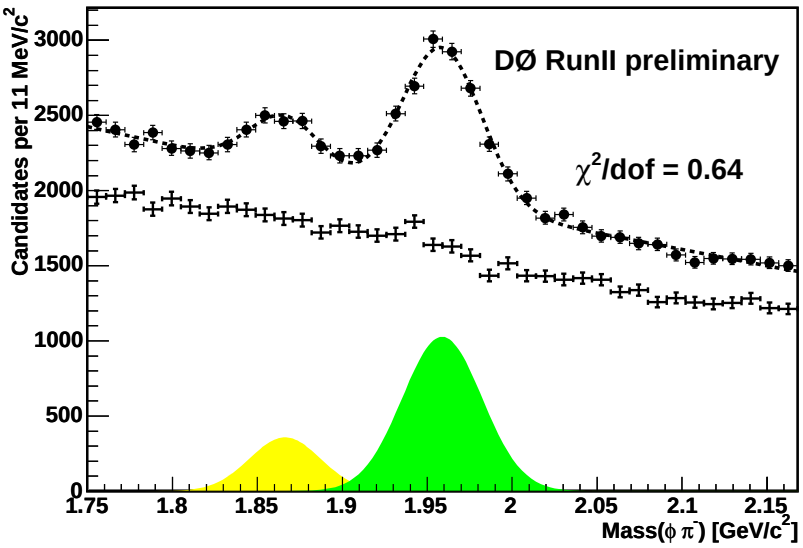

Figure 7.2: The mass distribution for the D_s^- signal is shown in green, and the D^- signal in yellow, a simultaneous fit could also be used to measure both lifetimes.

Bibliography

[1] L. Wolfenstein, preprint No. NSF-ITP-90-29 (unpublished); Phys. Rev. D **43** (1991) 151.

[2] "Measurement of the B_s^0 lifetime using the semileptonic decay channel $B_s^0 \to D_s^- \mu^+ \nu X$", A. Sánchez-Hernández, DØNote 4690 (physics note). "A high statistics measurement of the B_s^0 lifetime", DØ Collaboration, DØ Conf 4729.

[3] M. Neubert, "B Decays and the Heavy–Quark Expansion", in Second Edition of Heavy Flavours, World Scientific, Singapore 1997, hep-ph/9702375.

[4] www-d0.fnal.gov/Run2Physics/cs/skimming/pass1.html, "Pass–1 Skimmed Data".

[5] www-d0.fnal.gov/phys_id/muon_id/d0_private/certif/p14, "P14 Muo-Candidate". For definition of quantities look at DØNote 4091, where p13 muon thumbnail is described, but no change in the storing was made for p14.

[6] "New Clustering Algorithm for Multi-jet Cross Sections in e^+e^- Annihilation", S. Catani, Yu. L. Dokshitzer, M. Olsson, G. Turnock, B.R. Webber, Phys. Lett. **B269**, 432, (1991).

[7] "Pythia 6.2 Physics and Manual", T. Sjöstrand, P. Edén, C. Friberg, L. Lönnblad, G. Miu, S. Mrenna, and E. Norrbim, Comp. Phys. Commun. **135**, 238, (2001).

[8] The 19.9M of events can be accessed using the dataset definition "aadst–bsdmu0–all".

[9] D. J. Lange, Nucl. Instrum. Meth. **A462**, 152, (2001); for details of the decay models in the package, please see www.slac.stanford.edu/∼lange/EvtGen.

[10] "B Analysis Package", d0server1.fnal.gov/users/nomerot/Run2A/B_ANA.html, AATrack version v02-11-05 was used.

[11] "*b*–tagging in DELPHI at LEP", DELPHI Collaboration, *Eur. Phys. J.* **C32**, 185 (2004).

[12] "Review of Particles Physics", S. Eidelman *et al.* (Particle Data Group), Phys. Lett. **B592**, 1 (2004).

[13] "Measurement of the ratio of B^+ and B^0 meson lifetimes", DØ Collaboration, Phys. Rev. Lett. **94**, 182001, (2005).

[14] "MINUIT: Minimization package", F. James, CERN Program Library Long Writeup D506, Version 94.1.

[15] Status reports on this analysis has been shown at the B–physics meeting as well as in the B_s mixing and lifetime meeting. See agenda of the dates: July 28 2005, September 08 2005 and September 15 2005.

[16] "Measurement of the B_s^0 Lifetime in the Exclusive Decay Channel $B_s^0 \to J/\psi\phi$", DØ Collaboration, Phys. Rev. Lett. **94**, 042001, (2005).

[17] "Averages of b-hadron Properties as of Summer 2004", J. Alexander *et al.* (Heavy Flavor Averaging Group), hep–ex/0412073.

[18] "Measurement of the B_s^0 Meson Lifetime Using Semileptonic Decays with Single Lepton Datasets in CDF Run II", CDF Collaboration, CDF Note 7757, 2005.

[19] "Measurement of the Lifetime Difference in the B_s^0 System", DØ Collaboration, Phys. Rev. Lett. **95** (2005) 171801.

[20] "Measurement of the Lifetime Difference Between B_s Mass Eigenstates", CDF Collaboration, Phys. Rev. Lett. **94** (2005) 101803.

[21] "In pursuit of new physics with B_s decays", I. Dunietz, R. Fleischer, and U. Nierste, Phys. Rev. **D63**, 114015, (2001).

[22] "Combined D0 measurements constraining the CP-violatinig phase and width difference in the B_s^0 system", DØ Collaboration, Phys. Rev. D **76** (2007) 057101.

[23] en.wikipedia.org/wiki/Standard_model, "Standard Model"

[24] en.wikipedia.org/wiki/Fermilab, "fermilab"

[25] "B Physics at the Tevatron: Run II and Beyond", FERMILAB-Pub-01/197, hep-ph/0201071. December 2001.

[26] "The Upgraded DØ Detector", DØ Collaboration. FERMILAB-Pub-05-341-E.

Appendices

.1 EvtGen Decay Files Used in the Analysis

.1.1 User Decay File for $B_s^0 \to D_s^- \mu + \nu X$ decay signal

```
noMixing
Alias myphi    phi
Alias myD_s-   D_s-
Alias myD_s*-  D_s*-
Alias myD_s0*- D_s0*-
Alias myD'_s1- D'_s1-
Decay B_s0
0.0210   myD_s-    mu+     nu_mu   PHOTOS  ISGW2;
0.0560   myD_s*-   mu+     nu_mu   PHOTOS  HQET 0.92 1.18 0.72;
0.0020   myD_s0*-  mu+     nu_mu   PHOTOS  ISGW2;
0.0037   myD'_s1-  mu+     nu_mu   PHOTOS  ISGW2;
# tau+ will be decay by TAUOLA, Br(tau+ -> mu+) = 17.7%
0.0080   myD_s-    tau+    nu_tau          ISGW2;
0.0160   myD_s*-   tau+    nu_tau          ISGW2;
0.0018   myD_s0*-  tau+    nu_tau          ISGW2;
0.0028   myD'_s1-  tau+    nu_tau          ISGW2;
Enddecay
Decay myD'_s1-
1.0000  myD_s*- pi0                        VVS_PWAVE  1.0 0.0 0.0 0.0 0.0 0.0;
Enddecay
Decay myD_s0*-
1.0000  myD_s-  pi0                        PHSP;
Enddecay
Decay myD_s*-
0.942   myD_s-  gamma                      VSP_PWAVE;
0.058   myD_s-  pi0                        VSS;
Enddecay
Decay myD_s-
1.0000   myphi  pi-                        SVS;
```

```
Enddecay
Decay myphi
1.0000   K+     K-                          VSS;
Enddecay
End
```

.1.2 User Decay File for $\bar{B}^0 \to D_s^{(*)-} D^{(*)+}$ background sample

```
noMixing
Alias myD_s*- D_s*-
Alias myD_s-  D_s-
Alias myD+    D+
Alias myD*+   D*+
Alias myD_1+  D_1+
Alias myD0    D0
Alias myD*0   D*0
Alias myphi   phi
Decay anti-B0
0.0096   myD+    myD_s-                 PHSP;
0.0102   myD*+   myD_s-                 SVS;
0.0120   myD_1+  myD_s-                 SVS;
0.0094   myD_s*- myD+                   SVS;
0.0200   myD_s*- myD*+                  SVV_HELAMP 0.48 0.0 0.734 0.0 0.48 0.0;
0.0030   myD_s-  myD+  pi0              PHSP;
0.0060   myD_s-  myD0  pi+              PHSP;
0.0030   myD_s*- myD+  pi0              PHSP;
0.0060   myD_s*- myD0  pi+              PHSP;
0.0050   myD_s-  myD+  pi+  pi-         PHSP;
0.0037   myD_s-  myD+  pi0  pi0         PHSP;
0.0037   myD_s-  myD0  pi+  pi0         PHSP;
0.0050   myD_s*- myD+  pi+  pi-         PHSP;
```

```
0.0037   myD_s*- myD+  pi0  pi0          PHSP;
0.0037   myD_s*- myD0  pi+  pi0          PHSP;
Enddecay
Decay myD_1+
0.3333   myD*+   pi0                     VVS_PWAVE  0.0 0.0 0.0 0.0 1.0 0.0;
0.6667   myD*0   pi+                     VVS_PWAVE  0.0 0.0 0.0 0.0 1.0 0.0;
Enddecay
Decay myD*+
0.6830   myD0    pi+                     VSS;
0.3060   myD+    pi0                     VSS;
0.0110   myD+    gamma                   VSP_PWAVE;
Enddecay
Decay myD*0
0.6190   myD0    pi0                     VSS;
0.3810   myD0    gamma                   VSP_PWAVE;
Enddecay
Decay myD_s*-
0.942    myD_s-  gamma                   VSP_PWAVE;
0.058    myD_s-  pi0                     VSS;
Enddecay
Decay myD+
0.0430   anti-K*0   mu+   nu_mu          PHOTOS  ISGW2;
0.0700   anti-K0    mu+   nu_mu          PHOTOS  ISGW2;
0.0036   anti-K_10  mu+   nu_mu          PHOTOS  ISGW2;
0.0038   anti-K_2*0 mu+   nu_mu          PHOTOS  ISGW2;
0.0064   pi0        mu+   nu_mu          PHOTOS  ISGW2;
0.0028   eta        mu+   nu_mu          PHOTOS  ISGW2;
0.0011   eta'       mu+   nu_mu          PHOTOS  ISGW2;
0.0027   rho0       mu+   nu_mu          PHOTOS  ISGW2;
0.0029   omega      mu+   nu_mu          PHOTOS  ISGW2;
0.0027   K-  pi+    mu+   nu_mu          PHOTOS  PHSP;
0.0008   mu+        nu_mu                PHOTOS  SLN;
```

```
Enddecay
Decay myD0
0.0198   K*-   mu+ nu_mu          PHOTOS  ISGW2;
0.0322   K-    mu+ nu_mu          PHOTOS  ISGW2;
0.0014   K_1-  mu+ nu_mu          PHOTOS  ISGW2;
0.0015   K_2*- mu+ nu_mu          PHOTOS  ISGW2;
0.0037   pi-   mu+ nu_mu          PHOTOS  ISGW2;
0.0029   rho-  mu+ nu_mu          PHOTOS  ISGW2;
Enddecay
Decay myD_s-
1.0000   myphi    pi-                SVS;
Enddecay
Decay myphi
1.0000   K+       K-                 VSS;
Enddecay
End
```

.1.3 User Decay File for $B^- \to D_s^{(*)-} D^{(*)0}$ background sample

```
noMixing
Alias myD_s*- D_s*-
Alias myD_s-  D_s-
Alias myD+    D+
Alias myD*+   D*+
Alias myD_10  D_10
Alias myD0    D0
Alias myD*0   D*0
Alias myphi   phi
Decay B-
0.0096   myD0    myD_s-                PHSP;
0.0102   myD*0   myD_s-                SVS;
```

```
0.0120   myD_10  myD_s-                 SVS;
0.0094   myD_s*- myD0                   SVS;
0.0270   myD_s*- myD*0                  SVV_HELAMP 0.48 0.0 0.734 0.0 0.48 0.0;
0.0060   myD_s-  myD+  pi-              PHSP;
0.0030   myD_s-  myD0  pi0              PHSP;
0.0060   myD_s*- myD+  pi-              PHSP;
0.0030   myD_s*- myD0  pi0              PHSP;
0.0055   myD_s-  myD+  pi-  pi0         PHSP;
0.0055   myD_s-  myD0  pi-  pi+         PHSP;
0.0014   myD_s-  myD0  pi0  pi0         PHSP;
0.0055   myD_s*- myD+  pi-  pi0         PHSP;
0.0055   myD_s*- myD0  pi-  pi+         PHSP;
0.0014   myD_s*- myD0  pi0  pi0         PHSP;
Enddecay
Decay myD_10
0.3333   myD*0 pi0                     VVS_PWAVE  0.0 0.0 0.0 0.0 1.0 0.0;
0.6667   myD*+ pi-                     VVS_PWAVE  0.0 0.0 0.0 0.0 1.0 0.0;
Enddecay
Decay myD*+
0.6830   myD0    pi+                   VSS;
0.3060   myD+    pi0                   VSS;
0.0110   myD+    gamma                 VSP_PWAVE;
Enddecay
Decay myD*0
0.6190   myD0    pi0                   VSS;
0.3810   myD0    gamma                 VSP_PWAVE;
Enddecay
Decay myD_s*-
0.942    myD_s-  gamma                 VSP_PWAVE;
0.058    myD_s-  pi0                   VSS;
Enddecay
Decay myD+
```

```
0.0430   anti-K*0   mu+   nu_mu         PHOTOS  ISGW2;
0.0700   anti-K0    mu+   nu_mu         PHOTOS  ISGW2;
0.0036   anti-K_10  mu+   nu_mu         PHOTOS  ISGW2;
0.0038   anti-K_2*0 mu+   nu_mu         PHOTOS  ISGW2;
0.0064   pi0        mu+   nu_mu         PHOTOS  ISGW2;
0.0028   eta        mu+   nu_mu         PHOTOS  ISGW2;
0.0011   eta'       mu+   nu_mu         PHOTOS  ISGW2;
0.0027   rho0       mu+   nu_mu         PHOTOS  ISGW2;
0.0029   omega      mu+   nu_mu         PHOTOS  ISGW2;
0.0027   K-  pi+    mu+   nu_mu         PHOTOS  PHSP;
0.0008   mu+        nu_mu               PHOTOS  SLN;
Enddecay
Decay myD0
0.0198   K*-   mu+ nu_mu          PHOTOS  ISGW2;
0.0322   K-    mu+ nu_mu          PHOTOS  ISGW2;
0.0014   K_1-  mu+ nu_mu          PHOTOS  ISGW2;
0.0015   K_2*- mu+ nu_mu          PHOTOS  ISGW2;
0.0037   pi-   mu+ nu_mu          PHOTOS  ISGW2;
0.0029   rho-  mu+ nu_mu          PHOTOS  ISGW2;
Enddecay
Decay myD_s-
1.0000   myphi    pi-                SVS;
Enddecay
Decay myphi
1.0000   K+       K-                 VSS;
Enddecay
End
```

.1.4 User Decay File for $B_s{}^0 \to D_s^{(*)-} D_s^{(*)+}$ background sample

```
noMixing
```

```
Alias myD_s*- D_s*-
Alias myD_s-  D_s-
Alias myD_s+  D_s+
Alias myD_s*+ D_s*+
Alias myphi   phi
Decay B_s0
0.0086   myD_s-      myD_s+      PHSP;
0.0090   myD_s*+     myD_s-      SVS;
0.0099   myD_s*-     myD_s+      SVS;
0.0197   myD_s*-     myD_s*+     SVV_HELAMP  1.0 0.0 1.0 0.0 1.0 0.0;
Enddecay
Decay myD_s*+
0.942   myD_s+  gamma                  VSP_PWAVE;
0.058   myD_s+  pi0                    VSS;
Enddecay
Decay myD_s*-
0.942    myD_s-  gamma                 VSP_PWAVE;
0.058    myD_s-  pi0                   VSS;
Enddecay
Decay myD_s+
0.0200    phi       mu+    nu_mu     PHOTOS  ISGW2;
0.0260    eta       mu+    nu_mu     PHOTOS  ISGW2;
0.0089    eta'      mu+    nu_mu     PHOTOS  ISGW2;
0.0027    anti-K0   mu+    nu_mu     PHOTOS  ISGW2;
0.0010    anti-K*0  mu+    nu_mu     PHOTOS  ISGW2;
0.0046    mu+       nu_mu           PHOTOS  SLN;
Enddecay
Decay myD_s-
1.0000   myphi    pi-                SVS;
Enddecay
Decay myphi
1.0000   K+       K-                 VSS;
```

```
Enddecay
End
```

.1.5 User Decay File for $B_s{}^0 \to D_s^{(*)-} D^{(*)}$ background sample

```
noMixing
Alias myD_s*- D_s*-
Alias myD_s-  D_s-
Alias myD+    D+
Alias myD*+   D*+
Alias myD0    D0
Alias myphi   phi
Decay anti-B_s0
0.0096   myD_s-   myD+     K0       PHSP;
0.0096   myD_s*-  myD+     K0       PHSP;
0.0096   myD_s*-  myD0     K+       PHSP;
0.0024   myD_s-   myD+     pi0  K0  PHSP;
0.0048   myD_s-   myD0     pi+  K0  PHSP;
0.0048   myD_s-   myD+     pi-  K+  PHSP;
0.0024   myD_s-   myD0     pi0  K+  PHSP;
0.0024   myD_s*-  myD+     pi0  K0  PHSP;
0.0048   myD_s*-  myD0     pi+  K0  PHSP;
0.0048   myD_s*-  myD+     pi-  K+  PHSP;
0.0024   myD_s*-  myD0     pi0  K+  PHSP;
0.0017   myD_s-   myD+              PHSP;
0.0017   myD*+    myD_s-            SVS;
0.0017   myD_s*-  myD+              SVS;
0.0017   myD_s*-  myD*+             SVV_HELAMP  1.0 0.0 1.0 0.0 1.0 0.0;
Enddecay
Decay myD*+
0.6830   myD0    pi+                          VSS;
```

```
0.3060   myD+    pi0                          VSS;
0.0110   myD+    gamma                        VSP_PWAVE;
Enddecay
Decay myD_s*-
0.942    myD_s-  gamma                        VSP_PWAVE;
0.058    myD_s-  pi0                          VSS;
Enddecay
Decay myD+
0.0430   anti-K*0   mu+   nu_mu         PHOTOS  ISGW2;
0.0700   anti-K0    mu+   nu_mu         PHOTOS  ISGW2;
0.0036   anti-K_10  mu+   nu_mu         PHOTOS  ISGW2;
0.0038   anti-K_2*0 mu+   nu_mu         PHOTOS  ISGW2;
0.0064   pi0        mu+   nu_mu         PHOTOS  ISGW2;
0.0028   eta        mu+   nu_mu         PHOTOS  ISGW2;
0.0011   eta'       mu+   nu_mu         PHOTOS  ISGW2;
0.0027   rho0       mu+   nu_mu         PHOTOS  ISGW2;
0.0029   omega      mu+   nu_mu         PHOTOS  ISGW2;
0.0027   K-  pi+    mu+   nu_mu         PHOTOS  PHSP;
0.0008   mu+        nu_mu               PHOTOS  SLN;
Enddecay
Decay myD0
0.0198   K*-   mu+ nu_mu          PHOTOS  ISGW2;
0.0322   K-    mu+ nu_mu          PHOTOS  ISGW2;
0.0014   K_1-  mu+ nu_mu          PHOTOS  ISGW2;
0.0015   K_2*- mu+ nu_mu          PHOTOS  ISGW2;
0.0037   pi-   mu+ nu_mu          PHOTOS  ISGW2;
0.0029   rho-  mu+ nu_mu          PHOTOS  ISGW2;
Enddecay
Decay myD_s-
1.0000   myphi    pi-                SVS;
Enddecay
Decay myphi
```

```
1.0000   K+       K-                  VSS;
Enddecay
End
```

.2 List of the most significant triggers for this analysis

	Trigger Name	%
1	MU_2TRK3_L2M0	22.5
2	MUW_L2M0_2TK3_MM	22.3
3	MUW_W_L2M3_TRK10	19.7
4	MT3_L2M0_2TK3_MM	14.9
5	MT3_L2M0_MM5	14.8
6	MU_JT20_L2M0	12.5
7	MU_JT25_L2M0	10.6
8	MUW_W_L2M0_2TRK3	9.7
9	MU_JT20_MET10	8.8
10	MU_W_L2M3_TRK10	8.2
11	MU_A_L2M3_TRK10	7.6
12	MWTXT10_TK10	7.5
13	2MU_A_L2M0	6.4
14	MUZ_A_L2M3_TRK10	6.2
15	2MU_C_2L2_2TRK	5.8
16	MU_TAU10_L2M0	5.5
17	MU_EM_L2M5	5.2
18	MUW_A_L2M3_TRK10	4.9
19	2MU_A_L2ETAPHI	4.6
20	MU_W_L2M0_2TRK3	4.4
21	MT10W_L2M5_TRK10	4.4
22	MUW_L2M0_MM4	4.4

23	MU_JT15_L2M0	4.3
24	MUZ_W_L2M3_TRK10	4.1
25	MUW_W_L2M0_TRK4	3.9
26	MT3_L2M0_MM4	3.5
27	MU_EM_L2M0	3.4
28	MU_TAU10_2T_L2M0	3.3
29	MUW_L2M0_Tk4_MM	3.2
30	3CJT5_JT20_L2M0	3.2

.3 Lifetime fit for non–zero $\Delta\Gamma/\Gamma$ values

Using the $B_s^0 \to J/\psi\phi$ decay channel, DØ [19] and CDF [20] have measured a non–zero value for $\Delta\Gamma/\Gamma$, which enforce the hypothesis of different width for each $B^0_{s,\mathrm{heavy}}$ and $B^0_{s,\mathrm{light}}$ eigenstates of the $B_s^0\bar{B}_s^0$ system.

In the current analysis, using a single exponential decay, it has been assumed $\Delta\Gamma/\Gamma = 0$. The lifetime fit can be modified to propertly take into account the different width (lifetime) of the two B_s^0 eigenstates. The modified decay time distribution for the signal is given by

$$F(t) = e^{-\Gamma_L t} + e^{-\Gamma_H t} \qquad \text{with} \qquad \Gamma_{L/H} = \Gamma \pm \Delta\Gamma/2$$

where $\Gamma_{H/L}$ are the width of the Heavy and Light eigenstate with Γ the average width and $\Delta\Gamma$ the width difference of those eigenstates. In ref. [15] we showed the difficulties which raise when a fit of this kind is introduced. Here, we quote the values obtained when $\Delta\Gamma/\Gamma$ is fixed and $1/\Gamma$ is allowed to float. The table below summarizes these numbers, along with the likelihood difference respect to the $\Delta\Gamma/\Gamma = 0$ value.

$\lvert\Delta\Gamma/\Gamma\rvert$	c/Γ (μm)	$\Delta(\mathcal{L})$
0.00	419.2 ± 13.1	0.00
0.05	418.6 ± 13.1	-0.05
0.10	416.9 ± 13.1	-0.21
0.15	413.9 ± 13.0	-0.46
0.20	409.8 ± 12.9	-0.79
0.25	404.6 ± 12.7	-1.16
0.30	398.3 ± 12.5	-1.56
0.35	391.0 ± 12.3	-1.96
0.40	382.6 ± 12.0	-2.35
0.50	363.3 ± 11.5	-3.06

Table 2: Average lifetime values for different $\Delta\Gamma/\Gamma$ hypotheses.

.4 Published paper: PRL 97, 241801 (2006)

The Physical Review Letter that was published with the results of this Thesis has been appended in the following and final pages.

Measurement of the B_s^0 Lifetime Using Semileptonic Decays

V. M. Abazov,[36] B. Abbott,[76] M. Abolins,[66] B. S. Acharya,[29] M. Adams,[52] T. Adams,[50] M. Agelou,[18] J.-L. Agram,[19] S. H. Ahn,[31] M. Ahsan,[60] G. D. Alexeev,[36] G. Alkhazov,[40] A. Alton,[65] G. Alverson,[64] G. A. Alves,[2] M. Anastasoaie,[35] T. Andeen,[54] S. Anderson,[46] B. Andrieu,[17] M. S. Anzelc,[54] Y. Arnoud,[14] M. Arov,[53] A. Askew,[50] B. Åsman,[41] A. C. S. Assis Jesus,[3] O. Atramentov,[58] C. Autermann,[21] C. Avila,[8] C. Ay,[24] F. Badaud,[13] A. Baden,[62] L. Bagby,[53] B. Baldin,[51] D. V. Bandurin,[36] P. Banerjee,[29] S. Banerjee,[29] E. Barberis,[64] P. Bargassa,[81] P. Baringer,[59] C. Barnes,[44] J. Barreto,[2] J. F. Bartlett,[51] U. Bassler,[17] D. Bauer,[44] A. Bean,[59] M. Begalli,[3] M. Begel,[72] C. Belanger-Champagne,[5] A. Bellavance,[68] J. A. Benitez,[66] S. B. Beri,[27] G. Bernardi,[17] R. Bernhard,[42] L. Berntzon,[15] I. Bertram,[43] M. Besançon,[18] R. Beuselinck,[44] V. A. Bezzubov,[39] P. C. Bhat,[51] V. Bhatnagar,[27] M. Binder,[25] C. Biscarat,[43] K. M. Black,[63] I. Blackler,[44] G. Blazey,[53] F. Blekman,[44] S. Blessing,[50] D. Bloch,[19] K. Bloom,[68] U. Blumenschein,[23] A. Boehnlein,[51] O. Boeriu,[56] T. A. Bolton,[60] F. Borcherding,[51] G. Borissov,[43] K. Bos,[34] T. Bose,[78] A. Brandt,[79] R. Brock,[66] G. Brooijmans,[71] A. Bross,[51] D. Brown,[79] N. J. Buchanan,[50] D. Buchholz,[54] M. Buehler,[82] V. Buescher,[23] S. Burdin,[51] S. Burke,[46] T. H. Burnett,[83] E. Busato,[17] C. P. Buszello,[44] J. M. Butler,[63] S. Calvet,[15] J. Cammin,[72] S. Caron,[34] M. A. Carrasco-Lizarraga,[33] W. Carvalho,[3] B. C. K. Casey,[78] N. M. Cason,[56] H. Castilla-Valdez,[33] S. Chakrabarti,[29] D. Chakraborty,[53] K. M. Chan,[72] A. Chandra,[49] D. Chapin,[78] F. Charles,[19] E. Cheu,[46] F. Chevallier,[14] D. K. Cho,[63] S. Choi,[32] B. Choudhary,[28] L. Christofek,[59] D. Claes,[68] B. Clément,[19] C. Clément,[41] Y. Coadou,[5] M. Cooke,[81] W. E. Cooper,[51] D. Coppage,[59] M. Corcoran,[81] M.-C. Cousinou,[15] B. Cox,[45] S. Crépé-Renaudin,[14] D. Cutts,[78] M. Ćwiok,[30] H. da Motta,[2] A. Das,[63] M. Das,[61] B. Davies,[43] G. Davies,[44] G. A. Davis,[54] K. De,[79] P. de Jong,[34] S. J. de Jong,[35] E. De La Cruz-Burelo,[65] C. De Oliveira Martins,[3] J. D. Degenhardt,[65] F. Déliot,[18] M. Demarteau,[51] R. Demina,[72] P. Demine,[18] D. Denisov,[51] S. P. Denisov,[39] S. Desai,[73] H. T. Diehl,[51] M. Diesburg,[51] M. Doidge,[43] A. Dominguez,[68] H. Dong,[73] L. V. Dudko,[38] L. Duflot,[16] S. R. Dugad,[29] A. Duperrin,[15] J. Dyer,[66] A. Dyshkant,[53] M. Eads,[68] D. Edmunds,[66] T. Edwards,[45] J. Ellison,[49] J. Elmsheuser,[25] V. D. Elvira,[51] S. Eno,[62] P. Ermolov,[38] J. Estrada,[51] H. Evans,[55] A. Evdokimov,[37] V. N. Evdokimov,[39] S. N. Fatakia,[63] L. Feligioni,[63] A. V. Ferapontov,[60] T. Ferbel,[72] F. Fiedler,[25] F. Filthaut,[35] W. Fisher,[51] H. E. Fisk,[51] I. Fleck,[23] M. Ford,[45] M. Fortner,[53] H. Fox,[23] S. Fu,[51] S. Fuess,[51] T. Gadfort,[83] C. F. Galea,[35] E. Gallas,[51] E. Galyaev,[56] C. Garcia,[72] A. Garcia-Bellido,[83] J. Gardner,[59] V. Gavrilov,[37] A. Gay,[19] P. Gay,[13] D. Gelé,[19] R. Gelhaus,[49] C. E. Gerber,[52] Y. Gershtein,[50] D. Gillberg,[5] G. Ginther,[72] N. Gollub,[41] B. Gómez,[8] K. Gounder,[51] A. Goussiou,[56] P. D. Grannis,[73] H. Greenlee,[51] Z. D. Greenwood,[61] E. M. Gregores,[4] G. Grenier,[20] Ph. Gris,[13] J.-F. Grivaz,[16] S. Grünendahl,[51] M. W. Grünewald,[30] F. Guo,[73] J. Guo,[73] G. Gutierrez,[51] P. Gutierrez,[76] A. Haas,[71] N. J. Hadley,[62] P. Haefner,[25] S. Hagopian,[50] J. Haley,[69] I. Hall,[76] R. E. Hall,[48] L. Han,[7] K. Hanagaki,[51] K. Harder,[60] A. Harel,[72] R. Harrington,[64] J. M. Hauptman,[58] R. Hauser,[66] J. Hays,[54] T. Hebbeker,[21] D. Hedin,[53] J. G. Hegeman,[34] J. M. Heinmiller,[52] A. P. Heinson,[49] U. Heintz,[63] C. Hensel,[59] G. Hesketh,[64] M. D. Hildreth,[56] R. Hirosky,[82] J. D. Hobbs,[73] B. Hoeneisen,[12] M. Hohlfeld,[16] S. J. Hong,[31] R. Hooper,[78] P. Houben,[34] Y. Hu,[73] V. Hynek,[9] I. Iashvili,[70] R. Illingworth,[51] A. S. Ito,[51] S. Jabeen,[63] M. Jaffré,[16] S. Jain,[76] K. Jakobs,[23] C. Jarvis,[62] A. Jenkins,[44] R. Jesik,[44] K. Johns,[46] C. Johnson,[71] M. Johnson,[51] A. Jonckheere,[51] P. Jonsson,[44] A. Juste,[51] D. Käfer,[21] S. Kahn,[74] E. Kajfasz,[15] A. M. Kalinin,[36] J. M. Kalk,[61] J. R. Kalk,[66] S. Kappler,[21] D. Karmanov,[38] J. Kasper,[63] I. Katsanos,[71] D. Kau,[50] R. Kaur,[27] R. Kehoe,[80] S. Kermiche,[15] S. Kesisoglou,[78] A. Khanov,[77] A. Kharchilava,[70] Y. M. Kharzheev,[36] D. Khatidze,[71] H. Kim,[79] T. J. Kim,[31] M. H. Kirby,[35] B. Klima,[51] J. M. Kohli,[27] J.-P. Konrath,[23] M. Kopal,[76] V. M. Korablev,[39] J. Kotcher,[74] B. Kothari,[71] A. Koubarovsky,[38] A. V. Kozelov,[39] J. Kozminski,[66] A. Kryemadhi,[82] S. Krzywdzinski,[51] T. Kuhl,[24] A. Kumar,[70] S. Kunori,[62] A. Kupco,[11] T. Kurča,[20,*] J. Kvita,[9] S. Lager,[41] S. Lammers,[71] G. Landsberg,[78] J. Lazoflores,[50] A.-C. Le Bihan,[19] P. Lebrun,[20] W. M. Lee,[53] A. Leflat,[38] F. Lehner,[42] C. Leonidopoulos,[71] V. Lesne,[13] J. Leveque,[46] P. Lewis,[44] J. Li,[79] Q. Z. Li,[51] J. G. R. Lima,[53] D. Lincoln,[51] J. Linnemann,[66] V. V. Lipaev,[39] R. Lipton,[51] Z. Liu,[5] L. Lobo,[44] A. Lobodenko,[40] M. Lokajicek,[11] A. Lounis,[19] P. Love,[43] H. J. Lubatti,[83] M. Lynker,[56] A. L. Lyon,[51] A. K. A. Maciel,[2] R. J. Madaras,[47] P. Mättig,[26] C. Magass,[21] A. Magerkurth,[65] A.-M. Magnan,[14] N. Makovec,[16] P. K. Mal,[56] H. B. Malbouisson,[3] S. Malik,[68] V. L. Malyshev,[36] H. S. Mao,[6] Y. Maravin,[60] M. Martens,[51] S. E. K. Mattingly,[78] R. McCarthy,[73] R. McCroskey,[46] D. Meder,[24] A. Melnitchouk,[67] A. Mendes,[15] L. Mendoza,[8] M. Merkin,[38] K. W. Merritt,[51] A. Meyer,[21] J. Meyer,[22] M. Michaut,[18] H. Miettinen,[81] T. Millet,[20] J. Mitrevski,[71] J. Molina,[3] N. K. Mondal,[29] J. Monk,[45] R. W. Moore,[5] T. Moulik,[59] G. S. Muanza,[16] M. Mulders,[51] M. Mulhearn,[71] L. Mundim,[3] Y. D. Mutaf,[73] E. Nagy,[15] M. Naimuddin,[28] M. Narain,[63] N. A. Naumann,[35] H. A. Neal,[65] J. P. Negret,[8] S. Nelson,[50] P. Neustroev,[40] C. Noeding,[23] A. Nomerotski,[51] S. F. Novaes,[4] T. Nunnemann,[25] V. O'Dell,[51] D. C. O'Neil,[5] G. Obrant,[40] V. Oguri,[3] N. Oliveira,[3] N. Oshima,[51] R. Otec,[10]

G. J. Otero y Garzón,[52] M. Owen,[45] P. Padley,[81] N. Parashar,[57] S.-J. Park,[72] S. K. Park,[31] J. Parsons,[71] R. Partridge,[78] N. Parua,[73] A. Patwa,[74] G. Pawloski,[81] P. M. Perea,[49] E. Perez,[18] K. Peters,[45] P. Pétroff,[16] M. Petteni,[44] R. Piegaia,[1] M.-A. Pleier,[22] P. L. M. Podesta-Lerma,[33] V. M. Podstavkov,[51] Y. Pogorelov,[56] M.-E. Pol,[2] A. Pompoš,[76] B. G. Pope,[66] A. V. Popov,[39] W. L. Prado da Silva,[3] H. B. Prosper,[50] S. Protopopescu,[74] J. Qian,[65] A. Quadt,[22] B. Quinn,[67] K. J. Rani,[29] K. Ranjan,[28] P. A. Rapidis,[51] P. N. Ratoff,[43] P. Renkel,[80] S. Reucroft,[64] M. Rijssenbeek,[73] I. Ripp-Baudot,[19] F. Rizatdinova,[77] S. Robinson,[44] R. F. Rodrigues,[3] C. Royon,[18] P. Rubinov,[51] R. Ruchti,[56] V. I. Rud,[38] G. Sajot,[14] A. Sánchez-Hernández,[33] M. P. Sanders,[62] A. Santoro,[3] G. Savage,[51] L. Sawyer,[61] T. Scanlon,[44] D. Schaile,[25] R. D. Schamberger,[73] Y. Scheglov,[40] H. Schellman,[54] P. Schieferdecker,[25] C. Schmitt,[26] C. Schwanenberger,[45] A. Schwartzman,[69] R. Schwienhorst,[66] S. Sengupta,[50] H. Severini,[76] E. Shabalina,[52] M. Shamim,[60] V. Shary,[18] A. A. Shchukin,[39] W. D. Shephard,[56] R. K. Shivpuri,[28] D. Shpakov,[64] V. Siccardi,[19] R. A. Sidwell,[60] V. Simak,[10] V. Sirotenko,[51] P. Skubic,[76] P. Slattery,[72] R. P. Smith,[51] G. R. Snow,[68] J. Snow,[75] S. Snyder,[74] S. Söldner-Rembold,[45] X. Song,[53] L. Sonnenschein,[17] A. Sopczak,[43] M. Sosebee,[79] K. Soustruznik,[9] M. Souza,[2] B. Spurlock,[79] J. Stark,[14] J. Steele,[61] K. Stevenson,[55] V. Stolin,[37] A. Stone,[52] D. A. Stoyanova,[39] J. Strandberg,[41] M. A. Strang,[70] M. Strauss,[76] R. Ströhmer,[25] D. Strom,[54] M. Strovink,[47] L. Stutte,[51] S. Sumowidagdo,[50] A. Sznajder,[3] M. Talby,[15] P. Tamburello,[46] W. Taylor,[5] P. Telford,[45] J. Temple,[46] B. Tiller,[25] M. Titov,[23] V. V. Tokmenin,[36] M. Tomoto,[51] T. Toole,[62] I. Torchiani,[23] S. Towers,[43] T. Trefzger,[24] S. Trincaz-Duvoid,[17] D. Tsybychev,[73] B. Tuchming,[18] C. Tully,[69] A. S. Turcot,[45] P. M. Tuts,[71] R. Unalan,[66] L. Uvarov,[40] S. Uvarov,[40] S. Uzunyan,[53] B. Vachon,[5] P. J. van den Berg,[34] R. Van Kooten,[55] W. M. van Leeuwen,[34] N. Varelas,[52] E. W. Varnes,[46] A. Vartapetian,[79] I. A. Vasilyev,[39] M. Vaupel,[26] P. Verdier,[20] L. S. Vertogradov,[36] M. Verzocchi,[51] F. Villeneuve-Seguier,[44] P. Vint,[44] J.-R. Vlimant,[17] E. Von Toerne,[60] M. Voutilainen,[68,†] M. Vreeswijk,[34] H. D. Wahl,[50] L. Wang,[62] J. Warchol,[56] G. Watts,[83] M. Wayne,[56] M. Weber,[51] H. Weerts,[66] N. Wermes,[22] M. Wetstein,[62] A. White,[79] D. Wicke,[26] G. W. Wilson,[59] S. J. Wimpenny,[49] M. Wobisch,[51] J. Womersley,[51] D. R. Wood,[64] T. R. Wyatt,[45] Y. Xie,[78] N. Xuan,[56] S. Yacoob,[54] R. Yamada,[51] M. Yan,[62] T. Yasuda,[51] Y. A. Yatsunenko,[36] K. Yip,[74] H. D. Yoo,[78] S. W. Youn,[54] C. Yu,[14] J. Yu,[79] A. Yurkewicz,[73] A. Zatserklyaniy,[53] C. Zeitnitz,[26] D. Zhang,[51] T. Zhao,[83] Z. Zhao,[65] B. Zhou,[65] J. Zhu,[73] M. Zielinski,[72] D. Zieminska,[55] A. Zieminski,[55] V. Zutshi,[53] and E. G. Zverev[38]

(D0 Collaboration)

[1]*Universidad de Buenos Aires, Buenos Aires, Argentina*
[2]*LAFEX, Centro Brasileiro de Pesquisas Físicas, Rio de Janeiro, Brazil*
[3]*Universidade do Estado do Rio de Janeiro, Rio de Janeiro, Brazil*
[4]*Instituto de Física Teórica, Universidade Estadual Paulista, São Paulo, Brazil*
[5]*University of Alberta, Edmonton, Alberta, Canada, Simon Fraser University, Burnaby, British Columbia, Canada, York University, Toronto, Ontario, Canada, and McGill University, Montreal, Quebec, Canada*
[6]*Institute of High Energy Physics, Beijing, People's Republic of China*
[7]*University of Science and Technology of China, Hefei, People's Republic of China*
[8]*Universidad de los Andes, Bogotá, Colombia*
[9]*Center for Particle Physics, Charles University, Prague, Czech Republic*
[10]*Czech Technical University, Prague, Czech Republic*
[11]*Center for Particle Physics, Institute of Physics, Academy of Sciences of the Czech Republic, Prague, Czech Republic*
[12]*Universidad San Francisco de Quito, Quito, Ecuador*
[13]*Laboratoire de Physique Corpusculaire, IN2P3-CNRS, Université Blaise Pascal, Clermont-Ferrand, France*
[14]*Laboratoire de Physique Subatomique et de Cosmologie, IN2P3-CNRS, Universite de Grenoble 1, Grenoble, France*
[15]*CPPM, IN2P3-CNRS, Université de la Méditerranée, Marseille, France*
[16]*IN2P3-CNRS, Laboratoire de l'Accélérateur Linéaire, Orsay, France*
[17]*LPNHE, IN2P3-CNRS, Universités Paris VI and VII, Paris, France*
[18]*DAPNIA/Service de Physique des Particules, CEA, Saclay, France*
[19]*IReS, IN2P3-CNRS, Université Louis Pasteur, Strasbourg, France, and Université de Haute Alsace, Mulhouse, France*
[20]*Institut de Physique Nucléaire de Lyon, IN2P3-CNRS, Université Claude Bernard, Villeurbanne, France*
[21]*III. Physikalisches Institut A, RWTH Aachen, Aachen, Germany*
[22]*Physikalisches Institut, Universität Bonn, Bonn, Germany*
[23]*Physikalisches Institut, Universität Freiburg, Freiburg, Germany*
[24]*Institut für Physik, Universität Mainz, Mainz, Germany*

[25]*Ludwig-Maximilians-Universität München, München, Germany*
[26]*Fachbereich Physik, University of Wuppertal, Wuppertal, Germany*
[27]*Panjab University, Chandigarh, India*
[28]*Delhi University, Delhi, India*
[29]*Tata Institute of Fundamental Research, Mumbai, India*
[30]*University College Dublin, Dublin, Ireland*
[31]*Korea Detector Laboratory, Korea University, Seoul, Korea*
[32]*SungKyunKwan University, Suwon, Korea*
[33]*CINVESTAV, Mexico City, Mexico*
[34]*FOM-Institute NIKHEF and University of Amsterdam/NIKHEF, Amsterdam, The Netherlands*
[35]*Radboud University Nijmegen/NIKHEF, Nijmegen, The Netherlands*
[36]*Joint Institute for Nuclear Research, Dubna, Russia*
[37]*Institute for Theoretical and Experimental Physics, Moscow, Russia*
[38]*Moscow State University, Moscow, Russia*
[39]*Institute for High Energy Physics, Protvino, Russia*
[40]*Petersburg Nuclear Physics Institute, St. Petersburg, Russia*
[41]*Lund University, Lund, Sweden, Royal Institute of Technology and Stockholm University, Stockholm, Sweden, and Uppsala University, Uppsala, Sweden*
[42]*Physik Institut der Universität Zürich, Zürich, Switzerland*
[43]*Lancaster University, Lancaster, United Kingdom*
[44]*Imperial College, London, United Kingdom*
[45]*University of Manchester, Manchester, United Kingdom*
[46]*University of Arizona, Tucson, Arizona 85721, USA*
[47]*Lawrence Berkeley National Laboratory and University of California, Berkeley, California 94720, USA*
[48]*California State University, Fresno, California 93740, USA*
[49]*University of California, Riverside, California 92521, USA*
[50]*Florida State University, Tallahassee, Florida 32306, USA*
[51]*Fermi National Accelerator Laboratory, Batavia, Illinois 60510, USA*
[52]*University of Illinois at Chicago, Chicago, Illinois 60607, USA*
[53]*Northern Illinois University, DeKalb, Illinois 60115, USA*
[54]*Northwestern University, Evanston, Illinois 60208, USA*
[55]*Indiana University, Bloomington, Indiana 47405, USA*
[56]*University of Notre Dame, Notre Dame, Indiana 46556, USA*
[57]*Purdue University Calumet, Hammond, Indiana 46323, USA*
[58]*Iowa State University, Ames, Iowa 50011, USA*
[59]*University of Kansas, Lawrence, Kansas 66045, USA*
[60]*Kansas State University, Manhattan, Kansas 66506, USA*
[61]*Louisiana Tech University, Ruston, Louisiana 71272, USA*
[62]*University of Maryland, College Park, Maryland 20742, USA*
[63]*Boston University, Boston, Massachusetts 02215, USA*
[64]*Northeastern University, Boston, Massachusetts 02115, USA*
[65]*University of Michigan, Ann Arbor, Michigan 48109, USA*
[66]*Michigan State University, East Lansing, Michigan 48824, USA*
[67]*University of Mississippi, University, Mississippi 38677, USA*
[68]*University of Nebraska, Lincoln, Nebraska 68588, USA*
[69]*Princeton University, Princeton, New Jersey 08544, USA*
[70]*State University of New York, Buffalo, New York 14260, USA*
[71]*Columbia University, New York, New York 10027, USA*
[72]*University of Rochester, Rochester, New York 14627, USA*
[73]*State University of New York, Stony Brook, New York 11794, USA*
[74]*Brookhaven National Laboratory, Upton, New York 11973, USA*
[75]*Langston University, Langston, Oklahoma 73050, USA*
[76]*University of Oklahoma, Norman, Oklahoma 73019, USA*
[77]*Oklahoma State University, Stillwater, Oklahoma 74078, USA*
[78]*Brown University, Providence, Rhode Island 02912, USA*
[79]*University of Texas, Arlington, Texas 76019, USA*
[80]*Southern Methodist University, Dallas, Texas 75275, USA*
[81]*Rice University, Houston, Texas 77005, USA*
[82]*University of Virginia, Charlottesville, Virginia 22901, USA*
[83]*University of Washington, Seattle, Washington 98195, USA*
(Received 24 April 2006; published 12 December 2006)

We report a measurement of the B_s^0 lifetime in the semileptonic decay channel $B_s^0 \to D_s^- \mu^+ \nu X$ (and its charge conjugate), using approximately 0.4 fb^{-1} of data collected with the D0 detector during 2002–2004. Using 5176 reconstructed $D_s^- \mu^+$ signal events, we have measured the B_s^0 lifetime to be $\tau(B_s^0) = 1.398 \pm 0.044(\text{stat})^{+0.028}_{-0.025}(\text{syst})$ ps. This is the most precise measurement of the B_s^0 lifetime to date.

DOI: 10.1103/PhysRevLett.97.241801 PACS numbers: 13.25.Hw, 14.40.Nd

Measurements of the lifetimes of different b hadrons allow tests of the mechanism of heavy hadron decay. The spectator model predicts that all hadrons with the same heavy flavor content have identical lifetimes. However, observed charm and bottom hadron lifetimes suggest that nonspectator effects, such as interference between contributing amplitudes, are not negligible in heavy hadron decays. This implies that a mechanism beyond the simple spectator model is required. An effective theory called the heavy quark expansion (HQE) [1] includes such effects and predicts lifetime differences among the different bottom hadrons. In particular, a difference of the order of 1% is predicted between B^0 and B_s^0 mesons. The measurement of the flavor-specific B_s^0 lifetime using semileptonic decays is also useful in determining the decay width difference between the light and heavy mass eigenstates of the B_s^0 meson, which is an equal mixture of CP eigenstates that correspond to mass eigenstates in the absence of CP violation in the B_s^0 system.

In this Letter, we present a high-statistics measurement of the B_s^0 lifetime, using a large sample of semileptonic B_s^0 decays collected in $p\bar{p}$ collisions at $\sqrt{s} = 1.96$ TeV with the D0 detector at the Fermilab Tevatron Collider in 2002–2004. The data correspond to approximately 0.4 fb^{-1} of integrated luminosity. B_s^0 mesons were identified through their semileptonic decay $B_s^0 \to D_s^- \mu^+ \nu X$ [2], where the D_s^- meson decays via $D_s^- \to \phi\pi^-$, followed by $\phi \to K^+K^-$.

The D0 detector is described in detail elsewhere [3]. The detector components most important to this analysis are the central-tracking and muon systems. The D0 central-tracking system consists of a silicon microstrip tracker (SMT) and a central fiber tracker (CFT), both located within a 2 T superconducting solenoidal magnet, with designs optimized for tracking and vertexing at pseudorapidities $|\eta| < 3$ and $|\eta| < 2.5$, respectively, (where $\eta = -\ln[\tan(\theta/2)]$). A liquid-argon and uranium calorimeter has a central section covering pseudorapidities up to ≈ 1.1, and two end calorimeters that extend the coverage to $|\eta| \approx 4.2$ [4]. The muon system is located outside the calorimeters and has pseudorapidity coverage $|\eta| < 2$. It consists of a layer of tracking detectors and scintillation trigger counters in front of 1.8 T toroids, followed by two similar layers after the toroids [5].

Events with semileptonic B-meson decays were selected using inclusive single-muon triggers in a three-level trigger system. The triggers used did not impose any impact parameter criterion and were shown to not bias the lifetime measurement. Off-line, muons were identified by extrapolation of the muon track segments, formed by the hits in the muon system, to the tracks found in the central tracking system. Each muon was required to have a momentum $p > 3$ GeV/c and a transverse momentum $p_T > 2$ GeV/c.

The primary vertex of each $p\bar{p}$ interaction was defined by all available well-reconstructed tracks [6] and constrained by the mean beam-spot position. The latter was updated every few hours. The resolution of the reconstructed primary vertex was typically 20 μm in the transverse plane and 40 μm in the beam direction.

To reconstruct $D_s^- \to \phi\pi^-$ decays, tracks with $p_T > 1.0$ GeV/c were assigned the kaon mass and oppositely charged pairs were combined to form a ϕ candidate. Each ϕ candidate was required to have a mass in the range 1.008–1.032 GeV/c^2, compatible with the reconstructed ϕ mass at D0. The ϕ candidate was then combined with another track of $p_T > 0.7$ GeV/c. For the "right-sign" combinations, we required the charge of the track to be opposite to that of the muon and assigned the pion mass to this track. All selected tracks were required to have at least one SMT hit and one CFT hit. The three tracks selected were combined to form a common vertex (the D_s^- vertex) with a confidence level greater than 0.1%. The D_s^- candidate was required to have $p_T > 3.5$ GeV/c.

The secondary vertex, where the B_s^0 decays to a muon and a D_s^- meson, was obtained by finding the intersection of the trajectory of the muon track and the flight path of the D_s^- candidate. The confidence level of that vertex had to be greater that 0.01%. The reconstructed D_s^- decay vertex was required to be displaced from the primary vertex in the direction of the D_s^- momentum.

The helicity angle Φ, defined as the angle between the directions of the K^- and D_s^- in the ϕ rest frame, has a distribution proportional to $\cos^2\Phi$. A cut of $|\cos\Phi| > 0.4$ was applied to further reduce combinatorial background, which was found to have a flat distribution. In order to suppress the physics background originating from $D^{(*)}D^{(*)}$ processes [7], we required that the transverse momentum of the muon with respect to the D_s^- meson, $p_{T\text{rel}}$, exceed 2 GeV/c. The $D_s^- \mu^+$ invariant mass was also restricted to 3.4–5.0 GeV/c^2, to be consistent with a B-meson candidate. Because the number of tracks near the B_s^0 candidate tends to be small, we required the isolation $\mathcal{I} = p^{\text{tot}}(\mu^+ D_s^-)/(p^{\text{tot}}(\mu^+ D_s^-) + \sum p_i^{\text{tot}}) > 0.65$, where the sum $\sum p_i^{\text{tot}}$ was taken over all charged particles in the cone $\sqrt{(\Delta\phi)^2 + (\Delta\eta)^2} < 0.5$, with $\Delta\phi$ and $\Delta\eta$ being the azimuthal angle and the pseudorapidity with respect to the $(\mu^+ D_s^-)$ direction. The muon, kaon, and pion tracks were not included in the sum.

The lifetime of the B_s^0, τ, is related to the decay length in the transverse plane L_{xy} by $L_{xy} = c\tau p_T/m$, where p_T is

the transverse momentum of the B_s^0 and m is its invariant mass. L_{xy} is defined as the displacement of the B_s^0 vertex from the primary vertex projected onto the transverse momentum of the $D_s^- \mu^+$ system. Because the B_s^0 meson is not fully reconstructed, $p_T(B_s^0)$ is estimated by $p_T(D_s^- \mu^+)/K$, where the correction factor $K = p_T(D_s^- \mu^+)/p_T(B_s^0)$ is determined using Monte Carlo (MC) methods. The quantity used to extract the B_s^0 lifetime is called the pseudoproper decay length (PPDL). The correction factor K was applied statistically when extracting $c\tau(B_s^0)$ from the PPDL in the lifetime fit.

In the cases with more than one B_s^0 candidate per event, we chose the one with the highest vertex confidence level. We also required the PPDL uncertainty to be less than 500 μm. The resulting invariant mass distribution of the D_s^- candidates is shown in Fig. 1. The distribution for "right-sign" $D_s^- \mu^+$ candidates was fitted using a Gaussian, to describe the signal, and a second-order polynomial, to describe the combinatorial background. A second Gaussian was included for the Cabibbo-suppressed $D^- \to \phi\pi^-$ decay. The best fit result is shown in the same figure. The fit yields a signal of $5176 \pm 242(\text{stat}) \pm 314(\text{syst}) D_s^-$ candidates and a mass of 1958.8 ± 0.9 MeV$/c^2$. The width of the D_s^- Gaussian is 22.6 ± 1.0 MeV$/c^2$. The systematic uncertainty comes from the fit. For the D^- meson, the fit yields 1551 events. Figure 1 also shows the invariant mass distribution of the "wrong-sign" candidates. The observed shift in the D_s^- mass is consistent with known issues associated with the calibration of the D0 track momenta. The contribution to the mass region from reflected states was found to be negligible. Studies confirmed that this mass shift introduces no significant residual bias in the lifetime determination.

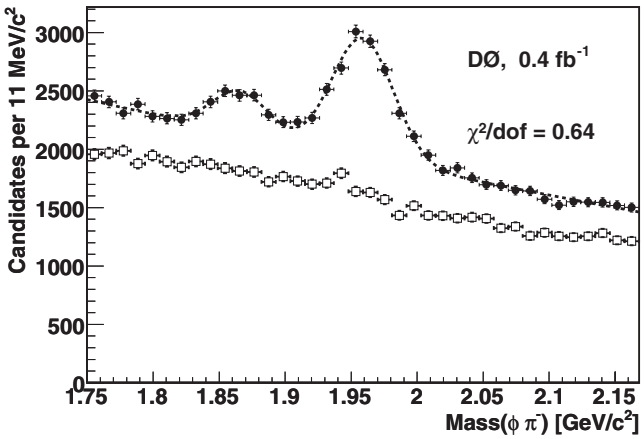

FIG. 1. The mass distribution of $\phi\pi^-$ candidates. Points with errors bars show the "right-sign" $D_s^- \mu^+$ combinations, and the open squares show the corresponding "wrong-sign" distribution. The dashed curve represents the result of the fit to the "right-sign" combinations. The two peaks are associated with the D^- and D_s^- mesons, respectively.

MC samples were generated using PYTHIA [8] for the production and hadronization phase, and EVTGEN [9] for decaying the b and c hadrons. Branching ratios from the Particle Data Group have been used when available. Detector acceptance and smearing were taken into account using the full D0 detector simulation based on GEANT [10]. Generated MC signal samples include contributions from $D_s^- \mu^+ \nu$, $D_s^{*-} \mu^+ \nu$, $D_{s0}^{*-} \mu^+ \nu$, $D_{s1}^{\prime -} \mu^+ \nu$, and $D_s^{(*)-} \tau^+ \nu$.

Apart from the background due to combinatorial processes such as a prompt muon and an identified D_s^- meson, there are several real physics processes that produce a muon and a D_s^- meson, where neither comes from the semileptonic decay of the B_s^0 meson. These "right-sign" $D_s^- \mu^+$ combinations are included in the signal sample and are defined as "physics backgrounds." Prompt D_s^- mesons from $c\bar{c}$ production at the interaction point can combine with high-p_T muons generated either via direct production or in charm decays. These $c\bar{c}$ background events are expected to have very short lifetimes and thus could introduce a significant bias in the B_s^0 lifetime measurement. Backgrounds that originate from $\bar{B}$ mesons and provide the $D_s^- \mu^+$ final state, but not via the semileptonic decay $B_s^0 \to D_s^- \mu^+ \nu X$, are called non-$B_s^0$ backgrounds. This kind of background is expected to have a relatively long lifetime, thus its effect on the B_s^0 lifetime fit is smaller than that of the charm background. There are three sources of such events: $\bar{B}^0 \to D_s^{(*)-} D^{(*)+} X$, $B^- \to D_s^{(*)-} \bar{D}^{(*)0} X$, and $\bar{B}_s^0 \to D_s^{(*)-} D^{(*)} X$, where the charm meson accompanying the $D_s^{(*)-}$, which decays to $\phi\pi^-$, decays semileptonically. The momentum of the muon coming from the decay of the $D^{(*)}$ is softer than that for the signal, because it comes from the decay of a secondary charm hadron. This implies that the contribution of these modes to the signal sample is reduced by the kinematic cuts. We found the fractional contribution of the backgrounds to the signal region to be $(10.0 \pm 7.0)\%$ for $c\bar{c}$ background and $(11.3^{+5.3}_{-3.6})\%$ for non-B_s^0 backgrounds.

The lifetime of the B_s^0 was found using a fit to the PPDL distribution. We defined a signal sample using the D_s^- mass distribution in the region from 1913.6 MeV$/c^2$ to 2004.0 MeV$/c^2$, corresponding to $\pm 2\sigma$ from the fitted mean mass. The PPDL distribution of the combinatorial background events contained in the signal sample was defined using "right-sign" events from the D_s^- sidebands (1755.3–1800.5 MeV$/c^2$, and 2117.1–2162.3 MeV$/c^2$) and "wrong-sign" events between 1755.3 and 2162.3 MeV$/c^2$. The combinatorial background due to random track combinations was modeled by the sideband sample events. This assumption is supported by the mass distribution of the "wrong-sign" combinations where no enhancement is visible in the D_s^- mass region.

The PPDL distribution obtained from the signal sample was fitted using an unbinned maximum log-likelihood method. Both the B_s^0 lifetime and the background shape were determined in a simultaneous fit to the signal and

background samples. The likelihood function $\mathcal{L}$ is given by

$$\mathcal{L} = \mathcal{C}_{\rm sig} \prod_i^{N_S} [f_{\rm sig}\mathcal{F}^i_{\rm sig} + (1 - f_{\rm sig})\mathcal{F}^i_{\rm bck}] \prod_j^{N_B} \mathcal{F}^j_{\rm bck}, \quad (1)$$

where N_S, N_B are the number of events in the signal and background samples and $f_{\rm sig}$ is the ratio of D_s^- signal events obtained from the D_s^- mass distribution fit to the total number of events in the signal sample. To constrain $f_{\rm sig}$, we factored in an additional likelihood term using the number of D_s^- signal events observed from the invariant mass distribution, and its uncertainty $\mathcal{C}_{\rm sig}$.

Because the current world-average width difference between the light and heavy mass eigenstates ($\Delta\Gamma_s$) of the B_s^0 system is small [11] compared with the current precision of the data, we used for the signal probability distribution function (PDF) $\mathcal{F}^i_{\rm sig}$, a normalized single exponential decay function convoluted with a Gaussian resolution function. The K-factor correction was also convoluted with the exponential decay function. Since *a priori*, we do not know the decay length uncertainty, which we estimated on an event-by-event basis, an overall global scale factor s was introduced as a free parameter in the B_s^0 lifetime fit. The events from non-B_s^0 background were taken into account in the fit by including similar PDFs to those in the signal but using fixed parameters according to the world-average values [12]. A different K-factor distribution was also used for each process. To take into account the $c\bar{c}$ background, we used a Gaussian distribution with fixed parameters. These contributions were evaluated and parametrized using MC methods following a similar procedure as for the signal evaluation.

The combinatorial background sample $\mathcal{F}^i_{\rm bck}$ was parametrized using a Gaussian distribution function for the resolution plus several exponential decays: two for the negative values in the PPDL distribution (one short and one long component) and two for the positive values of the distribution.

Figure 2 shows the PPDL distribution of the $D_s^-\mu^+$ signal sample with the fit result superimposed (dashed curve). The dotted curve represents the sum of the background probability function over the events in the signal sample. The B_s^0 signal is represented by the filled area.

To test the resolutions, pulls, fitting, and selection criteria, we performed detailed studies using MC samples and found no significant bias in our analysis procedure. In order to study the stability of the B_s^0 lifetime measurement, we split the data sample into two parts according to different kinematic and geometric parameters, compared the fitted results, and found the lifetimes consistent within their uncertainties. We also varied the selection criteria and mass fit ranges, and did not observe any significant shifts. We performed an extensive study of our fitting procedure, looking for any possible bias using MC ensembles with statistics of the size of our data set and distributions as

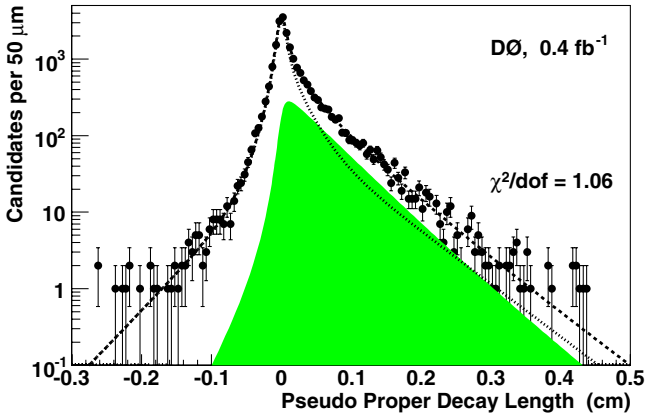

FIG. 2 (color online). Pseudoproper decay length distribution for $D_s^-\mu^+$ candidates with the result of the fit superimposed as the dashed curve. The dotted curve represents the combinatorial background and the filled area represents the B_s^0 signal.

those in data. These samples were fitted, and the mean and width of the distributions of extracted parameters were found to be consistent with the fits to data. One final check of the procedure involved performing a similar lifetime fit to a control sample defined by the Cabibbo-suppressed decay $D^- \to \phi\pi^-$ (see Fig. 1). We found that 89.1% of the sample comes from $B^0 \to D^-\mu^+X$, and the B^0 lifetime to be 1.541 ± 0.093 ps, where the uncertainty is statistical only. This result is in good agreement with the world-average B^0 lifetime [11,12].

We considered and evaluated various sources of systematic uncertainties. The major contributions come from the determination of the combinatorial background, the model for the resolution, and the physics background. To determine the systematics due to the uncertainty on the combinatorial background, we tested other assumptions on the background samples: we used just the events in the sidebands, just the events in the wrong-sign combinations, and removed either the right sideband or the left sideband samples. We also modified the definitions of those samples, changing the mass window sizes and positions. The largest difference in $c\tau$ observed in these variations of background modeling was 4.3 μm, which was taken to be the systematic uncertainty due to this source. The effect of uncertainty in the resolution of the decay length was studied using an alternative global scale factor s. We repeated the lifetime fit with fixed values of s obtained from MC samples and from a different lifetime analysis [13]. Using a variation of the resolution scale by a factor of 2 beyond these bounds, we found a 3.7 μm variation in $c\tau$. The uncertainty from the physics background was evaluated by varying the branching fractions of the different processes as well as the shapes of the lifetime templates, as given by their known lifetime values [12]. The variations were within 1 standard deviation in each case. Assuming no correlation between them, we added the effects of all the variations in quadrature and found a total contribution of

$^{+2.9}_{-4.2}$ μm. Using a similar procedure, we evaluated the uncertainty coming from the determination of the $c\bar{c}$ background and found a difference of $^{+2.3}_{-0.8}$ μm.

To evaluate the uncertainty associated with the K factor determination, we modified the kinematics of the event using a different decay model, a different p_T spectrum for the b quark, and a different p_T spectrum for the muon. We also varied the amount of each component, according to their uncertainty, of the $B_s^0 \to D_s^- \mu^+ X$ signal. In each case, the K factor was reevaluated and the fit repeated. We added all K factor variation effects in quadrature and found a total uncertainty of $^{+3.6}_{-2.1}$ μm.

There are two requirements in our selection method that could potentially change the final result by altering the shape of the PPDL distribution: $p_{T\mathrm{rel}} > 2$ GeV/c and the positive displacement from the primary vertex of the reconstructed D_s^- decay vertex. Using MC methods, we evaluated their effects by removing them one at a time. The largest variation observed was $^{+3.0}_{-0.3}$ μm, and the selection efficiency is flat as a function of proper decay time. The effect of a possible misalignment of the SMT system was tested in Ref. [13]. We repeated the study using MC signal samples and observed the same shift of $c\tau = 2$ μm, which was taken as a systematic uncertainty due to possible misalignment. The total systematic uncertainty from all of these sources added in quadrature is $^{+8.4}_{-7.6}$ μm.

In summary, using an integrated luminosity of approximately 0.4 fb^{-1}, we have measured the B_s^0 lifetime in the decay channel $D_s^- \mu^+ \nu X$ to be $\tau(B_s^0) = 1.398 \pm 0.044(\mathrm{stat})^{+0.028}_{-0.025}(\mathrm{syst})$ ps. Note that this measurement takes $\Delta\Gamma_s$ equal to zero. The extraction of the average lifetime $\bar{\tau}_s$ for $\Delta\Gamma_s \neq 0$ is straightforward [11]. The result is in good agreement with previous experiments as well as the current world-average value for all flavor-specific decays, $\tau(B_s^0) = 1.442 \pm 0.066$ ps [11,14]. Our B_s^0 lifetime measurement is the most precise to date and exceeds the precision of the current world-average measurement $\tau(B_s^0)_{\mathrm{PDG}} = 1.461 \pm 0.057$ ps [12], where semileptonic and hadronic decays were combined. This measurement is approximately 2.5σ away from the B^0 lifetime, more than the 1% predicted by HQE.

We thank the staffs at Fermilab and collaborating institutions, and acknowledge support from the DOE and NSF (USA); CEA and CNRS/IN2P3 (France); FASI, Rosatom and RFBR (Russia); CAPES, CNPq, FAPERJ, FAPESP and FUNDUNESP (Brazil); DAE and DST (India); Colciencias (Colombia); CONACyT (Mexico); KRF and KOSEF (Korea); CONICET and UBACyT (Argentina); FOM (The Netherlands); PPARC (United Kingdom); MSMT (Czech Republic); CRC Program, CFI, NSERC and WestGrid Project (Canada); BMBF and DFG (Germany); SFI (Ireland); The Swedish Research Council (Sweden); Research Corporation; Alexander von Humboldt Foundation; and the Marie Curie Program.

*On leave from IEP SAS Kosice, Slovakia.
†Visiting scientist from Helsinki Institute of Physics, Helsinki, Finland.

[1] I. I. Bigi *et al.*, in *B Decays*, edited by S. Stone (World Scientific, Singapore, 1994), 2nd ed..
[2] Unless otherwise stated, charge-conjugate states are implied.
[3] V. M. Abazov *et al.*, Nucl. Instrum. Methods Phys. Res., Sect. A **565**, 463 (2006).
[4] S. Abachi *et al.*, Nucl. Instrum. Methods Phys. Res., Sect. A **338**, 185 (1994).
[5] V. M. Abazov *et al.*, Nucl. Instrum. Methods Phys. Res., Sect. A **552**, 372 (2005).
[6] J. Abdallah *et al.*, Eur. Phys. J. C **32**, 185 (2004).
[7] $D^{(*)}$ denotes either D, D^*, or D^{**}.
[8] T. Sjöstrand *et al.*, Comput. Phys. Commun. **135**, 238 (2001).
[9] D. J. Lange, Nucl. Instrum. Methods Phys. Res., Sect. A **462**, 152 (2001).
[10] R. Brun *et al.*, CERN Report No. DD/EE/84-1, 1984.
[11] K. Anikeev *et al.* (Heavy Flavor Averaging Group), hep-ex/0505100.
[12] S. Eidelman *et al.* (Particle Data Group), Phys. Lett. B **592**, 1 (2004).
[13] V. M. Abazov *et al.*, Phys. Rev. Lett. **94**, 042001 (2005).
[14] D. Buskulic *et al.*, Phys. Lett. B **377**, 205 (1996); K. Ackerstaff *et al.*, Phys. Lett. B **426**, 161 (1998); F. Abe *et al.*, Phys. Rev. D **59**, 032004 (1999); P. Abreu *et al.*, Eur. Phys. J. C **16**, 555 (2000).